

Spectroscopic Imaging Using Quadrature

Optical Coherence Tomography

by

Pimrapat Thanusutiyabhorn

A Thesis submitted to the Faculty of Graduate Studies of

The University of Manitoba

in partial fulfilment of the requirements of the degree of

MASTER OF SCIENCE

Department of Electrical and Computer Engineering

University of Manitoba

Winnipeg

Copyright ©2014 by Pimrapat Thanusutiyabhorn

## **Abstract**

Optical Coherence Tomography (OCT) is a subsurface imaging technique with many biomedical and industrial applications. In this thesis, we describe our design and implementation of a time domain OCT system. We used this system to obtain OCT images of objects that are important in different applications. We also used an existing quadrature OCT system to obtain both real and imaginary parts of an OCT image. We introduced a new interpretation of OCT images as the 2<sup>nd</sup> derivative of the scattering potential of an object. To obtain this scattering potential from its 2<sup>nd</sup> derivative, we implemented a method of definite integration in the spectral-domain. The obtained scattering potential was used to separate the scattering profile from the absorption profile of an object. We applied this new spectroscopic imaging method to quadrature OCT images of different objects.

## Acknowledgements

First and foremost, I wish to express sincere appreciation to my advisor, Dr. Sherif Sherif, for giving me an opportunity to join the program and his amazing team. I have learned invaluable knowledge and experience in the past few years. He has been very supportive, both academically and emotionally. He always believes in my potential which means a lot to me. The work in this thesis would not be successful without his guidance and contributions.

Besides my advisor, I also would like to thank my thesis committee, Dr. Arkady Major and Dr. Jitendra Paliwal, for their comments and valuable questions. I had taken many courses with Dr. Major and learned a lot from him. He also gave a helpful suggestion on optical alignment when I was building the OCT system. I also would like to thank the people at the Institute for Microstructural Sciences for providing quadrature OCT data for analysis.

Next, I would like to thank my lab fellows and classmates for academically and mentally support. I would like to specially thank Fernando Saccon for his implementation of the Data Acquisition module. My work would not be succeeded without his collaboration.

I also would like to send my gratitude to my former advisors in Thailand for inspiring me to pursue graduate studies and their supports. Lastly, I would like to thank my family and friends, here and back in Thailand, for *everything* they assisted and gave me. This journey would not be a great one without them.

# Table of Contents

Abstract.....	i
Acknowledgements.....	ii
Table of Contents.....	iii
List of Tables .....	vi
List of Figures.....	vii
Chapter 1 Introduction .....	1
1.1. Motivation.....	1
1.2. The objectives of the thesis.....	1
1.3. Thesis contributions.....	2
1.4. Thesis structure.....	2
Chapter 2 Optical Coherence Tomography .....	4
2.1. Optical imaging and OCT.....	4
2.2. Optical interferometry and OCT.....	5
2.3. Time-Domain OCT (TD-OCT).....	6
2.4. Spectral-Domain OCT (SD-OCT).....	9
2.5. Swept-Source OCT (SS-OCT).....	10
2.5.1. Analysis of scalar scattering of light from tissue.....	10
2.5.2. Swept-source OCT.....	13
2.6. Resolution and scanning depth of OCT.....	14
2.6.1. Axial resolution.....	14
2.6.2. Transverse resolution.....	16
2.6.3. Imaging depth of OCT.....	18
Chapter 3 Design and implementation of the time-domain OCT system.....	19
3.1. Introduction.....	19
3.2. Optical design of time-domain OCT systems.....	19
3.3. Implementation of our time-domain OCT system.....	20
3.3.1. Optical module.....	20
3.3.2. Data Acquisition module.....	33

Chapter 4	Graphical User Interface (GUI) of our time-domain OCT system and imaging examples .....	39
4.1.	Introduction.....	39
4.2.	Graphical User Interface .....	39
4.2.1.	Setup Mode GUI.....	39
4.2.2.	Run Mode GUI .....	43
4.3.	Example images acquired using our OCT system .....	44
Chapter 5	Extraction of complex scattering potential using Quadrature OCT .....	53
5.1.	Introduction.....	53
5.2.	Overview of spectroscopic OCT (S-OCT) .....	53
5.3.	Previous work of using OCT for local separation of scattering and absorption effects in a sample .....	54
5.4.	Our work to obtain the complex scattering profile of a sample using quadrature OCT ...	56
5.4.1.	Relationship between the scattering potential and the complex refractive index of a sample .....	56
5.4.2.	Obtaining the complex scattering potential using a swept-source quadrature OCT ..	58
5.4.3.	New interpretation of SS-OCT images .....	60
5.5.	Experimental setup and results .....	61
5.5.1.	Swept Source quadrature OCT .....	61
5.5.2.	Examples of images acquired by our quadrature OCT system .....	63
Chapter 6	Obtaining scattering and absorption profiles from the complex scattering potential .....	71
6.1.	Method to obtain scattering and absorption profiles from the complex scattering potential .....	71
6.1.1.	Integrating the 2nd derivative of the scattering potential.....	71
6.1.2.	Retrieval of the DC value of the complex scattering potential .....	72
6.1.3.	Approximate value of the scattering potential scale .....	73
6.1.4.	Obtaining scattering and absorption profiles from the complex scattering potential. ....	74
6.2.	Results of the OCT data.....	74
Chapter 7	Implementation of differentiation and integration in the spectral domain .....	79

7.1.	Theoretical background .....	79
7.1.1.	Discrete Fourier Transform (DFT) .....	79
7.1.2.	Differentiation in the spectral domain .....	81
7.1.3.	Integration in the spectral domain.....	82
7.2.	Implementation of differentiation in the spectral domain.....	84
7.2.1.	Buffered spectral differentiation .....	84
7.2.2.	Application to test functions .....	88
7.3.	Implementation of integration in the spectral domain .....	95
7.3.1.	Buffered spectral integration.....	95
7.3.2.	Experimental results of test functions .....	98
Chapter 8	Summary and future development .....	105
APPENDIX A.	Time-Frequency Analysis .....	107
APPENDIX B.	Lagrange interpolation.....	115
Bibliography	.....	116

## List of Tables

Table 3-1 Lists of optical components.....	22
Table 3-2 Specification of the telecentric lens used in our OCT system.....	27
Table 3-3 NI SCB-68 connections.....	36

## List of Figures

Figure 2-1 Optical interferometry and OCT .....	6
Figure 2-2 A schematic of a TD-OCT using Michelson interferometer .....	6
Figure 2-3 A Michelson interferometer based SD-OCT and a spectrometer.....	9
Figure 2-4 A diagram of an object being illuminated by a light wave [7].....	11
Figure 2-5 Michelson interferometer based SD-OCT using swept source and a photodetector....	14
Figure 3-1 A schematic of the TD-OCT with balanced detection .....	21
Figure 3-2 Optical delay line .....	25
Figure 3-3 Signal of coarse sync and digital/analog sync of the delay line.....	26
Figure 3-4 A schematic of the telecentric lens used in our OCT system.....	27
Figure 3-5 Optical circulator.....	28
Figure 3-6 Schematics of (a) 2x2 fused fiber coupler (b) 3x3 fused fiber coupler .....	29
Figure 3-7 Plot of retardance (wave) of each paddle ( $d = 125 \mu m$ , $D = 18mm$ ) .....	30
Figure 3-8 The sample imaging probe (a) schematic diagram (b) actual setup .....	32
Figure 3-9 Interferometric signal captured from an oscilloscope .....	33
Figure 3-10 A diagram of the computer unit .....	34
Figure 3-11 (a) PXI-8120 with PXI-7965R and PXI-7861R (installed inside PXI-8120) and (b) connections inside the DAQ NI scb-68.....	35
Figure 3-12 VI flowchart .....	37
Figure 4-1 “Welcome page” GUI of our OCT system.....	39
Figure 4-2 Setup Mode GUI – “Acquisition” .....	40
Figure 4-3 Setup Mode GUI – “Processing” .....	41
Figure 4-4 Setup Mode GUI – “Delay Line” .....	42
Figure 4-5 GUI of the Setup mode – “Galvo Mirrors” .....	42
Figure 4-6 Run Mode GUI.....	43

Figure 4-7 OCT image of an onion skin .....	44
Figure 4-8 OCT image of a celery stalk.....	45
Figure 4-9 OCT image of a chicken breast (a) actual sample - scan line is indicated in orange (b) OCT image.....	45
Figure 4-10 OCT images of a fingertip (a) without gloves (b) with gloves.....	46
Figure 4-11 Axolotl embryo with gel (a) actual sample (b) OCT image.....	46
Figure 4-12 Axolotl embryo without gel (a) actual sample (b) OCT image.....	47
Figure 4-13 Kraft paper (a) actual sample (b) OCT image.....	47
Figure 4-14 A gap between two microfibers (a) actual sample (b) B-scan OCT image along scan line shown in (a), (c) 3D image .....	48
Figure 4-15 A small gap between two fiber strips (a) actual sample (b) OCT image (c) 3D image .....	49
Figure 4-16 Two small gaps between two fiber strips (a) actual sample (b) OCT image (c) 3D image.....	50
Figure 4-17 Overlap microfiber strips (a) actual sample (b) OCT image (c) 3D image.....	51
Figure 4-18 Overlap microfiber strips (a) actual sample (b) OCT image from scan line1 (c) OCT image from scan line1 (d) 3D image.....	52
Figure 5-1 A diagram of A Mach-Zehnder interferometer using $3 \times 3$ fiber coupler to acquire a complex interferometric signal [10].....	59
Figure 5-2 An A-scan signal (a) interferometric signals from the measurements (b) A-scan .....	62
Figure 5-3 OCT images of a fingertip (a) full range image (b) ROI indicated by the white dashed box in (a).....	63
Figure 5-4 Images representing the 2 <sup>nd</sup> derivative of the scattering potential profile of a fingertip (a) real part and (b) imaginary part.....	64
Figure 5-5 OCT images of a fingertip with gloves. (a) full range image and (b) ROI indicated by the white dashed box in (a).....	65

Figure 5-6 Images representing the 2<sup>nd</sup> derivative of the scattering potential profile of a fingertip with gloves(a) real part and (b) imaginary part..... 66

Figure 5-7 OCT images of an axolotl embryo. (a) full range image and (b) ROI indicated by the white dashed box in (a) ..... 67

Figure 5-8 Images representing the 2<sup>nd</sup> derivative of the scattering potential profile of an axolotl embryo (a) real part and (b) imaginary part..... 68

Figure 5-9 OCT images of clear adhesive tape. (a) full range image and (b) ROI indicated by the white dashed box in (a) ..... 69

Figure 5-10 Images representing the 2<sup>nd</sup> derivative of the scattering potential profile of clear adhesive tape(a) real part and (b)imaginary part ..... 70

Figure 6-1 Scattering profile of a fingertip (a) scattering profile (b) 2<sup>nd</sup> derivative of the scattering profile ..... 75

Figure 6-2 Absorption profile of a fingertip (a) absorption profile (b) 2<sup>nd</sup> derivative of the absorption profile ..... 75

Figure 6-3 Scattering profile of a fingertip with gloves (a) scattering profile (b) 2<sup>nd</sup> derivative of the scattering profile ..... 76

Figure 6-4 Absorption profile of a fingertip with gloves (a) absorption profile (b) 2<sup>nd</sup> derivative of the absorption profile ..... 76

Figure 6-5 Scattering profile of an axolotl embryo (a) scattering profile (b) 2<sup>nd</sup> derivative of the scattering profile ..... 77

Figure 6-6 Absorption profile of an axolotl embryo (a) absorption profile (b) 2<sup>nd</sup> derivative of the absorption profile ..... 77

Figure 6-7 Scattering profile of clear adhesive tape (a) scattering profile (b) 2<sup>nd</sup> derivative of the scattering profile ..... 78

Figure 6-8 Absorption profile of clear adhesive tape (a) absorption profile (b) 2<sup>nd</sup> derivative of the absorption profile ..... 78

Figure 7-1 An arbitrary polynomial function.....	85
Figure 7-2 Analytical derivatives (a) 1 <sup>st</sup> derivative and (b) 2 <sup>nd</sup> derivative.....	85
Figure 7-3 Derivatives using spectral derivative technique (a) 1 <sup>st</sup> derivative and (b) 2 <sup>nd</sup> derivative .....	86
Figure 7-4 A periodic function where the original function and its duplicates are shown in solid line and the buffered zones are represented by circle markers .....	87
Figure 7-5 Plots of the 1 <sup>st</sup> and 2 <sup>nd</sup> derivatives using buffered spectral Fourier derivative technique .....	88
Figure 7-6 Plot of $f(n) = n^2$ .....	89
Figure 7-7 Plots of $f''(n) = 2$ (a) analytical (b) derivative using standard FFT, and (c) derivative using buffered spectral derivative .....	90
Figure 7-8 Plot of $f(n) = -n^3 + 0.2n^2 + 0.7n + 1$ .....	91
Figure 7-9 Plots of $f'(n) = -3n^2 + 0.4n + 0.7$ (a) analytical (b) derivative using standard FFT, and (c) derivative using buffered spectral derivative .....	91
Figure 7-10 Plots of $f''(n) = -6n + 0.4$ (a) analytical (b) derivative using standard FFT, and (c) derivative using buffered spectral derivative .....	92
Figure 7-11 Plot of $f(n) = -14n^5 - 78n^4 + 32n^3 + 2n^2 - 2n + 2$ .....	93
Figure 7-12 Plots of $f'(n) = -54n^4 - 72n^3 + 92n^2 + 4n - 2$ (a) analytical (b) derivative using standard FFT, and (c) derivative using buffered spectral derivative.....	93
Figure 7-13 Plots of $f''(n) = -5n^3 - 212n^2 + 9n + 4$ (a) analytical (b) derivative using standard FFT, and (c) derivative using buffered spectral .....	94
Figure 7-14 Integration in The spectral domain (a) given a smooth non-periodic $f'(n)$ (b) comparison plots between $f(n)$ (dashed line) and the incorrect result $fn$ , and (c) incorrect $fn$ after DC offset compensation .....	95
Figure 7-15 Plots of $fp, a'$ where (a) $a = a_1$ , (b) $a = a_2$ , and (c) $a = a_3$ and $a_3 > a_2 > a_1$ ..	96

Figure 7-16 Comparison plots of the results from the integration method and the original $f(n)$ .	97
Figure 7-17 $f_n$ converges to $f(n)$ during the iterative process .....	98
Figure 7-18 Plot of the second derivative $f''n = 2$ .....	99
Figure 7-19 $f'n = 2 \times n$ (a) analytical (b) cumulative sum method, and (c) integration in the spectral domain .....	99
Figure 7-20 $fn = n^2$ (a) analytical (b) cumulative sum method, and (c) integration in the spectral domain .....	100
Figure 7-21 The plot of $f''n = -6n + 0.4$ .....	101
Figure 7-22 $f'n = -3n^2 + 0.4n + 0.7$ (a) analytical (b) cumulative sum method, and (c) integration in the spectral domain.....	101
Figure 7-23 $fn = -n^3 + 0.2n^2 + 0.7n + 1$ (a) analytical, (b) cumulative sum method, and (c) integration in the spectral domain.....	102
Figure 7-24 Plot of $f''(n) = -5n^3 - 212n^2 + 9n + 4$ .....	103
Figure 7-25 $f'(n) = -54n^4 - 72n^3 + 92n^2 + 4n - 2$ (a) analytical (b) cumulative sum method, and (c) integration in the spectral domain.....	103
Figure 7-26 $f(n) = -14n^5 - 78n^4 + 32n^3 + 2n^2 - 2n + 2$ (a) analytical (b) cumulative sum method, and (c) integration in the spectral domain.....	104

# Chapter 1

## Introduction

### 1.1. Motivation

Optical Coherence Tomography (OCT) is a subsurface imaging technique that typically uses interferometry of a low coherence wave [1]. The structure of a sample or specimen, such as biological tissue, is determined from the backscattered wave [2].

The functionality of OCT was enlarged by the development of the spectroscopic OCT [3, 4, 5]. The spectroscopic properties, such as the absorption part of the refractive index of the sample, can be determined by digitally processing the data measured from the conventional OCT. Finding refractive index profiles of a sample is an interesting application of the OCT. The simplest way of determining the refractive index is to compare the physical length and the optical path length of the sample [6]. However, refractive index of a sample is essentially a complex number; the real part of the value corresponds to the scattering properties of the sample, whereas, the imaginary part corresponds to its absorption. In general, only the real part profile is likely concerned than the imaginary part. The solution to extracting both real and imaginary parts of the refractive index using the OCT has not been fully addressed.

### 1.2. The objectives of the thesis

The scattering potential of an object is related to the squared value of the complex refractive index [2, 7]. Typical OCT allows one to measure the real part of the backscattered signal which refers to the real part of the scattering potential [8, 9]. With quadrature OCT, we are able to measure both real and imaginary signal [10, 11]. Hence, through such a system, it is possible to attain the profile of the real and imaginary parts of the scattering potential. With the information, it is conceivable to be able to approximate the scattering and absorption effect of the sample.

The aim of this thesis is 1) to build a time domain OCT system and 2) to develop a method of extracting the complex scattering potential and the complex refractive index profiles of the sample based on the swept source quadrature OCT.

### **1.3. Thesis contributions**

1. Design and implementation of a time-domain OCT system.
2. Development of a method to obtain the scattering potential profile of the sample using the swept source quadrature OCT. This information can be used to separate the effects of scattering and absorption properties of the sample.
3. Implementation of numerical methods for differentiation and integration in the spectral domain.

### **1.4. Thesis structure**

In Chapter 2, we focus on the background of OCT. We explain the basic principles of OCT, including time-domain OCT and spectral-domain OCT. The principle of swept-source OCT is described elaborately using Fercher's analysis [7]. This section will be revisited again in Chapter 5. Finally, we discuss the limitations of OCT, e.g. axial resolution, transverse resolution, and imaging depth.

Chapter 3 describes optical design and implementation of a time-domain OCT system. The implementation of this time-domain OCT system is divided into two modules. In the optical module, we include an overview of the setup, a list of components and their specifications. In the data acquisition module, the architecture of the acquisition unit and the data flow of the Virtual Instrument state machines are described.

Chapter 4 describes the Graphic User Interface (GUI) of our time-domain OCT system. Some imaging examples performed by this system are illustrated at the end of this chapter.

Chapter 5 provides an overview of the spectroscopic OCT and previous work on using OCT to find refractive index profiles of a sample. Then, we describe our analysis and method in extracting the real and imaginary profiles of the scattering potential from quadrature OCT data. We present the results of OCT images produced by a quadrature OCT system that was developed at the Institute for Microstructural Sciences, National Research Council Canada.

Chapter 6 is a continuation from Chapter 5 where we propose a procedure to obtain the complex scattering potential function from its derivative and to separate the scattering and absorption effects. The results from the procedure are shown at the end of the chapter.

Chapter 7 discusses implementations of techniques for numerical differentiation and numerical integration in the spectral domain which were needed for our results in Chapter 6. We present theoretical background of the differentiation and integration in the spectral domain.

Chapter 8 presents conclusions of research and suggestions for future work.

## **Chapter 2**

### **Optical Coherence Tomography**

#### **2.1. Optical imaging and OCT**

Optical imaging is a technique to reproduce the physical structure of an object by radiating the object with an electromagnetic wave, and measuring the back-reflected wave by some sensor [12]. The shape of the object and its physical properties, such as absorption, scattering, fluorescence, etc., are obtained from the measured field. Each of the well-known imaging techniques, such as X-ray tomography, magnetic resonance imaging (MRI), ultrasound, and optical coherence tomography (OCT), can obtain different physical information about the object. This is because each imaging technique uses different waves, and the interactions between these waves and the sample are different [1]. Existing imaging techniques such as microscopy/confocal microscopy, ultrasound, MRI, or CT provide images with different imaging resolution and penetration depth in a biological sample. The characteristics of the imaging module are affected by the frequency of the waves used to illuminate the sample. In general, waves with high frequencies yield higher resolution; however, they tend to have a lower penetration depth due to higher attenuation effect in biological tissue [13]. OCT has features that fill the gap between the confocal microscopy and ultrasound which is advantageous for many biomedical imaging applications.

OCT is a noninvasive subsurface imaging technique that utilizes optical interferometry [1, 14]. A cross-sectional image of a sample is generated from multiple interferometry measurements in axial and transverse directions known as A-scans and B-scans. As a result, OCT creates a two-dimensional interferometric signal that represents the subsurface structure. A volumetric image can also be generated by performing raster scanning of the sample to acquire multiple cross-sectional images.

OCT has become an established technology for medical diagnostics and optical biopsy [15], as it has several advantages over conventional biopsy: 1) being non-invasive avoids the complication that might occur during a conventional biopsy procedure; 2) it also allows the diagnostic at some locations, where the conventional biopsy cannot be performed, e.g. the eye. The first OCT images were performed with 830 nm wavelength light on *in vitro* retina and *ex vivo* human coronary artery by Huang *et al.* in 1991 [14]. OCT applications in highly scattering tissue have been expanded by using 1300 nm wavelength, as this wavelength allows deeper imaging depth (~2-3mm). OCT is also applied to other area of medicine, such as dermatology [16], laryngology [17], and dentistry [18]. The applications of OCT are not limited to biomedical imaging, but also extend to industrial applications. For example, OCT has been used in studying polymer matrix composites (PMCs) [19], inspecting and analysis of jade [20], and in forensics [21, 22].

## **2.2. Optical interferometry and OCT**

Optical interferometry is an accurate sensing technique where the properties of a superimposed wave resulting from scatterers in a medium (or sample) and the original wave are analyzed [23]. Interference is a phenomenon where two or more light waves are superimposed, and the intensity in the region of superposition appears as fringes varying in the maxima and minima pattern [24]. Small differences between the two waves, such as amplitude and phase, result in changes in the intensity, visibility, and interference pattern of the superimposed wave. Low coherence interferometry (LCI) is a technique that uses a low coherence light source in an interferometer. One important concept in LCI is temporal coherence of light. The temporal coherence of light is the correlation between the fields at the same point but different times, which is related to the spectral bandwidth of this light [24].

OCT can be categorized into two types of systems: time-domain OCT and spectral-domain OCT. The mathematical principles of these OCT rely on the concept of coherence interferometry as shown in the diagram in Figure 2-1.

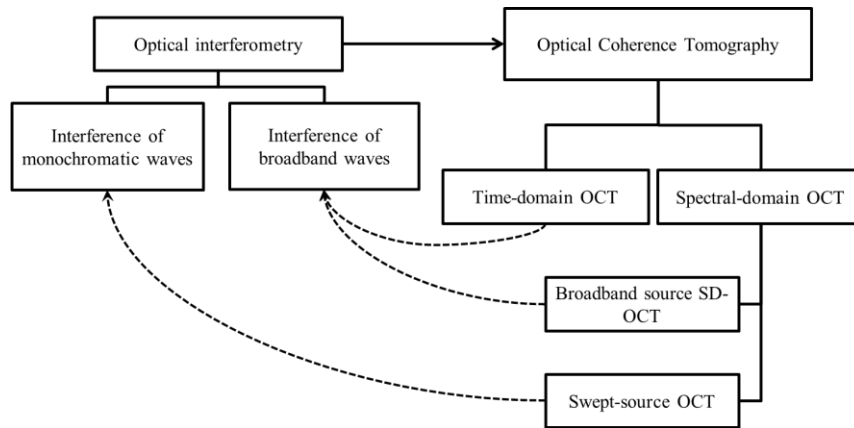


**Figure 2-1 Optical interferometry and OCT**

### 2.3. Time-Domain OCT (TD-OCT)

Time-domain OCT is a localized imaging technique based on LCI where the interference signal is formed by mixing a wave that is scattered from an object with a reference wave. Varying the time delay in the reference wave path provides a scanning axial (A-scan) direction and the substructure of a sample is scanned point-by-point. The system could be accompanied with a movable sample stage or galvo-mirrors for raster scanning in the transverse direction (B-scan) to obtain a cross sectional or volumetric image of microstructure of the sample.

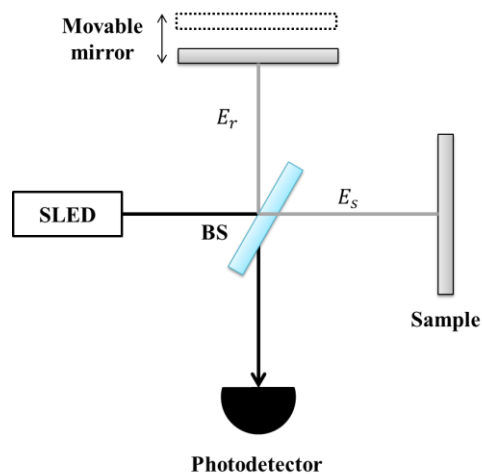


**Figure 2-2 A schematic of a TD-OCT using Michelson interferometer**

The principle of TD-OCT was described in detail by Hee [25]. Shown in Figure 2-2 is a diagram of a standard Michelson interferometer based OCT. Light from a broadband source or a superluminescent diode (SLED) is divided by a 50/50 beam splitter into two wavefields  $E_r$  and  $E_s$ . The wavefield  $E_r$  travels to a movable mirror, whereas the wavefield  $E_s$  travel to the sample. In the reference arm, the wavefield  $E_r$  is reflected by the mirror. Then, the wave travels back to the beam splitter, and interfere with the backscattered wave  $E_s$  from the sample arms. The reference and sample wavefields can be described as shown in Eq. (2.1) and Eq. (2.2):

$$E_r(\omega) = A_r(\omega) \exp[-jk_r(\omega)l_r], \quad (2.1)$$

$$E_s(\omega) = A_s(\omega) \exp[-jk_s(\omega)l_s], \quad (2.2)$$

where  $A_r(\omega)$  and  $A_s(\omega)$  is the reflection amplitude,  $k_r(\omega)$  and  $k_s(\omega)$  are propagation constants, and  $l_r$  and  $l_s$  are optical distances from the SLED to the detector of the reference wave and the sample wave, respectively. The power of the interference signal is detected by the detector which can be described as a sum of monochromatic plane wave component as described in Eq. (2.3).

$$i_d(\omega, \Delta l) \propto \text{real} \left\{ \int_{-\infty}^{\infty} S(\omega) \exp[-j\Delta\phi(\omega)] \frac{d\omega}{2\pi} \right\}, \quad (2.3)$$

where  $S(\omega) = A_s(\omega)A_r(\omega)^*$  is the power spectral density and  $\Delta\phi(\omega)$  is the phase mismatch between the two arms given by,

$$\Delta\phi(\omega) = k_s(\omega)l_s - k_r(\omega)l_r. \quad (2.4)$$

When the waves travel in nondispersive media, the propagation constants  $k_r(\omega)$  and  $k_s(\omega)$  are assumed to be the same. The SLED can be described mathematically as a band limited light

source  $S(\omega - \omega_0)$  that has a center frequency at  $\omega_0$ . Accordingly, the propagation constants  $k_r(\omega)$  and  $k_s(\omega)$  can be expanded by the 1<sup>st</sup>-order Taylor expansions  $k_r(\omega) = k_s(\omega) = k(\omega_0) + k'(\omega_0)(\omega - \omega_0)$ . The phase mismatch  $\Delta\phi(\omega)$  in Eq. (2.4) can be rewritten as

$$\Delta\phi(\omega) = k(\omega_0)(\Delta l) + k'(\omega_0)(\omega - \omega_0)(\Delta l), \quad (2.5)$$

where  $\Delta l = l_S - l_R$ . By substituting Eq. (2.5) into Eq. (2.3), the interferometric signal is obtained.

$$I_d(\Delta l) \propto \text{real} \left\{ \exp[-j\omega_0\Delta\tau_p] \int_{-\infty}^{\infty} S(\omega - \omega_0) \exp[-j(\omega - \omega_0)\Delta\tau_g] \frac{d(\omega - \omega_0)}{2\pi} \right\} \quad (2.6)$$

The definitions of the phase delay and group delay mismatches in Eq. (2.6) can be described by Eq. (2.7) and Eq. (2.8) as

$$\Delta\tau_p = \frac{k(\omega_0)}{\omega_0} \Delta l = \frac{\Delta l}{v_p}, \quad (2.7)$$

$$\Delta\tau_g = k'(\omega_0) \Delta l = \frac{\Delta l}{v_g}. \quad (2.8)$$

From Eq. (2.6), the integral term is the Fourier transform of the power spectral density. This term corresponds to the autocorrelation function,  $\gamma(z)$ , based on the Wiener-Khinchin theorem [25]. This function defines the axial resolution of the imaging system which will be explained in section 2.6. The photocurrent signal in Eq. (2.6) can be rewritten as follows:

$$I_d(\Delta l) \propto \text{real} \{ \exp[-j\omega_0\Delta\tau_p] \gamma(z) \}. \quad (2.9)$$

## 2.4. Spectral-Domain OCT (SD-OCT)

In time-domain OCT, a depth-resolved image is achieved by a movable mirror and the coherence length of the light source. In spectral-domain OCT, the interferometric signal is recorded in one shot. The scanned spot is extended to be a 2D (ray) or 3D (wave) probe, and all the points within the probe are contributed in each measurement. This technique is known as a *tomography* [26]. Spectral domain OCT offers a better performance compared to the time-domain OCT in terms of the acquisition speed and the sensitivity [5, 27].

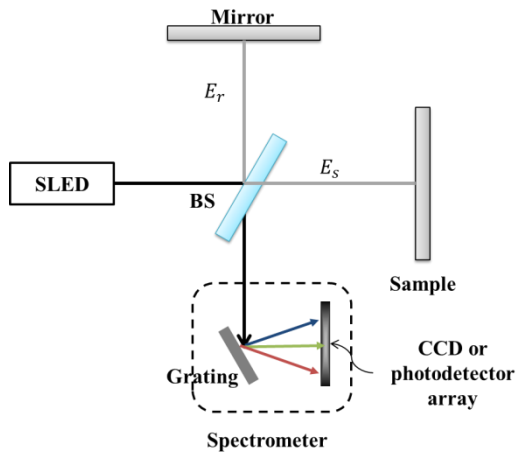


**Figure 2-3 A Michelson interferometer based SD-OCT and a spectrometer**

The implementation of a spectral-domain OCT is very similar to that of the time-domain OCT except for a fixed reference mirror and the use of a spectrometer. The spectral-domain OCT uses broadband source together with a spectrometer which is an instrument that measures the spectrum of light. Figure 2-3 shows a schematic diagram of a Michelson interferometer based spectral-domain OCT. The wavefields in the reference arm and the sample arm can be described by a coherent wave as shown in Eq. (2.10) and Eq. (2.11),

$$E_r(\omega) = A_r(\omega) \exp[-jk_r(\omega)l_r], \quad (2.10)$$

$$E_s(\omega) = A_s(\omega) \exp[-jk_s(\omega)l_s],$$

(2.11)

where  $A_r(\omega)$  and  $A_s(\omega)$  are reflection amplitudes from the reference mirror and the sample,  $k_r$  and  $k_s$  are propagation constants, and  $l_r$  and  $l_s$  is a round-trip optical length of the reference arm and the sample arm, respectively.

At the spectrometer, the spectral components of the interference signal are expanded by a grating and the intensity of each spectral component is measured by an array of photodetectors or a CCD line camera. The intensity of the spectrum interference is frequency dependent and can be described as,

$$I_d(\omega) \propto \text{real} \{S(\omega) \exp[-jk(\omega)\Delta l]\},$$

(2.12)

where  $k(\omega) = k_r(\omega) - k_s(\omega)$ ,  $\Delta l = l_r - l_s$ , and  $S(\omega) = A_s(\omega)A_r(\omega)^*$  is a power spectral density. The space-domain signal is computed by applying an inverse Fourier transform to Eq. (2.12).

## **2.5. Swept-Source OCT (SS-OCT)**

An alternative form of the spectral-domain OCT uses a wavelength-swept laser as the OCT light source. The interference signal is captured sequentially by a photodetector, similar to time-domain OCT. In this section, a background on scalar scattering of light from an object is presented [7]. This background is important for understanding the nature of the backscattered light wave.

### **2.5.1. Analysis of scalar scattering of light from tissue**

The Fercher's analysis is originated from Wolf's paper in 1969. The study indicated that a structure of a weakly scattering object can be determined from the scattering potential of the object through the diffraction theorem [2]. In 1994, Fercher modified the original formulation of Wolf for one-dimension problem [7]. Figure 2-4 shows a drawing of an object being illuminated

by a plane monochromatic laser beam. The incident wavefield on the sample can be described as Eq. (2.13)

$$E^i(\mathbf{r}, \mathbf{k}^i) = A^i \exp[-j\mathbf{k}^i \cdot \mathbf{r}], \quad (2.13)$$

where  $A^i$  is a constant that represents the amplitude of the wave,  $\mathbf{k}^i$  is the wavevector of the plane wave. The amplitude of this vector  $|\mathbf{k}^i| = k = 2\pi/\lambda$  is referred to as the wave-number. Utilizing first-order Born approximation [7, 24], in which the medium is assumed to have weak scattering, the scattered wave can be described as

$$E^s(\mathbf{r}, \mathbf{k}^s) = \int_V P(\mathbf{r}', k) E^i(\mathbf{r}', \mathbf{k}^i) \times G(|\mathbf{r} - \mathbf{r}'|) d^3\mathbf{r}', \quad (2.14)$$

where the Green's function is  $G(|\mathbf{r} - \mathbf{r}'|) = \frac{1}{4\pi} \frac{\exp(-jk|\mathbf{r} - \mathbf{r}'|)}{|\mathbf{r} - \mathbf{r}'|}$ . The scattering potential of the medium is shown in Eq.(2.15) [28].

$$P(\mathbf{r}, k) = -k^2(n^2(\mathbf{r}, k) - 1) \quad (2.15)$$

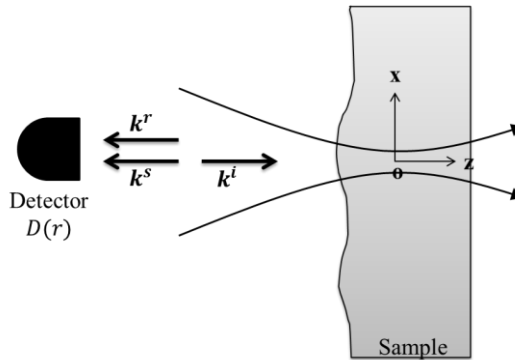


Figure 2-4 A diagram of an object being illuminated by a light wave [7]

The origin  $O$  of the coordinate system  $x, y, z$  is selected at the axis of the illuminating beam at the back surface of the object. The scattered light field is detected at point  $D(\mathbf{r})$  on the  $z$ -axis at a distance  $r$  outside the object. When  $r$  is much larger than the depth  $r'$ , the far field approximation can be applied where the denominator  $|\mathbf{r} - \mathbf{r}'|$  of the Green's function  $G$  can be approximated by  $r$ .

$$G(|\mathbf{r} - \mathbf{r}'|) = \frac{1}{4\pi} \frac{\exp(-jk|\mathbf{r} - \mathbf{r}'|)}{|\mathbf{r} - \mathbf{r}'|} \sim \frac{1}{4\pi} \frac{\exp(-jkr)}{r} \exp(j\mathbf{k}^s \cdot \mathbf{r}') \quad (2.16)$$

From the above approximations, an expression for the scattered field is derived as Eq. (2.17) was obtained

$$\begin{aligned} E^s(\mathbf{r}, \mathbf{k}^s) &= \frac{A^i}{4\pi r} \exp[-jkr] \int_V P(\mathbf{r}', k) \exp[-j(\mathbf{k}^i \cdot \mathbf{r}')] \times \exp[j\mathbf{k}^s \cdot \mathbf{r}'] d^3\mathbf{r}' \\ &= \frac{A^i}{4\pi r} \exp[-jkr] \int_V P(\mathbf{r}', k) \exp[-j\mathbf{K} \cdot \mathbf{r}'] d^3\mathbf{r}', \end{aligned} \quad (2.17)$$

where  $\mathbf{K} = \mathbf{k}^i - \mathbf{k}^s$  is the scattering vector. The scattering potential  $P(\mathbf{r}', k)$  is, later, approximated to be constant in the  $x'$  and  $y'$  direction within the beam waist, and the scattered light has an amplitude that is proportional to the  $z$ -axis only. This is the case when the Fresnel number  $d^2/\lambda D$  of the illuminating beam is much smaller than 1. With these approximations, the integration over  $x'$  and  $y'$  can be replaced by a constant factor  $W$ . From Figure 2-4, the propagation vectors  $\mathbf{k}^i$  and  $\mathbf{k}^s$  are inversely related and the scattering vector  $\mathbf{K}$  can be written as a scalar  $K = 2k$ ,

$$E^s(z, k) = \frac{A^i W}{4\pi z} \exp[-jkz] \int_{-z_{max}}^{z_{max}} P(z') \exp(-j2kz') dz'$$

$$= \frac{A^i W}{4\pi z} \exp[-jkz] \times \text{FT}\{P(z')\}.$$

(2.18)

### 2.5.2. Swept-source OCT

Figure 2-5 shows a schematic diagram of a swept-source OCT where the backscattered wave from the sample interferes with the reference wave and the interference signal is detected by the photodetector. Assuming that the wavefields are plane waves, the reference and sample waves can be described as the following equations:

$$E_r(z_{ref}, k) = A^i \exp(-jkz_{ref}),$$

(2.19)

$$E_s(z_{sample}, k) = \frac{A^i W}{4\pi z_{sample}} \exp(-jk(z_{sample})) \times \text{FT}\{P(z_{sample})\},$$

(2.20)

where  $z_{sample} = z_{ref} + \Delta z$  and  $\Delta z$  is the path length mismatch between the reference and sample arms. At the detector, the intensity of the interference signal between the two monochromatic wavefields can be described as shown in Eq. (2.21):

$$I_D(k) \propto \left( 2|A^i|^2 \frac{W}{4\pi z_{sample}} \right) \text{Re}\{\exp(-jk\Delta z) \times \text{FT}\{P(z)\}\}.$$

(2.21)

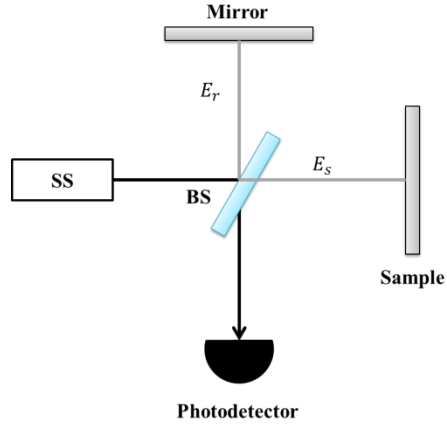


**Figure 2-5 Michelson interferometer based SD-OCT using swept source and a photodetector**

As the frequency of the swept-source is varied, the photodetector measures the interference signal one after the other. When the measurements of all frequencies are obtained, the data is inverted into the space-domain signal by applying an inverse Fourier transform. The space-domain data which shows the structure of the sample can be described as shown in Eq. (2.22).

$$FT^{-1}\{I_D(k)\} = I_D(z) = 2|A^i|^2 \frac{W}{4\pi z_{sample}} P(z_{sample})$$

(2.22)

## **2.6. Resolution and scanning depth of OCT**

Resolution of an imaging system is the closest distance between two points in the object that can be discerned [1]. This distance is determined by the width of a blurred spot or a point spread function (PSF). The resolutions of an OCT system can be divided into an axial resolution and a transverse resolution.

### **2.6.1. Axial resolution**

In time-domain OCT, where a finite bandwidth light source is used for illumination, the axial resolution is defined by the bandwidth of the light source. The relationship between the spectral

bandwidth, or the correlation function  $\gamma(z)$ , and the coherence length can be explained as follows.

The light source that has a Gaussian power spectral density  $S(\omega - \omega_0)$  can be described as shown in Eq. (2.23) [25].

$$S(\omega - \omega_0) = \sqrt{\frac{2\pi}{\sigma_\omega^2}} \exp\left[-\frac{(\omega - \omega_0)^2}{2\sigma_\omega^2}\right], \quad (2.23)$$

where  $\omega_0$  is the center frequency and  $2\sigma_\omega$  is the standard deviation power spectral bandwidth.

The spectral density distribution has a normalized unit power as,

$$\int_{-\infty}^{\infty} S(\omega) \frac{d\omega}{2\pi} = 1. \quad (2.24)$$

By substituting the Gaussian spectral density into the correlation function in Eq. (2.9), the photocurrent becomes

$$\begin{aligned} I_d(\Delta l) &\propto \text{real}\{\exp[-j\omega_0\Delta\tau_p] \gamma(z)\} \\ &\propto \text{real}\left\{\exp[-j\omega_0\Delta\tau_p] \exp\left[-\frac{\sigma_\omega^2\Delta\tau_g^2}{2}\right]\right\}, \end{aligned} \quad (2.25)$$

where the aurocorrelation function  $\gamma(z) = \exp\left[-\frac{\sigma_\omega^2\Delta\tau_g^2}{2}\right]$ . The photocurrent signal in Eq. (2.25)

can be seen as a carrier,  $\exp[-j\omega_0\Delta\tau_p]$ , that is modulated by an envelope,  $\exp\left[-\frac{\sigma_\omega^2\Delta\tau_g^2}{2}\right]$ . For

the detector to see the interference fringes, the group delay mismatch should fall within this Gaussian envelope,

$$-\frac{1}{\sigma_\omega} < \Delta\tau_g < \frac{1}{\sigma_\omega} \xrightarrow{\text{yields}} -\frac{1}{\sigma_\omega} < \frac{\Delta l}{v_g} < \frac{1}{\sigma_\omega}.$$

(2.26)

From the relationship in Eq. (2.26), the maximum optical path difference (OPD) between the two arms is determined by

$$\Delta l_{max} = l_c = \frac{v_g}{\sigma_\omega}$$

(2.27)

or  $\Delta l = \frac{c}{\sigma_\omega}$  when the group velocity  $v_g$  is equal to the speed of light  $c$  in free-space propagation.

It shows that the OPD is inversely proportional to the bandwidth of the light source. This maximum OPD determines the axial resolution of the system. The relationship between the coherence length and the spectral density of the light source that has a center wavelength at  $\lambda_0$  and wavelength bandwidth  $\Delta\lambda$  can be described as [25],

$$l_c \cong \frac{\lambda_0^2}{\Delta\lambda}.$$

(2.28)

The full-width at half-maximum of the coherence length is given by

$$l_{FWHM} = \frac{2 \ln 2}{\pi} \left( \frac{\lambda_0^2}{\Delta\lambda} \right).$$

(2.29)

### 2.6.2. Transverse resolution

The transverse resolution of an imaging system is determined by the size and shape of the lens aperture [1]. A point spread function (PSF) of an imaging system is the Fourier transform of its pupil function. For coherent illumination (SS-OCT), the PSF can be expressed as

$$h(x, y) \propto P\left(\frac{2\pi}{\lambda d}x, \frac{2\pi}{\lambda d}y\right). \quad (2.30)$$

where  $P$  is the Fourier transform of the pupil function. For a circular aperture or a circular lens with a focal length  $f$ , the pupil function is expressed by a Bessel function, and the width (spot size) of its PSF can be expressed as,

$$\rho = 1.22\lambda \frac{f}{D} = 1.22\lambda F_{\#} = 0.61 \frac{\lambda}{NA}, \quad (2.31)$$

where  $f$  is the focal length of the lens and  $D$  is the diameter of the lens aperture. Typically, the specification of a lens can be expressed in terms of an F-number or numerical aperture as shown in Eq. (2.32) and Eq.(2.33), respectively

$$F_{\#} = \frac{f}{D}, \quad (2.32)$$

$$NA = \sin \theta = \frac{f}{2D}. \quad (2.33)$$

For an incoherent illumination (TD-OCT and SD-OCT), the PSF of the imaging system is described by,

$$h(x, y) \propto \left| P\left(\frac{2\pi}{\lambda d}x, \frac{2\pi}{\lambda d}y\right) \right|^2. \quad (2.34)$$

For a circular aperture, the width of the spot size is the same as in coherent illumination, which can be described as

$$\rho = 0.61 \frac{\lambda}{\text{NA}}$$

(2.35)

### 2.6.3. Imaging depth of OCT

In time-domain OCT, the imaging depth directly depends on the time delay values provided by the system's delay line. In spectral domain OCT, imaging depth is limited by the spectrometer. In spectral-domain OCT, the sampling interval  $\delta_r k$  ( $k$  is the wave number) refers to the spectral resolution of the spectrometer. In swept-source OCT, the spectral sampling interval refers to the instantaneous linewidth of the swept-source. The effects of the spectral resolution have been evaluated in [29].

## Chapter 3

### Design and implementation of the time-domain OCT system

#### 3.1. Introduction

As described in Chapter 2, one of the most common interferometers that is used in an OCT is the Michelson interferometer. In section 3.2, we discuss how the standard Michelson interferometer is not a good option for OCT. Then, we discuss studies on evaluating the performances of new OCT designs based on Mach-Zehnder interferometer. From the studies, it has been shown that the Mach-Zehnder interferometer based OCT could yield a higher signal-to-noise ratio (SNR). Section 3.3 explains our implementation of an OCT system based on the Mach-Zehnder interferometer. The section is divided into two subsections. Section 3.3.1 explains the optical hardware module. This includes the setup overview, lists of the optical components used in the system, and the description of each component. Section 3.3.2 explains the data acquisition module. This section describes the architecture of the hardware and the data flow in the LabView Virtual Instrument (VI) state machines during the acquisition process.

#### 3.2. Optical design of time-domain OCT systems

In Michelson interferometer based OCT configurations, 75% of the optical power from the supplied source is typically wasted [30]. This wasted optical power affects the signal-to-noise ratio (SNR) and image quality. The SNR of an OCT system is affected by two factors. The first factor is the optical power of the source; the higher the power, the higher the SNR. The second factor is the bandwidth of the detection electronics; the higher the bandwidth of the detector, the lower the SNR. Therefore, conserving the optical power in an OCT system is necessary in order to enhance its SNR especially when a turbid sample is imaged.

In a study by Rollins and Izatt, the SNR values of different interferometer designs used in OCT were evaluated [30]. Their mathematical analysis showed that the SNR will be high when the

optical power in the reference arm is low. Therefore, in most interferometer designs for OCT, most of the light is directed to the sample arm to enhance the back-reflected signal by the sample. They also showed that balanced optical detection using a Mach-Zehnder interferometer achieves better sensitivity over Michelson interferometer based OCT. For unbalanced optical detection, the SNR and sensitivity will depend on the splitting ratio  $\alpha$  of the OCT optical coupler.

The SNRs of Mach-Zehnder and Michelson based OCT configurations were studied in more depth for the case of quadrature interferometry [11]. Under ideal balanced optical detection, results show that SNR for a quadrature Mach-Zehnder interferometer is higher than that of a Michelson interferometer. In case of the unbalanced detection, the SNR for both configurations is almost the same with a small improvement for the Mach-Zehnder configuration. This configuration has been used to implement a swept-source OCT with unbalanced differential optical detection [10].

### **3.3. Implementation of our time-domain OCT system**

#### **3.3.1. Optical module**

The schematics of our OCT system is shown in Figure 3-1. The power supplied by a light source is divided by a  $2 \times 2$  fused-fiber coupler into two arms, known as the reference beam and the sample beam. A 90/10 fiber coupler is used, such that 90 percent of the light power goes to the sample arm and 10 percent of it goes to the reference arm. An optical attenuator (optional) could be placed in the reference arm and used to enhance the SNR of the signal as explained in section 3.2. At the output of the delay line, a polarization controller is used to control the polarization state of the light in the reference arm to match with the polarization state of the light coming from the sample arm, since a difference in the polarization could have a negative effect on axial resolution [31].

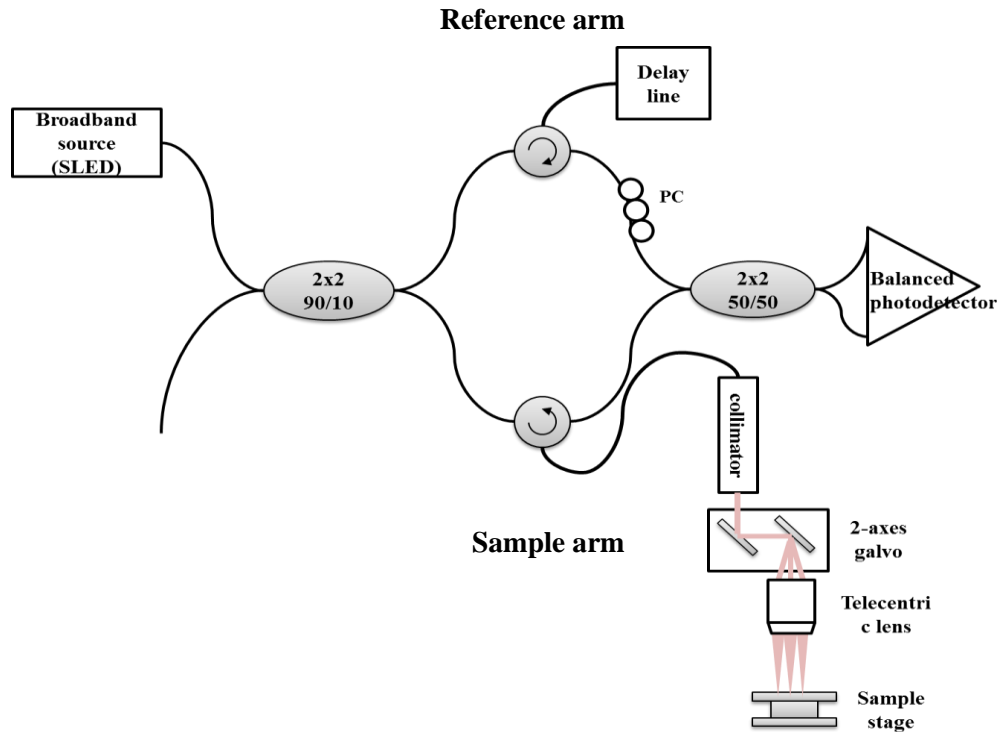


**Figure 3-1 A schematic of the TD-OCT with balanced detection**

A movable mirror is required for axial scanning (A-scan). In our setup, the optical delay line serves as our movable reference mirror. In the sample arm, the light is collimated by a collimating lens. The collimated light incidents on a dual-axis galvo-mirrors and is redirected to telecentric objective lens. The objective lens focuses the light onto the sample and the back-reflected light is collected by the lens and focused into a circulator. The outputs from the two circulators are recombined by a 50/50 fused-fiber coupler before they are detected by a heterodyne balanced detector.

### **3.3.1.1. Optical components used in our TD-OCT system**

This section describes operations of some optical components that were used in the time-domain OCT system. The summary of the components are shown in Table 3-1 where the manufacturers and part numbers are provided for future reference.

**Table 3-1 Lists of optical components**

<b>Optical component</b>	<b>Manufacturer</b>	<b>Part number</b>	<b>Task</b>
Superluminescent diode (SLED)	Novacam Technologies Inc.	N/A	Light source, 15mW, 1300nm ( $\Delta\lambda=90$ nm)
2x2 50/50 coupler	OZ optics	FUSED-22-1300-9/125-50/50-3A3A3A3A-1-1	The coupler splits the beam into 1:1 ratio
2x2 90/10 coupler	OZ optics	FUSED-22-1300-9/125-90/10-3A3A3A3A-1-1	The coupler splits the beam into 9:1 ratio
polarization independent fiber optic circulator	OZ optics	FOC-12N-111-9/125-SSS-1310-50-3A3A3A-1-1	The circulator is a three-port device that is used to direct the signal entering from one port to exit the next port
Optical attenuator (optional)	OZ optics	BB-500-11-1300/1550-9/125-S-40-3A3A-3-0.5	The attenuator is used to suppress the power of the light
Optical delay line	Novacam Technologies Inc.	N/A	Optical delay line provides 3.5mm axial scan (in air)
FC/APC fiber collimation package	Thorlabs	F280APC-C	The collimator is used to give a collimated beam (plane wave)
XYZ $\theta_x\theta_y$ Compact Lens Positioner	Newport	LPV-1	Five axis lens positioner is used with the collimation package for beam alignment
lens holder	custom	N/A	This custom-made lens holder is used for accommodating the collimator and to be able to put in the compact lens positioner

5mm XY galvo mirrors	Cambridge Technology	N/A	The galvo mirrors allow the scanning in x and y axis
Peg-joining linear stage	Newport	M-460P-XYZ-05	The galvo mirrors are attached to the linear stage for positioning
3X OCT Scan Lens	Thorlabs	LSM04	The telecentric property of the focusing point on the same plane is obtained using the scan lens.
XYZ $\theta_x\theta_y$ Lens Positioners	Newport	LP-1A	Five axis lens positioner is used with the scan lens for optical alignment
lens holder	custom	N/A	This custom-made lens holder is designed for LSM04 to be able to put in the lens positioner
Big Lab Jack	Newport	9204-M	This is used to place the sample. The height can be adjusted
Balanced photoreceiver	Newport	1817-FC	80 MHz balanced photoreceiver
Two-paddle polarization controller	Thorlabs	FPC020	To control the polarization of the fiber for visualization

- **Optical source**

The optical source used in the system is a superluminescent diode (SLED) supplied from Novacam Technologies, Inc. The power supply that is needed to operate the SLED is 5V. The power of the source is 15 mW when measured directly from the output fiber (yellow fiber). The central wavelength is 1310 nm and the spectrum bandwidth is 90 nm. The bandwidth of the source determines the axial resolution (or coherence length) of the system. The axial resolution of our system is equivalent to 8.41  $\mu\text{m}$  (in air).

- **2D galvo mirrors**

Lateral scanning of the OCT system is provided by a 2D-galvanometer scanner or galvo-mirrors from Cambridge Technology (model 6220H). 2D-galvanometer scanner consists of three main components; a 5mm mirror set, mirror mounts, and a dual-axis servo driver connected to a 24V power supply.

To control the galvo-mirrors, the mirrors rotation angles depends on the input waveform signal and power. The servo driver needs 0.5 V input for every 1 mechanical degree of rotation. The system gives maximum of  $\pm 15$  mechanical degrees (or  $\pm 30$  optical degrees). The servo driver is typically scaled so that the analog input range for the maximum angle is  $\pm 10$  V.

- **Optical delay line**

An optical delay line (Novacam Technologies, Inc.) is used in the system to perform the axial object scanning. A 12 V power supply is needed to operate the delay line. The maximum scanning speed of this delay line is 2.1 kHz and it has 3.5 mm scanning range. The scanning speed is adjustable from the hardware (blue knob) as shown in Figure 3-2. The optical path length in air of the delay line is approximately 1700mm (round trip of 3400 mm) in air.

The operation principle of this delay line is described in the paper by Lamouche *et al.* [32]. The optical path length (OPL) varies as five rhombic prisms inside the delay line rotate. In one full

cycle (at maximum speed of 210 Hz), the light travels through each prism and is redirected back by two different paths, channel 1 and channel 2, so that each prism provides two A-scans. With five prisms present, one rotation gives 10 A-scans where five A-scans belong to channel 1 and the other five belong to channel 2. Therefore, the scanning speed of the delay line is 2.1 KHz or 2,100 A-scans per second.

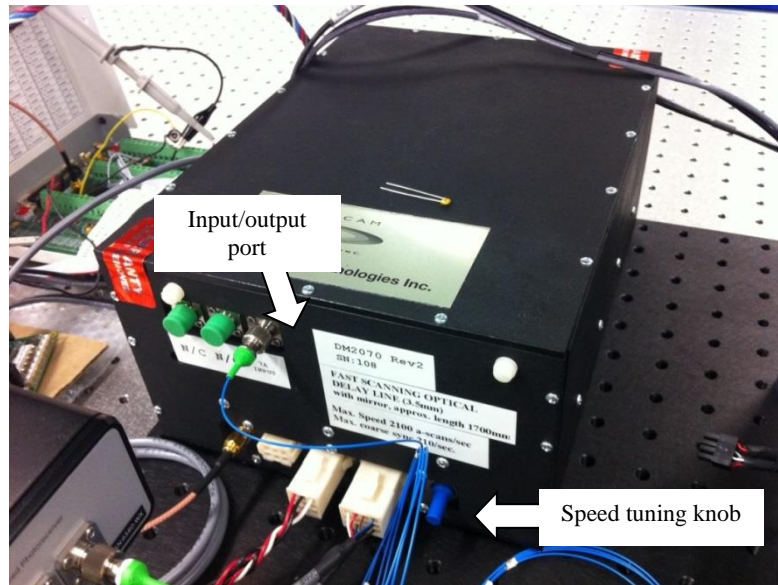


**Figure 3-2 Optical delay line**

Figure 3-3 shows two signals from the delay line which were captured on an oscilloscope. The coarse sync signal corresponding to a full rotation cycle of the delay line is shown in blue. The digital/analog sync signal corresponding to each rotation of a single rhombic prism is shown in green. As shown in the figure, there are five green peaks in one cycle, because five rhombic prisms are present inside the delay line. These electrical signals from the delay line are important for synchronization of the data acquisition module.

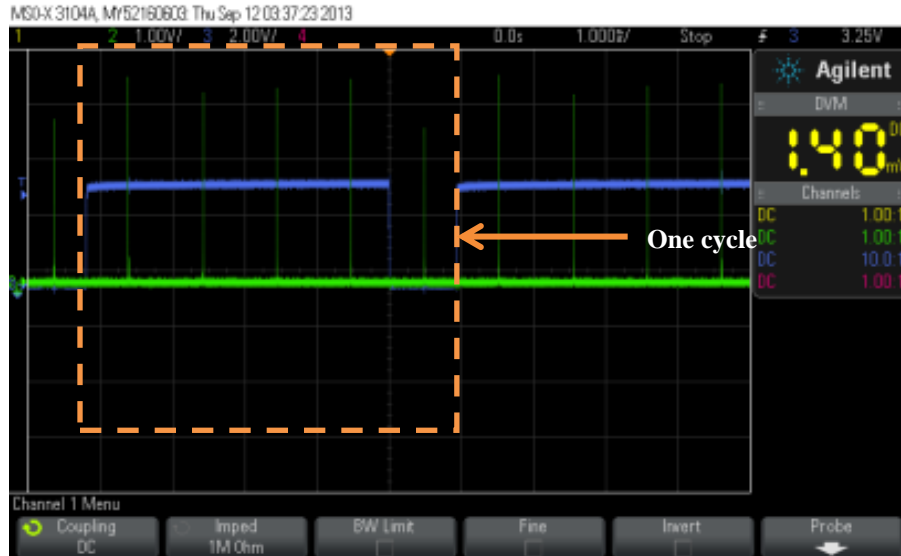


**Figure 3-3 Signal of coarse sync and digital/analog sync of the delay line**

- **Telecentric lens**

The objective lens that is used in the OCT system to focus a beam on the sample is a telecentric lens, LSM04 from Thorlabs, Inc. A telecentric lens is desirable in a laser scanning system such as OCT because it provides a flat imaging plane as the laser beam is scanned across a sample. The spot size of the focused beam, which determines the lateral resolution of the system, is nearly constant over the field-of-view (FOV). This results in a constant lateral imaging resolution and less imaging distortion than using an ordinary objective lens. The specification of the telecentric lens is shown in Table 3-2 [33] and its schematic is shown in Figure 3-4.

**Table 3-2 Specification of the telecentric lens used in our OCT system**

<b>Magnification</b>	×3
<b>Center wavelength</b>	1315 nm
<b>Wavelength range</b>	±65 nm
<b>Effective focal length</b>	53.99 mm
<b>Working distance</b>	42.3 mm
<b>Scanning distance</b>	18.9 mm
<b>Pupil size (<math>1/e^2</math>)</b>	4 mm
<b>Depth of View (DOV)</b>	1.15 mm
<b>Field of View (FOV)</b>	14.1 mm × 14.1 mm
<b>Parfocal distance</b>	80.8 mm
<b>Mean spot size (<math>1/e^2</math>)</b>	35 μm
<b>Scan angle</b>	7.5°

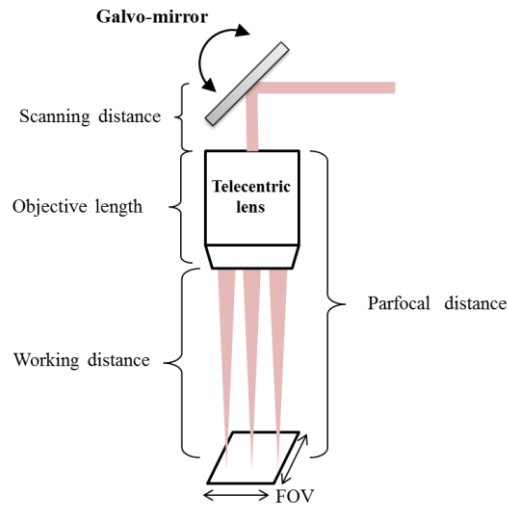


**Figure 3-4 A schematic of the telecentric lens used in our OCT system**

- **Optical circulator**

An optical circulator is a special fiber that consists of three ports as shown in Figure 3-5. It is designed for the light to enter one port and exit the next port. For example, the light that enters

Port T will exit the fiber from Port 1. In our system, the circulators are used in the reference arm and the sample arm.

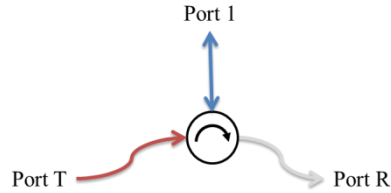


**Figure 3-5 Optical circulator**

In the reference arm of our system, the light enters the circulator from Port T and exits the fiber at Port 1. Port 1 is connected to the delay line; therefore, the reflected light from the mirror is redirected into the circulator at Port 1 and exits the fiber at Port R. In the sample arm of our system, the light also enters the circulator from Port T. Port 1, where the light exits, is connected to a collimator and the collimated light will be directed to the galvo-mirrors for lateral scanning the sample. The reflected light from the sample will be redirected into the circulator via Port 1 and the light will exit the circulator through Port R.

- **Fused fiber couplers**

Our OCT system uses two kinds of 2x2 fused fiber coupler; 50/50 coupler and 90/10 coupler. The diagram of 2x2 coupler is shown in Figure 3-6 (a). The 90/10 coupler is connected to the source to divide the power into 90 percent and 10 percent. The coupler also serves as a beam combiner. The 50/50 coupler is used to recombine the reflected lights from the reference arm and the sample arm, before dividing it equally for balanced detection.

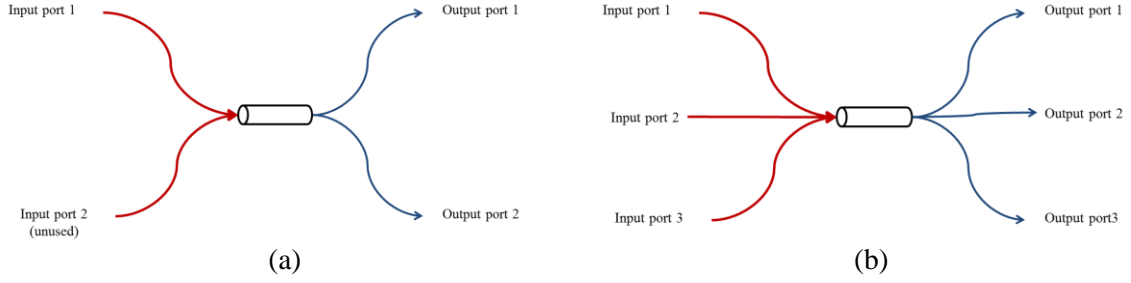


**Figure 3-6 Schematics of (a) 2x2 fused fiber coupler (b) 3x3 fused fiber coupler**

The design of the system can be modified and becomes a quadrature OCT by replacing the 50/50 coupler with a  $3 \times 3$  coupler in Figure 3-6 (b). The power of the light will be divided equally into three output ports (0.33:0.33:0.33). The  $3 \times 3$  coupler also introduces phase difference between the three outputs which is an important key in obtaining the real and imaginary signals from the quadrature OCT. The principle and the setup of the quadrature OCT system will be explained in Chapter 5.

- **Polarization controller**

As mentioned before, the difference in polarization between the lights coming from the reference arm and the sample arms affects the axial resolution of the system [31]. Our system employs a miniature 2-paddle polarization controller which is placed in the reference arm. Thorlabs's polarization controller uses stressed-induced birefringence in changing the polarization. This can be achieved by putting the fiber in two fiber spools to create two independent quartered wave plates  $\left(\frac{\lambda}{4}\right)$ . The retardance  $\phi$  of each paddle can be calculated from the following equation [33]

$$\phi(\text{Waves}) = \frac{\pi a N d^2}{\lambda D}, \tag{3.1}$$

where  $a$  is a constant (0.133 for silica fiber),  $N$  is the number of loops,  $d$  is the fiber cladding diameter,  $\lambda$  is the wavelength, and  $D$  is the loop diameter. The plot of retardance per each paddle when the fiber cladding diameter is  $125 \mu\text{m}$  and the loop diameter of the spool is  $18 \text{ mm}$  is shown

in Figure 3-7. The operating wavelength of the fibers used in our system is between 1290-1650 nm. Therefore, fiber is needed to be enfolded in the spool three times to create a quarter waveplate. The polarization of the transmitted light in a single mode fiber can be altered by rotating the paddles.

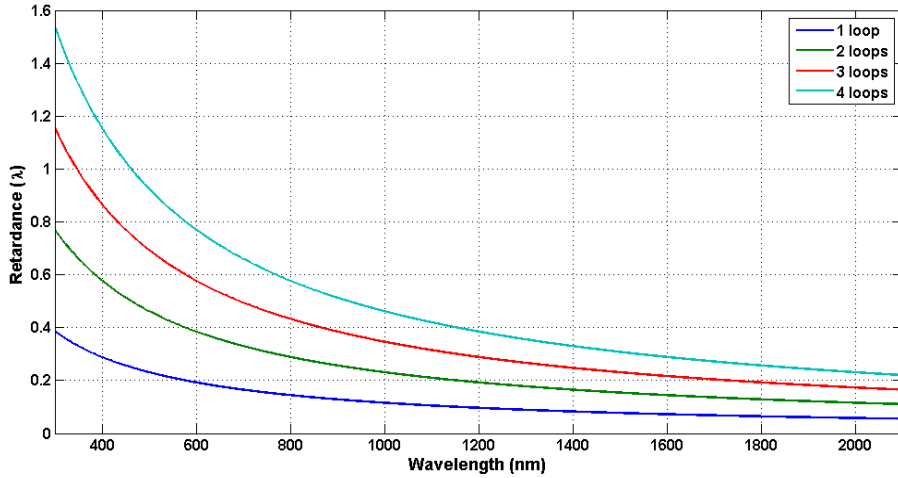


Figure 3-7 Plot of retardance (wave) of each paddle ( $d = 125 \mu\text{m}$ ,  $D = 18\text{mm}$ )

- **Heterodyne balanced optical detector**

A balanced detection technique is used in our OCT system for noise reduction purpose. In general, balanced photodetectors consist of two matched photodiodes. The two photodiodes detect the optical signals with  $\pi$  phase difference coming from the  $2 \times 2$  coupler. The photocurrent of the two photodiodes are subtracted from each other,  $I_1 - I_2$ . Therefore, the DC interference terms are cancelled out.

The balanced detector used in our system is the 1817 FC model from New Focus which uses a  $\pm 15$  V DC power supply [34]. These PIN junction photodiodes are made of InGaAs, in which the responsivity bandwidth is between 900 – 1700 nm. The 3-dB bandwidth is 80MHz. The minimum Noise-Equivalent Power (NEP), which is the minimum optical signal that can be detected by the photodetectors, is  $2.5 \text{ pW}/\sqrt{\text{Hz}}$ . The conversion gain of its amplifier is  $4 \times 10^4 \text{ V/W}$ , and the amplifier will reach saturation levels when the difference input between the

two photodiodes is approximately 110  $\mu\text{W}$  (for responsivity of 0.5 A/W). The maximum power per photodiode (damage threshold) is 5mW.

### **3.3.1.2. Description of our optical setup**

An optical mechanism to match the optical path length (OPL) of the reference and sample arms as shown in Figure 3-1 is an essential in building low coherence interferometer. In our system, the interferometer is implemented using optical fibers, couplers, and circulators. These fiber based components have standard fiber lengths which eases such OPL matching. In the reference arm, an optical circulator (blue fiber) is connected to the input/output port of the delay line. The round trip of the light that travels inside the delay line is 3400 mm (in air).

To match the OPL of the sample arm to the OPL of the reference arm, two extra optical fibers (1 m fiber) were needed in the sample arm. Most fibers used in our set up are Corning SMF-28 fibers, where the refractive index at 1310 nm is 1.4670 [35, 36]. Therefore, the OPL in this 2-m fiber is 2934 mm. In our set up, the 2 m fiber is placed after the output from the 90/10 fiber coupler. An attenuator having a 1 m fiber was placed in the reference arm, so another 1 m fiber was needed in the sample arm to balance this additional OPL.

The design of the sample imaging probe is shown in Figure 3-8 (a). It consists of a collimator, 2D galvo-mirrors, telecentric lens, and a sample holding stage. The collimator is placed in a compact five-axis lens positioner. The telecentric lens is placed in a five-axis lens positioner. The 2D galvo-mirrors are placed on a linear translation stage. For optimal image quality, it is necessary to account for the telecentric lens parameters, such as its scanning distance and the parfocal distance. The working distance of this telecentric lens, from the output of the lens to the sample stage, is 42.30 mm. The length of the lens is 38.5 mm and its parfocal distance, which is the sum of its working distance and its physical length, is 80.8 mm. The scanning distance is 18.9 mm which is the distance from the entrance pupil of the galvo mirrors to the lens' entrance pupil. Our

imaging probe uses a two axis galvo-mirror set; hence, its entrance pupil is located between the two galvo mirrors. The length of the collimator is 22.1 mm.  $\Delta l$  is the distance from the output of the collimator to the entrance pupil that is located between the two galvo mirrors. This distance  $\Delta l$  can be adjusted by the translation stage or by the compact lens positioner of the collimator to match the OPLs of the reference and the sample arm. Figure 3-8 (b) shows the actual optical imaging probe. When the OPLs of the interferometer arms are matched, an interference signal will appear as shown in Figure 3-9.

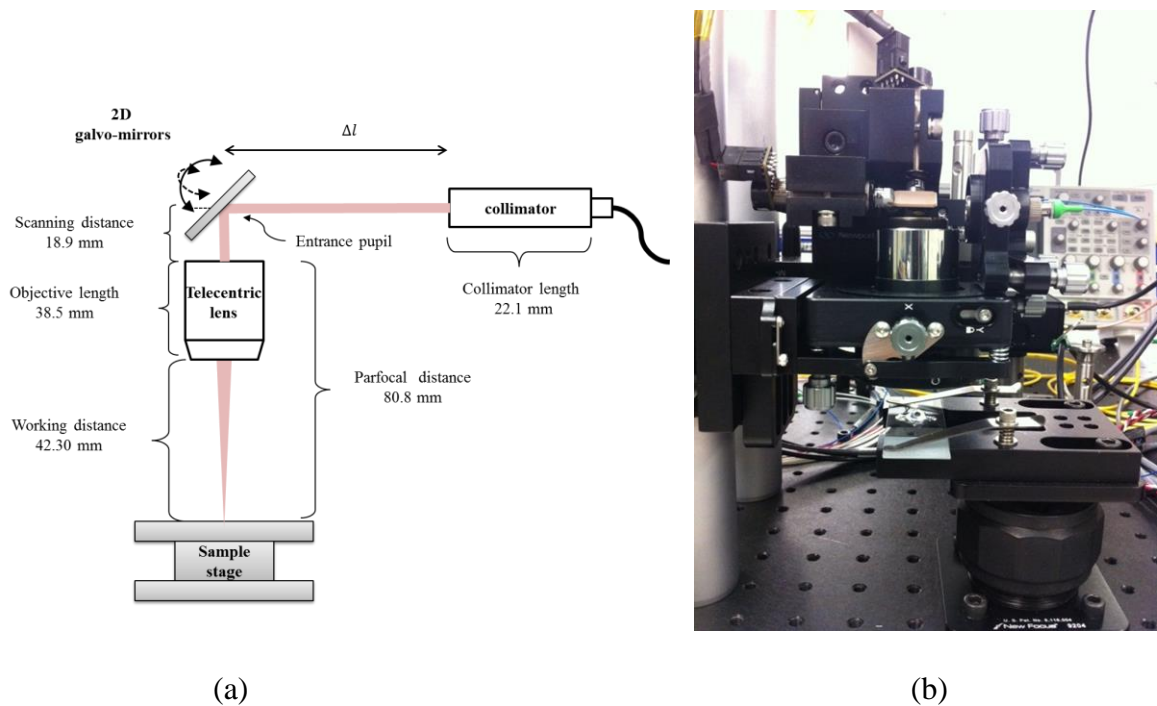


**Figure 3-8 The sample imaging probe (a) schematic diagram (b) actual setup**

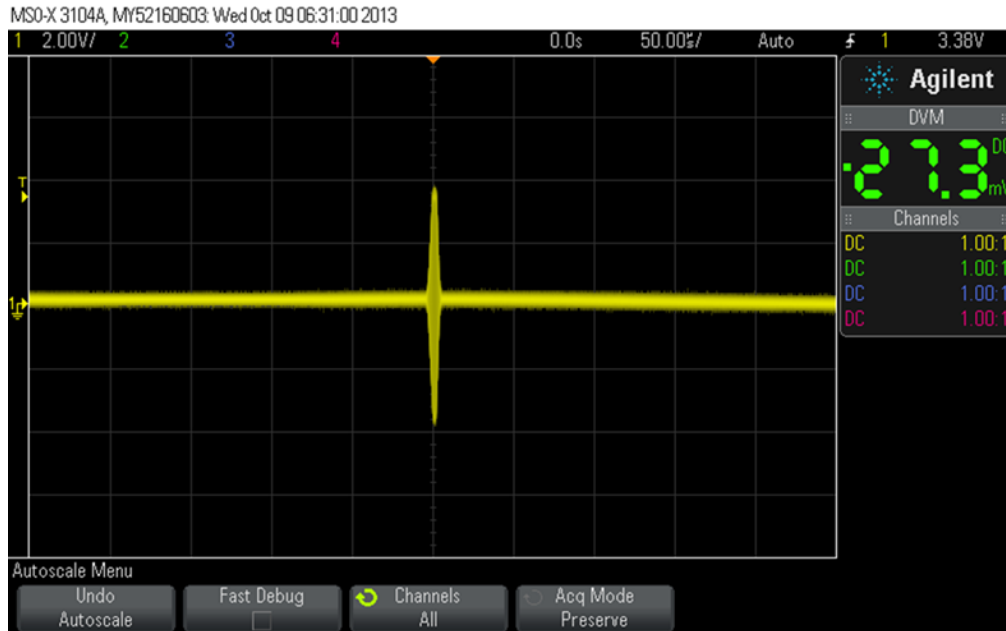


**Figure 3-9 Interferometric signal captured from an oscilloscope**

### 3.3.2. Data Acquisition module

For data acquisition, some components in optical module, e.g., galvo-mirrors, delay line, and detector, are connected to and controlled by a computer. A virtual instrument (VI) program has been developed by one of my colleagues, Fernando Saccon, for synchronizing the components in data acquisition. This section explains the relationship between optical hardware and computer and the work flow of the VI program. The implementation detail can be found in our “Integrated Computational Imaging Lab” internal report [37].

### 3.3.2.1. Architecture of Data Acquisition module

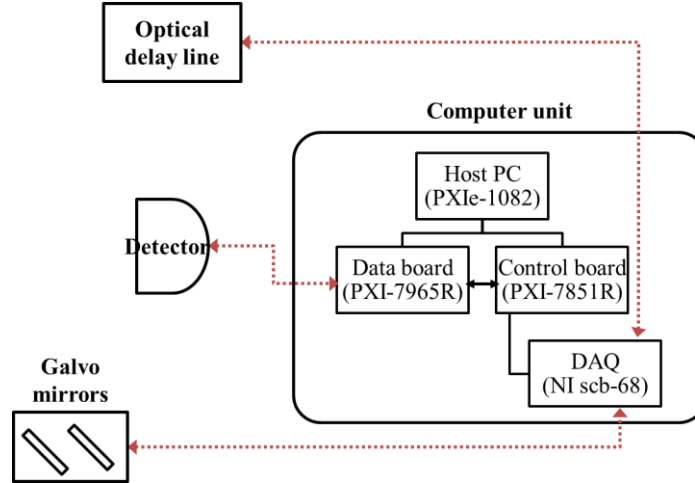


**Figure 3-10 A diagram of the computer unit**

Figure 3-10 shows a schematic of the data acquisition hardware. It includes a host PC (PXI-1082), a data board (PXI-7965R), a control board (PXI-7851R), and a data acquisition connector block (NI scb-68). In the host PC, a LabVIEW Virtual Instrument (VI) program, known as the Host VI. During the data acquisition, the data board and the control board is controlled by the host VI. These boards are equipped with Field Programmable Gate Array (FPGA) chips which allow the user to customize them for measurement and control. They allow full onboard decision making which is direct and fast. Figure 3-11 shows images of these hardware boards.



(a)



(b)

**Figure 3-11 (a) PXI-8120 with PXI-7965R and PXI-7861R (installed inside PXI-8120) and (b) connections inside the DAQ NI scb-68**

Analog and digital functionality of these boards can be configured through National Instruments' LabVIEW graphical language and LabVIEW FPGA module. The data board is connected to the detector to collect the digital interference signal. The DAQ is connected to the galvo-mirrors and the delay line, and the DAQ itself is connected to the control board. This control board serves two purposes; reading feedback signals from the galvo-mirrors (positions of mirrors) and the delay line (the starting point of the A-scan) and sending a command to the galvo-mirrors for moving the mirrors (B-scans). During data acquisition, the data board and the control board are synchronized by hardware trigger lines. The acquired data are queued to the host PC to be processed and saved on its hard drive. Complete lists of DAQ connections are shown in Table 3-3.

**Table 3-3 NI SCB-68 connections**

<b>Analog inputs</b>	
AI0	Delay line analog sync
AI1	Delay line Coarse sync
AI2	Delay line Digital sync
AI3	Galvo Y position feedback
AI4	Galvo X position feedback
AI5	Galvo Y motor current
AI6	Galvo X motor current
AI7	Not used
<b>Analog outputs</b>	
AO0	Galvo X motor (fast)
AO1	Galvo Y motor (slow)
AO2 to AO7	Not used
<b>Digital inputs</b>	
DIO0	Y motor fault status
DIO1	X motor fault status
DIO2 to DIO7	Not used
<b>Digital outputs</b>	
DIO8	Galvo mute in
DIO9 to DIO15	Not used

### 3.3.2.2. Virtual Instrument (VI) state machines

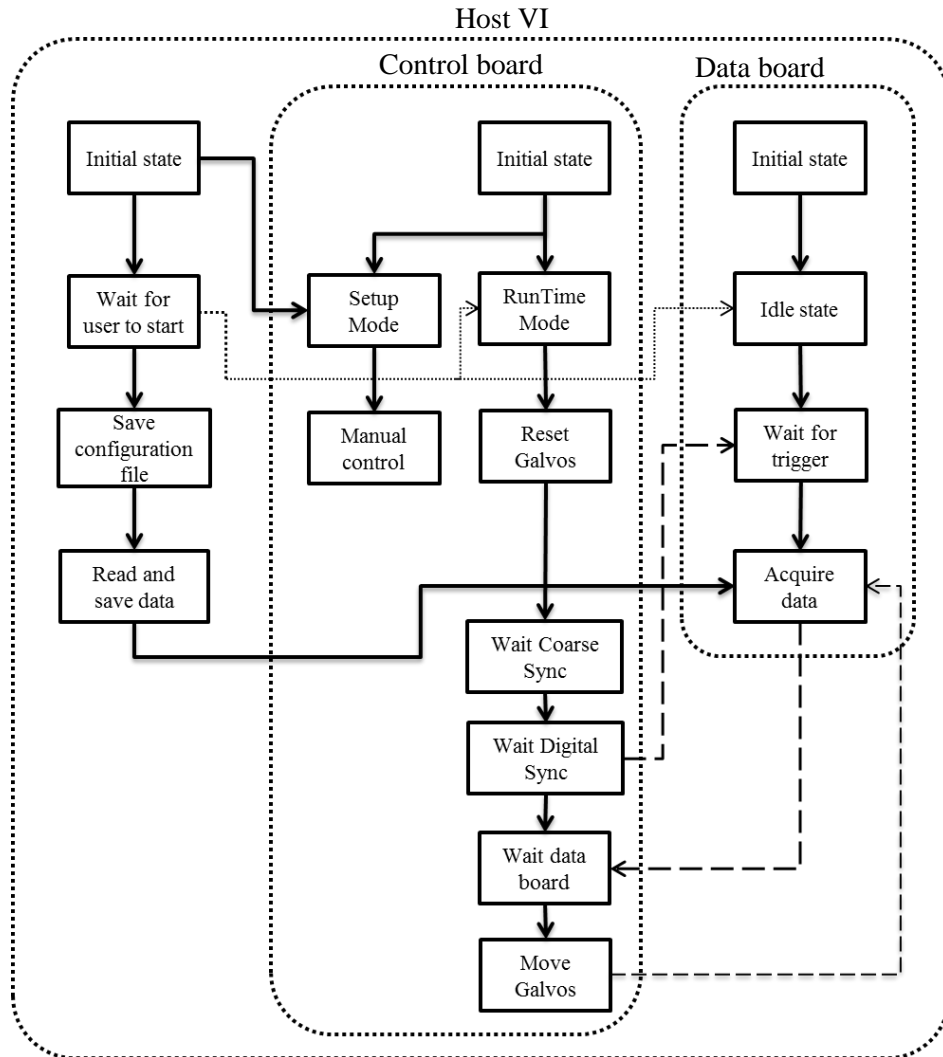


**Figure 3-12 VI flowchart**

This section describes how the data flow happens in the VI program. The program was implemented using LabVIEW on a host computer (Host PC). Figure 3-12 shows the flowchart of the program which consists of three main parts; Host VI, FPGA based control board, and FPGA based data board. Host VI is the main program to control the acquisition process of the control and data boards. These two boards work synchronously through their hardware trigger. In the figure, solid lines represent data flow, dashed lines represent communication between control and

data boards via hardware triggers, and dotted lines show a command by the user that affects these two boards.

The VI programs start in their initial states where user can start the acquisition process through a Graphical User Interface (GUI) by choosing the “*Setup Mode*” to configure the system if needed.

In the “*RunTime mode*”, the host VI will wait for the user to press the “*Run*”. Once a user presses the “*Run*” button in the GUI, the Host VI will save the configuration file of the system, the control board will move the galvo-mirrors to the initial positions, and the control board will be waiting for a trigger from the delay line. When the mirrors are at their initial position, the control board will wait for the coarse and digital triggers signal from the delay line. When the digital trigger is obtained, the control board will trigger the data board to start acquiring an A-scan and the control board itself will wait for the data board to finish this A-scan. When the data board has finished acquiring an A-scan, it will send a trigger to the control board to move the galvo mirrors to the next position. This ensures that the data board will start to acquire A-scans at the correct time. This process will go on until the complete field of view is scanned or until the user decides to terminate the operation by pressing the “*Run*” button again. The GUI will be described in detail in the next chapter.

# Chapter 4

## Graphical User Interface (GUI) of our time-domain OCT system and imaging examples

### 4.1. Introduction

This chapter describes the GUI of our time-domain system. It will explain the components of the GUI so a user would be able to use our OCT system to acquire images. Also example images acquired by our OCT system will be shown in section 4.3.

### 4.2. Graphical User Interface

The GUI of our OCT system can be used in two modes “*Setup Mode*” and “*Run Mode*”. “*Setup Mode*” is used for configuring the acquisition system, “*Run Mode*” is used for acquiring data.

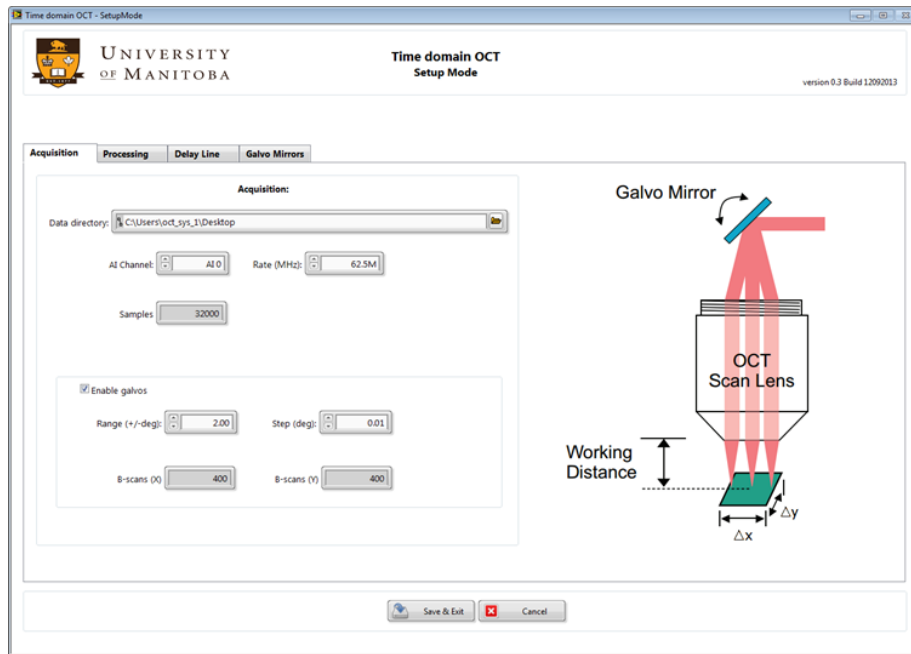


Figure 4-1 “Welcome page” GUI of our OCT system

#### 4.2.1. Setup Mode GUI

“*Setup Mode*” is used to set up the operation of the acquisition system. This step is required when the measurement is performed for the first time. The “*Setup Mode*” consists of four LabView

interface pages: “*Acquisition*”, “*Processing*”, “*Delay Line*”, and “*Galvo mirrors*”. The main set up of the system is in the “*Acquisition*” page which allows setting up several parameters.



**Figure 4-2 Setup Mode GUI – “Acquisition”**

Figure 4-2 shows the parameters that could be set in the “*Acquisition*” page.

- “Data directory” box allows the user to choose a folder for data to be saved.
- “AI Channel” indicates the data board channel to be used to acquire the data.
- “Rate (MHz)” is for choosing the acquisition rate of the data board. The number of sample per A-scan is shown in the “Samples” which is the gray box under AI channel.
- “Enable galvos” determines the use of galvo mirrors in transverse scanning. The scanning range is set in degrees and their spatial resolution is determined by the step. The number of B-scans in x and y direction are shown in the gray boxes, B-scans (X) and B-scan (Y).

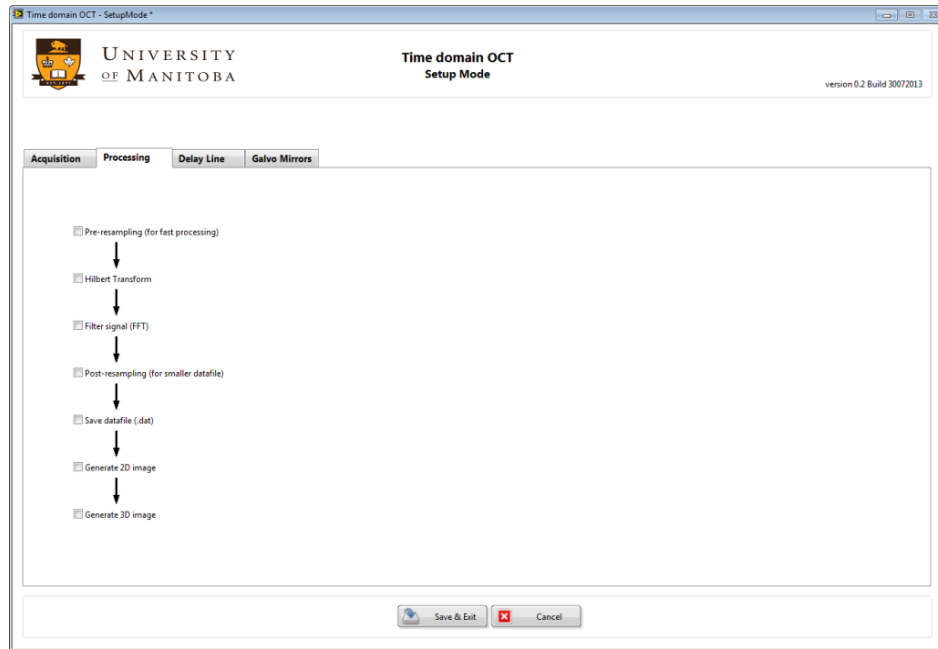


**Figure 4-3 Setup Mode GUI – “Processing”**

In the “*Processing page*”, a user can choose different signal processing algorithms to be applied to the raw signal.

- “Pre-resampling” eliminates some samples that are acquired from the data board.
- “Hilbert transform” extracts the envelope of the signal.
- “Filter signal” applies low pass filter for reducing the noise.
- “Post-resampling” eliminates some samples after applying the Hilbert transform and low pass filter.
- “Save datafile (.dat)” saves data in a text file.

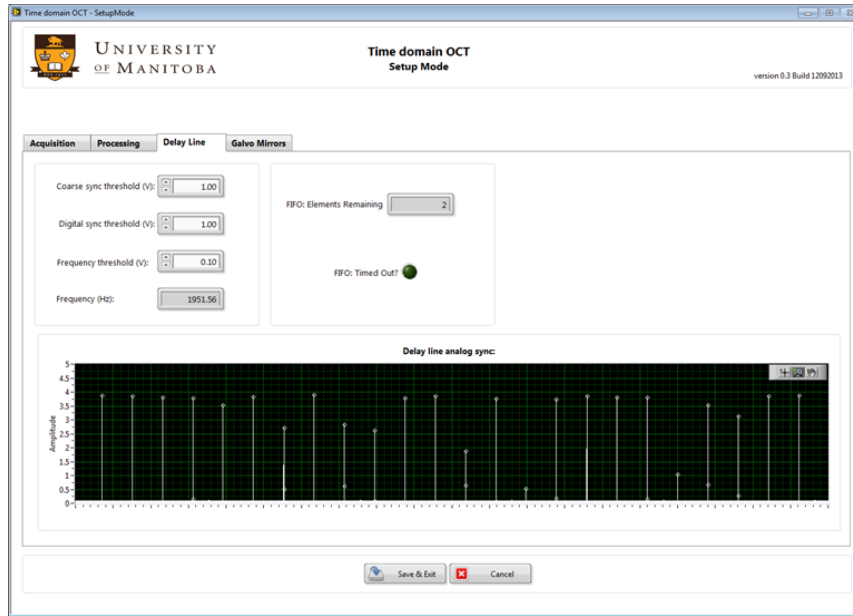


**Figure 4-4 Setup Mode GUI – “Delay Line”**

In the “*Delay Line*” page, the user can see the speed of the optical delay line or A-scan which can be adjusted at the hardware. The optical delay line that we use gives 3.5 mm scanning range. The principle of this delay line was described in 3.3.1.1 [32].



**Figure 4-5 GUI of the Setup mode – “Galvo Mirrors”**

“*Galvo Mirrors*” page is for the user to manually adjust positions of the two mirrors without acquiring data, for example, during an optical setup alignment. After the user finish configuring the system, one has to press the “*Save & Exit*” button to save the configuring file. The file will be used in the “*RunTime mode*”. This step can be skipped in the next time of acquisition if the user wants to use the same system.

#### 4.2.2. Run Mode GUI

A user can start acquiring images by choosing “*Run Mode*” in the “*Welcome Page*”. The “*Run Mode*” is shown in Figure 4-6. In this page, user can fill-in information of the sample that is being imaged in the space on the left side of the GUI. This information will be saved in a text file under the name “*config*” which can be found in the same folder as indicated in the Data Directory.

The interferometric signal of the A-scans will be shown on the screen. The raw signal will be shown in red and the processed signal will be shown in green. Once the user presses the “*Run*” button, the system will start to scan the sample, acquire, and save the data. This process will go on until the whole sample is scanned, or until the user decides to terminate the operation by pressing the “*Run*” button again.

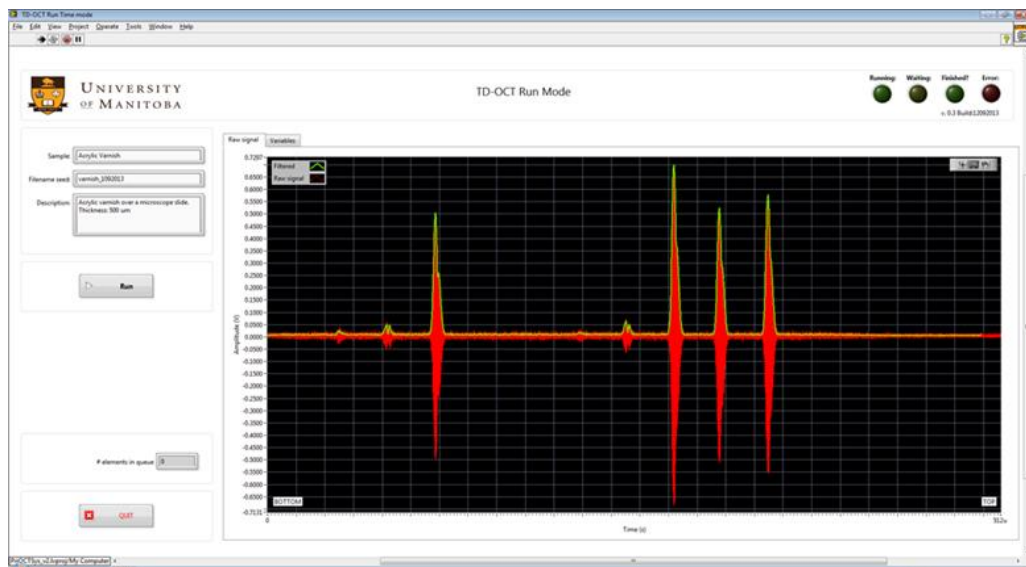
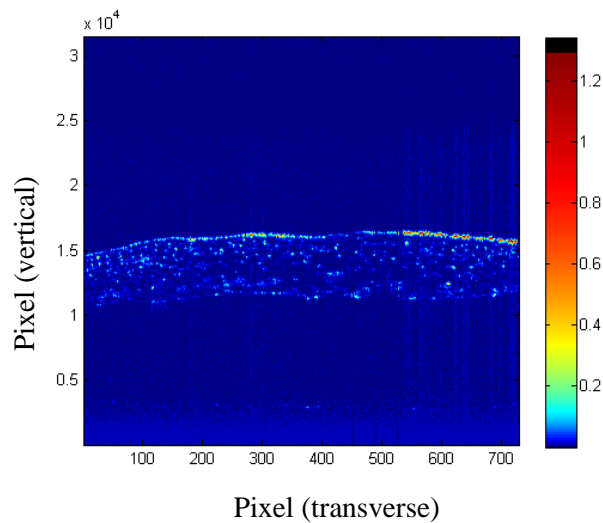


Figure 4-6 Run Mode GUI

### 4.3. Example images acquired using our OCT system

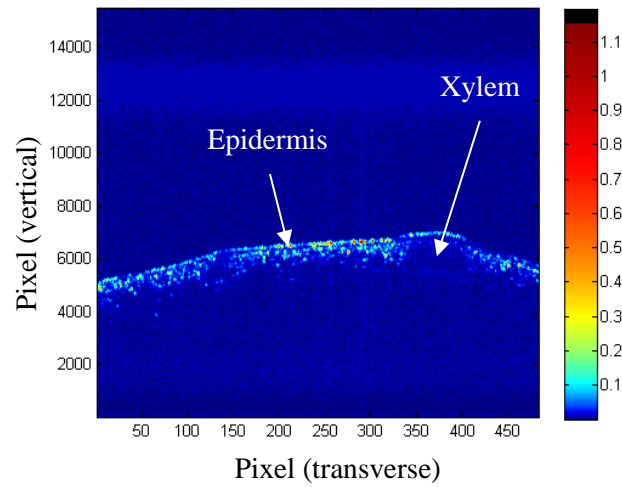
To demonstrate the ability of our TD-OCT to acquire good images, we present several images that were acquired for different purposes.

- Onion skin: Figure 4-7
- Celery stalk: Figure 4-8
- Chicken breast: Figure 4-9
- Fingertip (without gloves and with gloves): Figure 4-10
- Axolotl embryo :Figure 4-11 and Figure 4-12
- Kraft paper: Figure 4-13
- Gaps between two microfibers : Figure 4-14, Figure 4-15, and Figure 4-16
- Tape/tow overlap: Figure 4-17 and Figure 4-18



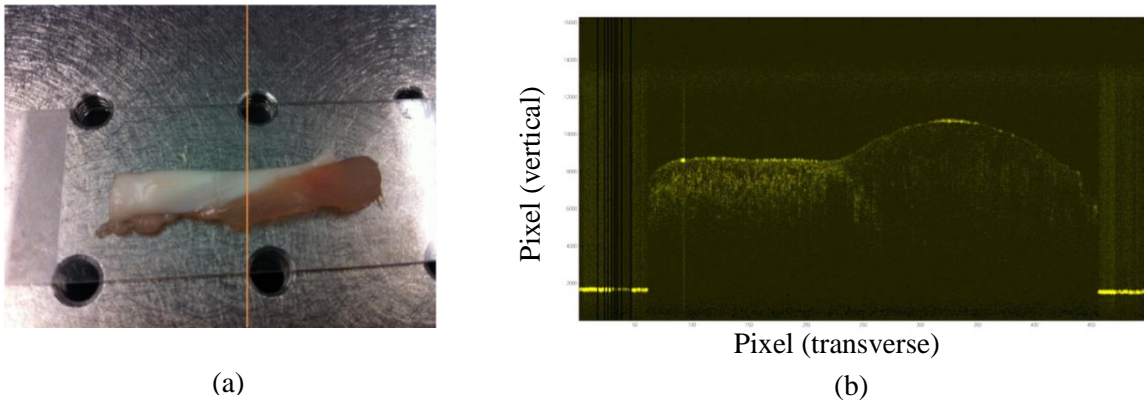
**Figure 4-7 OCT image of an onion skin**

Figure 4-7 shows an OCT image of an onion skin where the structure of cell walls are clearly seen.



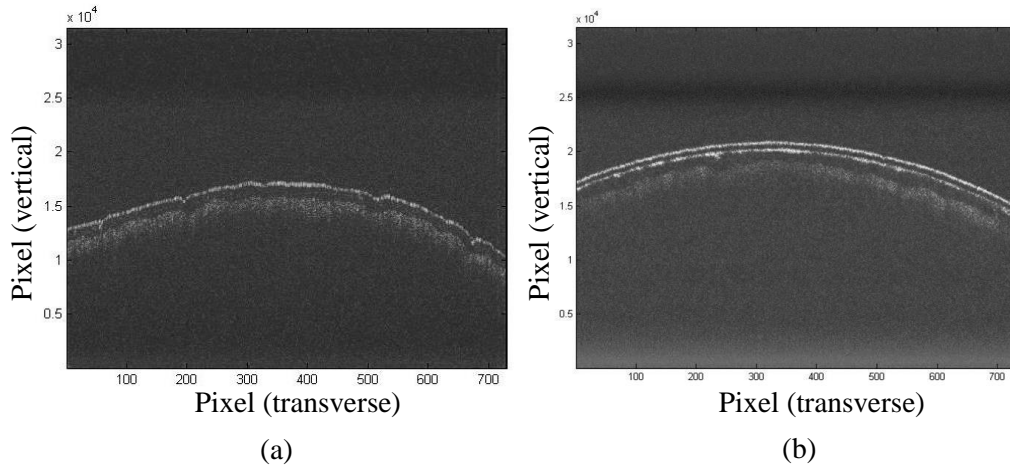
**Figure 4-8 OCT image of a celery stalk**

Figure 4-8 shows an OCT image of a celery stalk where the interior of the epidermis and vascular bundle (xylem) can be seen.



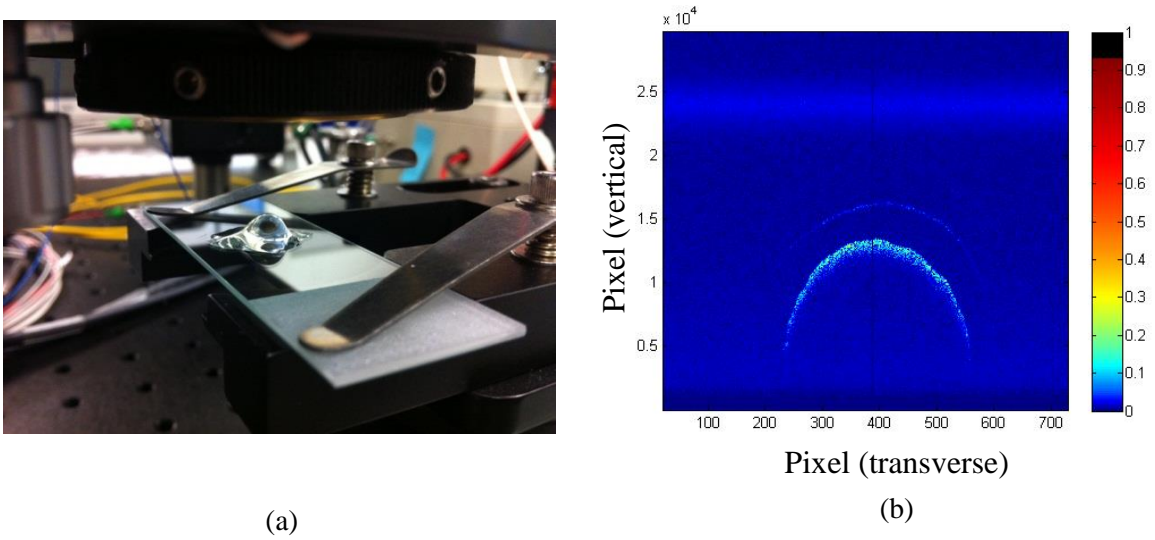
**Figure 4-9 OCT image of a chicken breast (a) actual sample - scan line is indicated in orange (b) OCT image**

Figure 4-9 shows a chicken breast that was used as the sample and its OCT image. The meat part and the cartilage part can be distinguished because they have different subsurface textures.

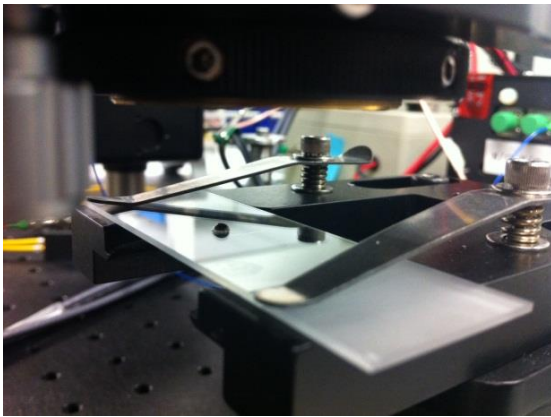


**Figure 4-10 OCT images of a fingertip (a) without gloves (b) with gloves**

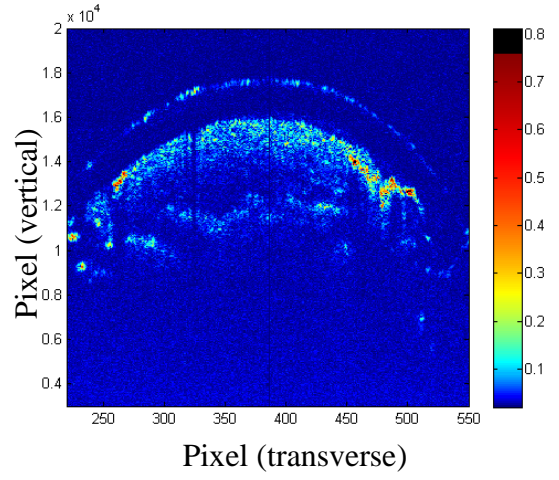
OCT images of a fingertip and the fingertip with gloves are shown in Figure 4-10. The images show that OCT can distinguish the gloves layer from the fingertip.



**Figure 4-11 Axolotl embryo with gel (a) actual sample (b) OCT image**



(a)

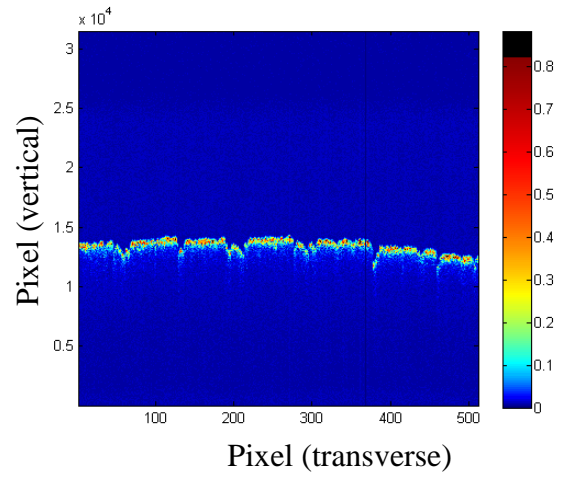


(b)

**Figure 4-12 Axolotl embryo without gel (a) actual sample (b) OCT image**

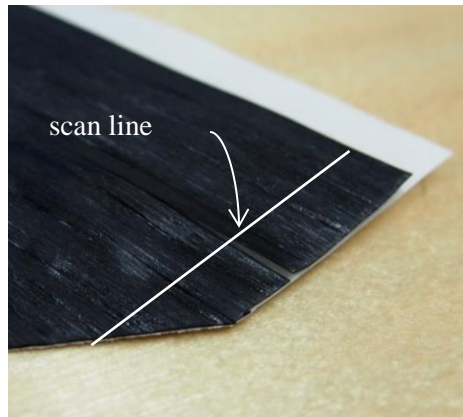


(a)

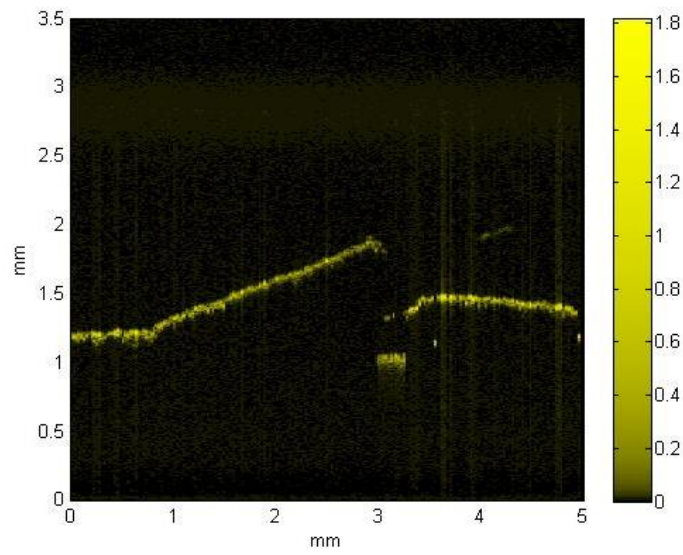


(b)

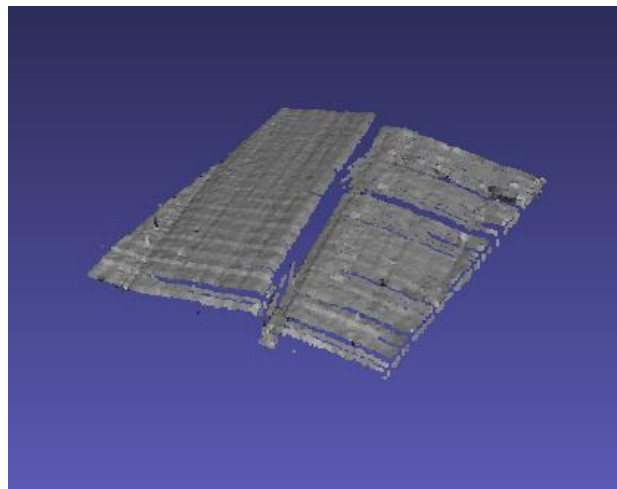
**Figure 4-13 Kraft paper (a) actual sample (b) OCT image**



(a)



(b)

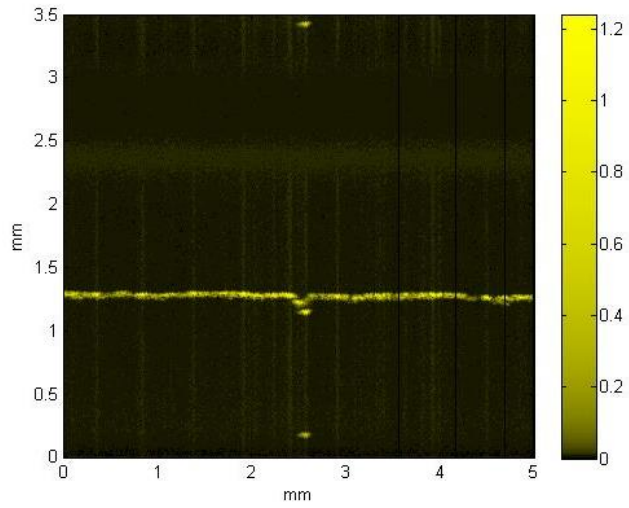


(c)

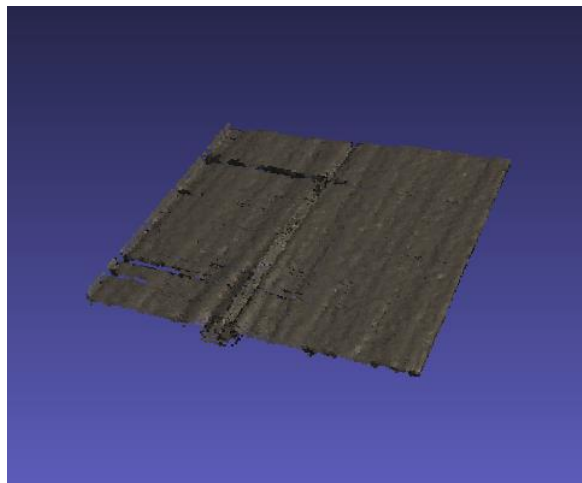
**Figure 4-14 A gap between two microfibers (a) actual sample (b) B-scan OCT image along scan line shown in (a), (c) 3D image**



(a)

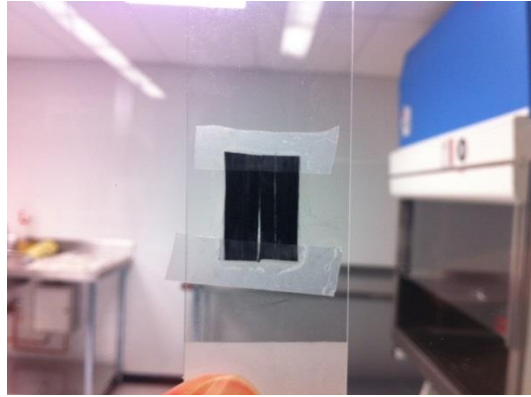


(b)

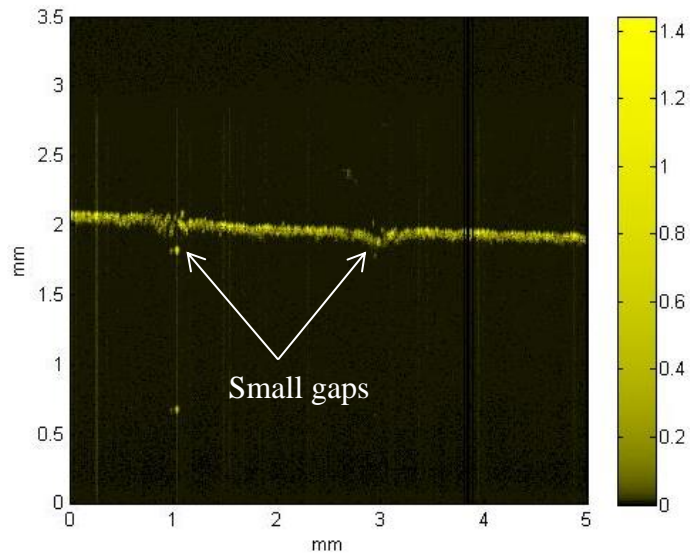


(c)

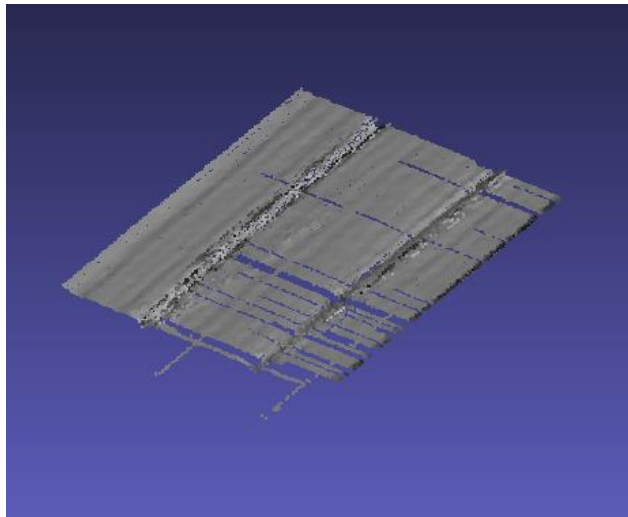
**Figure 4-15 A small gap between two fiber strips (a) actual sample (b) OCT image (c) 3D image**



(a)

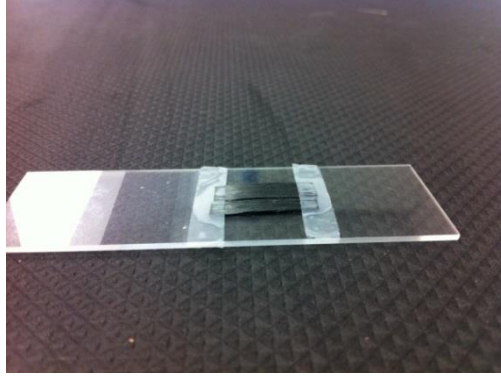


(b)

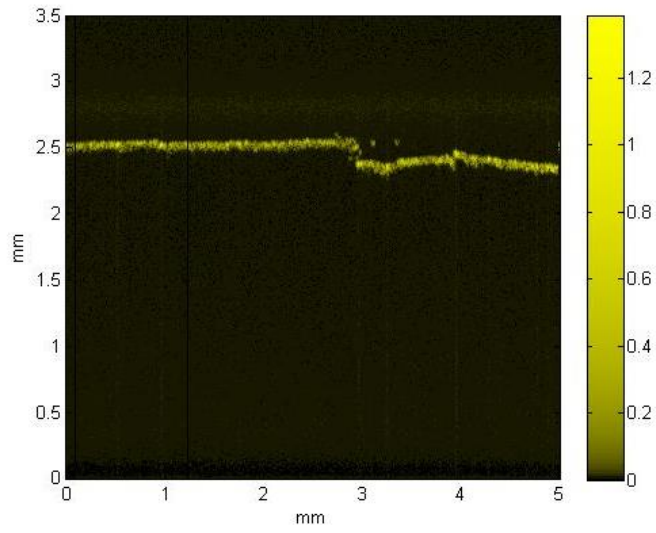


(c)

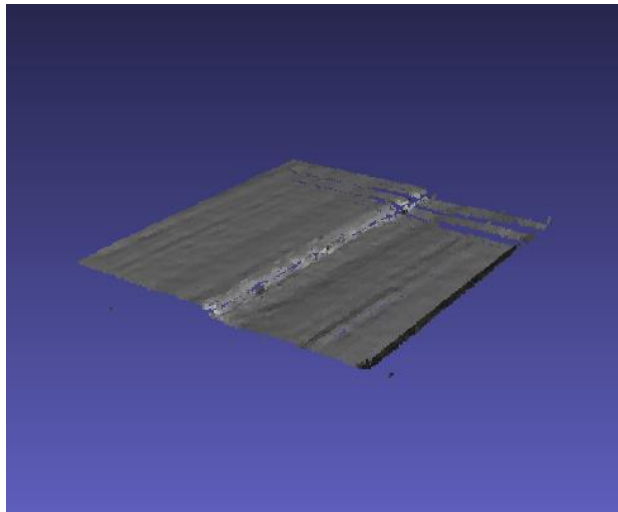
**Figure 4-16 Two small gaps between two fiber strips (a) actual sample (b) OCT image (c) 3D image**



(a)



(b)



(c)

**Figure 4-17** Overlap microfiber strips (a) actual sample (b) OCT image (c) 3D image

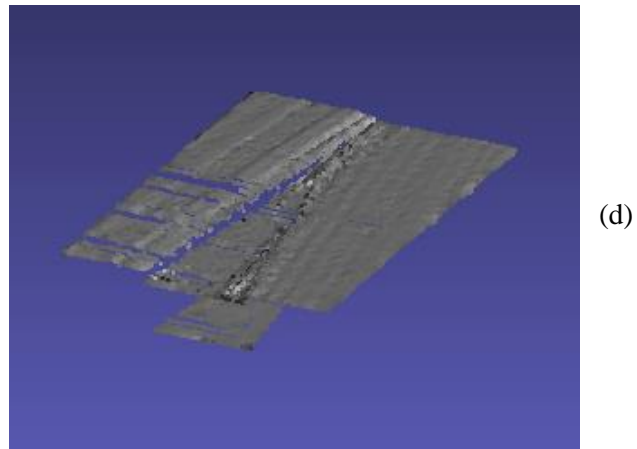
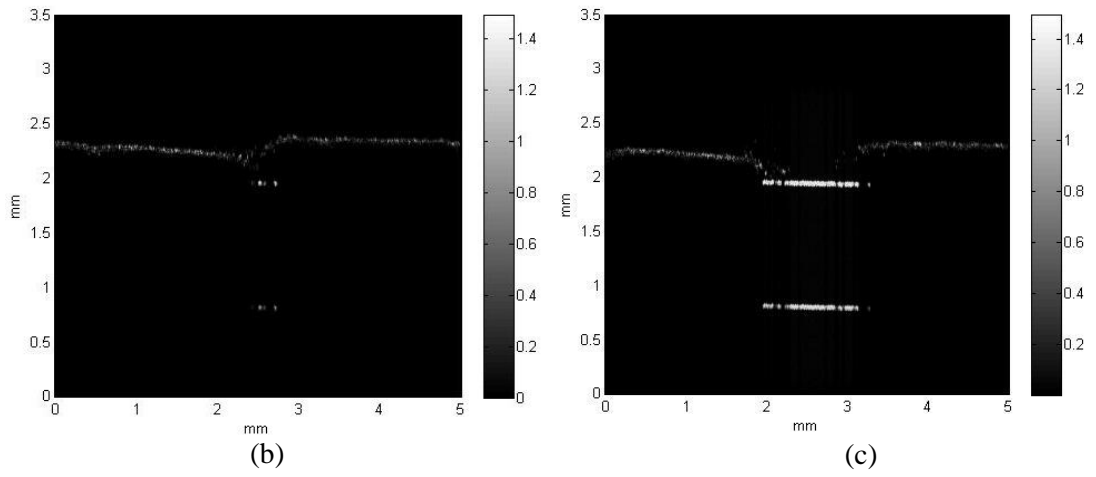
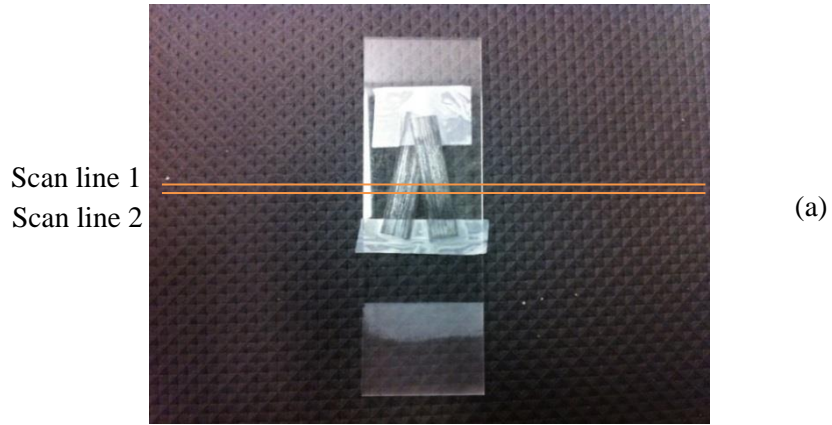


**Figure 4-18** Overlap microfiber strips (a) actual sample (b) OCT image from scan line1  
(c) OCT image from scan line1 (d) 3D image

## **Chapter 5**

### **Extraction of complex scattering potential using Quadrature OCT**

The second part of this thesis is on spectroscopic OCT imaging. Spectroscopic OCT is an extension of conventional OCT where depth-resolved spectroscopic sample properties are analyzed. In this chapter, we describe the theoretical background of spectroscopic OCT and the previous works where spectroscopic OCT was used in finding the complex refractive index of a sample. We also describe our analysis to obtain spectroscopic information using quadrature OCT.

#### **5.1. Introduction**

The main purpose of OCT is to image the subsurface structure of a sample; however, there is more information that could be of interest in a sample e.g., spatial distribution of its light absorption. Functionality of conventional OCT (TD-OCT and SD-OCT) has been extended to obtain spectroscopic information of a sample [3, 4, 5]. This is known as spectroscopic OCT where the spectroscopic information can be obtained using posterior signal processing without changing measurement configurations.

#### **5.2. Overview of spectroscopic OCT (S-OCT)**

Interferometric signals from an OCT, in addition to information about the structure of samples, also contain spectroscopic information. The backscattered light from a sample is modulated, in terms of its amplitude and frequency, as it travels inside the sample. These modulations come from interactions of the wave with the sample. For example, some parts of the spectrum of broadband light might be absorbed by molecules (or chromophores) inside the sample. Spectral information of a time dependent function can be obtained by applying a Fourier transform to the function; however, the transformed signal is global and delocalized in space. Therefore, localized spectroscopic information cannot be obtained by applying the Fourier transform to the OCT

signal. Depth-resolved spectral information can be obtained from the instantaneous frequency content of the OCT signal. The instantaneous frequency of a signal can be calculated using time-frequency (TF) analysis applied for signals measured from both TD-OCT [4] and SD-OCT [5].

Two classes of time-frequency analysis algorithms are commonly used in spectroscopic imaging. The first approach is called the *atomic decompositions* and the second approach is called the *energy distributions*. The basic idea of atomic decompositions is to linearly decompose a signal into “atoms” by using a “sliding window”. The technique is known as a windowed-Fourier transform or a short-time Fourier transform (STFT). The Fourier transform is applied to the signal inside the window to obtain its local spectrum components; therefore, the STFT is a function of time and frequency. The second class of time-frequency analysis is Cohen’s class which is based on calculating the distribution of signal energy over time and frequency. One of the most important members of Cohen’s class is called Wigner-Ville distribution. Mathematical explanations of these two classes of TF analysis algorithms are explained in APPENDIX A.

### **5.3. Previous work of using OCT for local separation of scattering and absorption effects in a sample**

We begin the discussing on the previous work on separating scattering and absorption effects in a sample with the analysis from Xu *et al.* in 2004 [8]. They proposed a method where both time-frequency analysis and a least-square fitting algorithm are utilized to separate the absorption and scattering profiles of testing tissue phantoms. Typically, the absorption and scattering coefficients are dependent on both wavelength and depth:  $\mu_a(\lambda, z)$  and  $\mu_s(\lambda, z)$ . In their analysis, these coefficients are rewritten in the form of multiplication of two functions,  $\mu_a(\lambda, z) = \varepsilon_a(\lambda)f_a(z)$  and  $\mu_s(\lambda, z) = \varepsilon_s(\lambda)f_s(z)$ .  $\varepsilon_a(\lambda)$  and  $\varepsilon_s(\lambda)$  are absorption and scatter concentration per unit length and  $f_a(z)$  and  $f_s(z)$  are absorber and scatterer concentrations at a particular depth. By using time-frequency analysis and least-squares fitting algorithm, they were able to estimate the depth-resolved spectral modification based on scattering and absorption coefficients separately.

Functional S-OCT to determine localized tissue oxygenation has been studied in [38, 39]. The extinction of light wave comes from the absorption property by hemoglobin and the scattering property of red blood cells. The oxygen saturation of  $SO_2$  can be optically determined by the difference in light absorption between oxygenated hemoglobin ( $Hb(HbO_2)$ ) and deoxygenated hemoglobin (Hb) which will appear in the spectrum of the OCT signal. In [38, 39], the absorption spectra were calculated by applying STFT analysis to the OCT signal.

In 2010, Robels and Wax [9] presented an analytic method together with time-frequency analysis to retrieve the real and imaginary parts of the refractive index from low-coherence interferometric signals. Like typical spectroscopic OCT, the technique is based on the time-frequency analysis. In their method, the refractive index  $n(\omega)$  was expanded as  $n(\omega) = n(\omega_0) + \Delta n(\omega)$  by Taylor series expansion. Although light dispersion would degrade the quality of the axial resolution, it contains information about wavelength-dependent changes in the real part of the refractive index, from which the imaginary part of the refractive index can be retrieved using Kramers-Kronig relations. Therefore, the scattering and absorption coefficients of the sample can be quantified.

In 2013, Jaedicke *et al.* proposed a new method to analyze the scattering property of a sample using multispectral imaging and signal processing [40]. The depth-resolved spectroscopic information was analyzed using the dual-window method proposed by Robels *et al.* [41]. Then the spectroscopic information is processed by different feature reductions to calculate spectroscopic metrics to be displayed using a color map. These results demonstrated that the proposed method resulted in high performance clustering of areas in the sample with different scattering properties.

## 5.4. Our work to obtain the complex scattering profile of a sample using quadrature OCT

In the previous works, the procedure to obtain the spectroscopic information of the sample involves the time-frequency analysis and Kramers-Kronig relations. These techniques mainly use OCT based on low coherence interferometry and require time-frequency analysis. The problem is that these techniques are not applicable to a swept-source OCT which is the fastest OCT imaging method available. Also the use of time-frequency analysis results in reduced spatial resolution due to windowing effects. We propose a different approach to obtain the information that does not suffer from such problems. In our analysis, the complex scattering potential, or the complex susceptibility, is obtained through the quadrature OCT.

We resume discussion from the swept source OCT explained in section 2.5 in Chapter 2. We emphasize the relationship between the scattering potential and the complex refractive index of the sample. Afterward, we discuss how the complex scattering potential is obtained by using a swept-source quadrature OCT. Finally, we introduce a new interpretation of the space-domain signal; the 2<sup>nd</sup> derivative of the scattering potential of the sample.

### 5.4.1. Relationship between the scattering potential and the complex refractive index of a sample

Resuming our discussion of the swept-source OCT in Chapter 2, the scattering potential of the object is expressed as [28],

$$P(\mathbf{r}, k) = -k^2(n^2(\mathbf{r}, k) - 1), \tag{5.1}$$

where  $n^2(\mathbf{r}, k)$  is the complex refractive index given by

$$n(\mathbf{r}, k) = n_s(\mathbf{r}, k) + jn_a(\mathbf{r}, k).$$

(5.2)

The real part of the refractive index,  $n_s$ , corresponds to scattering effects, whereas the imaginary part,  $n_a$ , corresponds to absorption effects in the sample.

Expanding Eq. (5.1), we obtain,

$$P(\mathbf{r}, k) = -k^2 \{ (n_s^2(\mathbf{r}, k) - n_a^2(\mathbf{r}, k) - 1) + (2jn_s(\mathbf{r}, k)n_a(\mathbf{r}, k)) \}.$$

(5.3)

As typical in OCT, scattering potential  $P(\mathbf{r}, k)$  is assumed constant in the  $x$  and  $y$  directions and the dispersion in the sample is ignored, Eq. (5.3) becomes

$$P(z) = -k^2 \{ (n_s^2(z) - n_a^2(z) - 1) + (2jn_s(z)n_a(z)) \}.$$

(5.4)

The imaginary part of the complex refractive index,  $n_a(z)$ , in tissue is very small compared to  $n_s(z)$ , so we can neglect  $n_a^2(z)$ . The complex scattering potential can be expressed as

$$P(z) = \text{Re}\{P(z)\} + j\text{Im}\{P(z)\},$$

(5.5)

where

$$\text{Re}\{P(z)\} = -k^2(n_s^2(z) - 1)$$

(5.6)

and

$$\text{Im}\{P(z)\} = -k^2(2n_a(z)n_s(z)).$$

(5.7)

### 5.4.2. Obtaining the complex scattering potential using a swept-source quadrature OCT

The interference signal obtained from a conventional swept-source OCT

In conventional OCT, the measured data is the real part of the interference signal between the two wavefields; one from reference and one from sample arm. Assuming that the wavefields are plane waves, the reference and sample waves can be described as

$$E_r(z_{ref}, k) = A^i \exp(-jkz_{ref}) \quad (5.8)$$

and

$$E_s(z_{sample}, k) = \frac{A^i W}{4\pi(z_{ref} + \Delta z)} \exp(-jk(z_{ref} + \Delta z)) \tilde{P}(2k), \quad (5.9)$$

where  $z_{sample} = z_{ref} + \Delta z$  and  $\Delta z$  is the path length mismatch between the reference and sample arms. In general, the intensity of the interference signal between two monochromatic wavefields can be described as in Eq. (5.10).

$$\begin{aligned} I_{OCT}(z, k) &= |E_r(z_{ref}, k) + E_s(z_{sample}, k)|^2 \\ &= |A^i|^2 + \left| \frac{A^i W}{4\pi z_{ref}} \tilde{P}(2k) \right|^2 \\ &\quad + 2\text{Re} \left\{ A^i \exp(jkz_{ref}) \frac{A^i W}{4\pi(z_{ref} + \Delta z)} \exp(-jk(z_{ref} + \Delta z)) \tilde{P}(2k) \right\}. \end{aligned} \quad (5.10)$$

The interferometric portion of the intensity signal is given by

$$I(z, k) = 2|A^i|^2 \frac{W}{4\pi(z_{ref} + \Delta z)} \text{Re}\{\exp(-jk\Delta z)\tilde{P}(2k)\} \quad (5.11)$$

which has information only on the real part of the scattering potential.

Quadrature swept-source OCT [10]

The diagram of the quadrature OCT using a  $3 \times 3$  fiber coupler is illustrated in Figure 5-1.

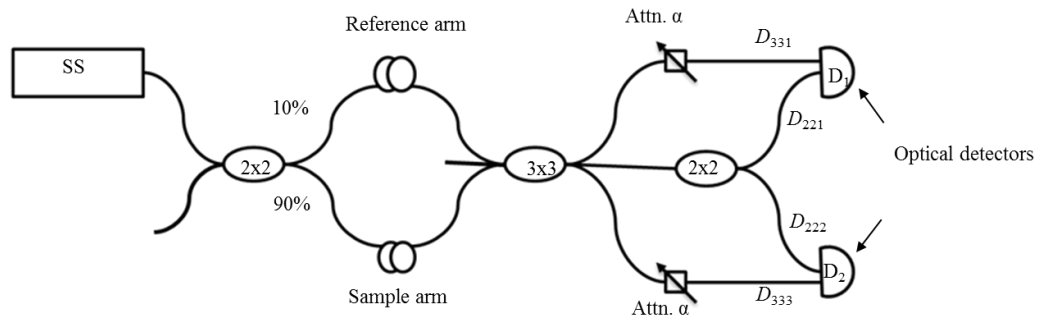


**Figure 5-1 A diagram of A Mach-Zehnder interferometer using  $3 \times 3$  fiber coupler to acquire a complex interferometric signal [10]**

Two interferometric signal intensities  $D_1$  and  $D_2$  are calculated from the outputs of the two differential detectors.

$$D_1(\phi) = \alpha D_{33_1}(\phi) - D_{22_1}(\phi)$$

$$D_2(\phi) = \alpha D_{33_3}(\phi) - D_{22_2}(\phi)$$

(5.12)

where  $\alpha$  represents attenuation and  $\phi$  is the phase shift between the sample and reference arms.

The real ( $I_{real}$ ) and imaginary ( $I_{img}$ ) parts of the OCT signal are calculated from the power of interferometric signals  $D_1$  and  $D_2$  using the following equations.

$$I_{real}(\phi) = D_1(\phi), \quad I_{img}(\phi) = \frac{D_1(\phi) \cos(\Delta\phi) - D_2(\phi)}{\sin(\Delta\phi)} \quad (5.13)$$

where,  $\Delta\phi$  is the phase difference between the interferometric signals  $D_1$  and  $D_2$ .

In this analysis, the power splitting ratios of the fiber couplers is assumed to be independent on the wavelength. The complex signal is obtained by putting the real and imaginary signals together as  $I_{real} + jI_{img}$ , and the OCT signal measured from the quadrature SS-OCT system can be described as

$$I_{quadrature}(k) = 2|A^i|^2 \frac{W}{4\pi(z_{ref} + \Delta z)} \left( \exp(-jk\Delta z) \tilde{P}(2k) \right) \quad (5.14)$$

The inverse Fourier transform of  $\{\exp(-jk\Delta z) \tilde{P}(2k)\}$  will be shifted by the amount of  $\Delta z$ . The difference between Eq.(5.11) and Eq. (5.14) is that quadrature SS-OCT can measure, not only the real part, but also the imaginary part of the scattering potential of a sample.

### 5.4.3. New interpretation of SS-OCT images

Applying an inverse Fourier transform to the measured data in Eq. (5.14) and presenting the space-domain image in absolute value is the common way of displaying OCT images.

The scattering potential in Eq. (5.4) can be written as

$$P(z) = -k^2(n^2(z) - 1) = -k^2P_1(z), \quad (5.15)$$

where  $P_1(z) = n^2(z) - 1$ .

In the spectral domain, the frequency variable  $-k^2$  represents the 2<sup>nd</sup> derivative of  $P_1(z)$  or [42].

This implies that the structure of the sample shown in the OCT images represents  $\frac{\partial^2 P_1(z)}{\partial z^2}$ . By

substituting  $n(z) = n_s(z) + jn_a(z)$  into  $P_1(z) = n^2(z) - 1$ , we obtain

$$P_1(z) = (n_s^2(z) - n_a^2(z) - 1) + 2jn_s(z)n_a(z)$$

The 1<sup>st</sup> derivative of  $P_1(z)$  is given by

$$\frac{\partial P_1(z)}{\partial z} = \left( 2n_s(z) \frac{\partial n_s(z)}{\partial z} - 2n_a(z) \frac{\partial n_a(z)}{\partial z} \right) + 2j \left( n_s(z) \frac{\partial n_a(z)}{\partial z} + n_a(z) \frac{\partial n_s(z)}{\partial z} \right) \quad (5.16)$$

and the 2<sup>nd</sup> derivative is given by

$$\frac{\partial^2 P_1(z)}{\partial z^2} = \frac{\partial}{\partial z} \left( 2n_s(z) \frac{\partial n_s(z)}{\partial z} - 2n_a(z) \frac{\partial n_a(z)}{\partial z} \right) + 2j \frac{\partial}{\partial z} \left( n_s(z) \frac{\partial n_a(z)}{\partial z} + n_a(z) \frac{\partial n_s(z)}{\partial z} \right). \quad (5.17)$$

Therefore, in SS-OCT we are observing the second derivative of the scattering potential where in both real and imaginary parts are the effects of scattering and absorption that are highly intertwined. In image processing, the 2<sup>nd</sup> derivative operator is one of the edge detection methods [43].

## 5.5. Experimental setup and results

### 5.5.1. Swept Source quadrature OCT

We obtained quadrature OCT images using a quadrature swept source OCT system implemented at the Institute for Microstructural Sciences, National Research Council Canada [10]. The system configuration is based on 3×3 Mach-Zehnder interferometer. The central wavelength of the swept source (HSL 2000, Santec) is 1320 nm with a full scan wavelength of 110 nm. The coherence length of the swept source is 10.8 mm and the operating frequency is 20 kHz, which is equivalent

to 3200 vertical pixels. A galvanometer is used to transversely scan the beam over the sample with 900 transverse pixels. The transverse resolution of the system is  $27 \mu\text{m}$ . The intensities of the two optical interference signals are measured by two differential photodetectors (2117-FC, NewFocus).

The example of an A-scan is shown in Figure 5-2. Figure 5-2 (a) shows the two interference signal intensities obtained from the detectors, whereas, Figure 5-2 (b) shows the absolute values of the A-scan in space-domain after an inverse Fourier transform is applied.

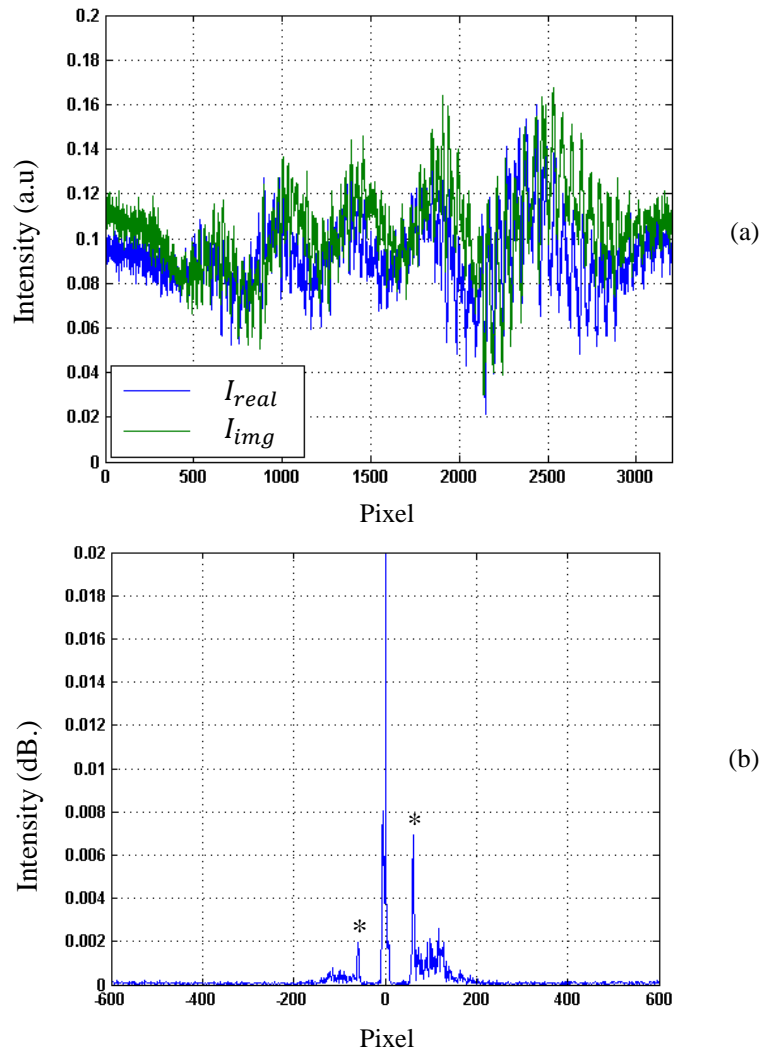


**Figure 5-2 An A-scan signal (a) interferometric signals from the measurements (b) A-scan**

## 5.5.2. Examples of images acquired by our quadrature OCT system

### 5.5.2.1. Sample 1: A fingertip without gloves

Figure 5-3 (a) shows the full range OCT image (no integration) of a fingertip. Figure 5-3 (b) shows the Region-Of-Interest (ROI).

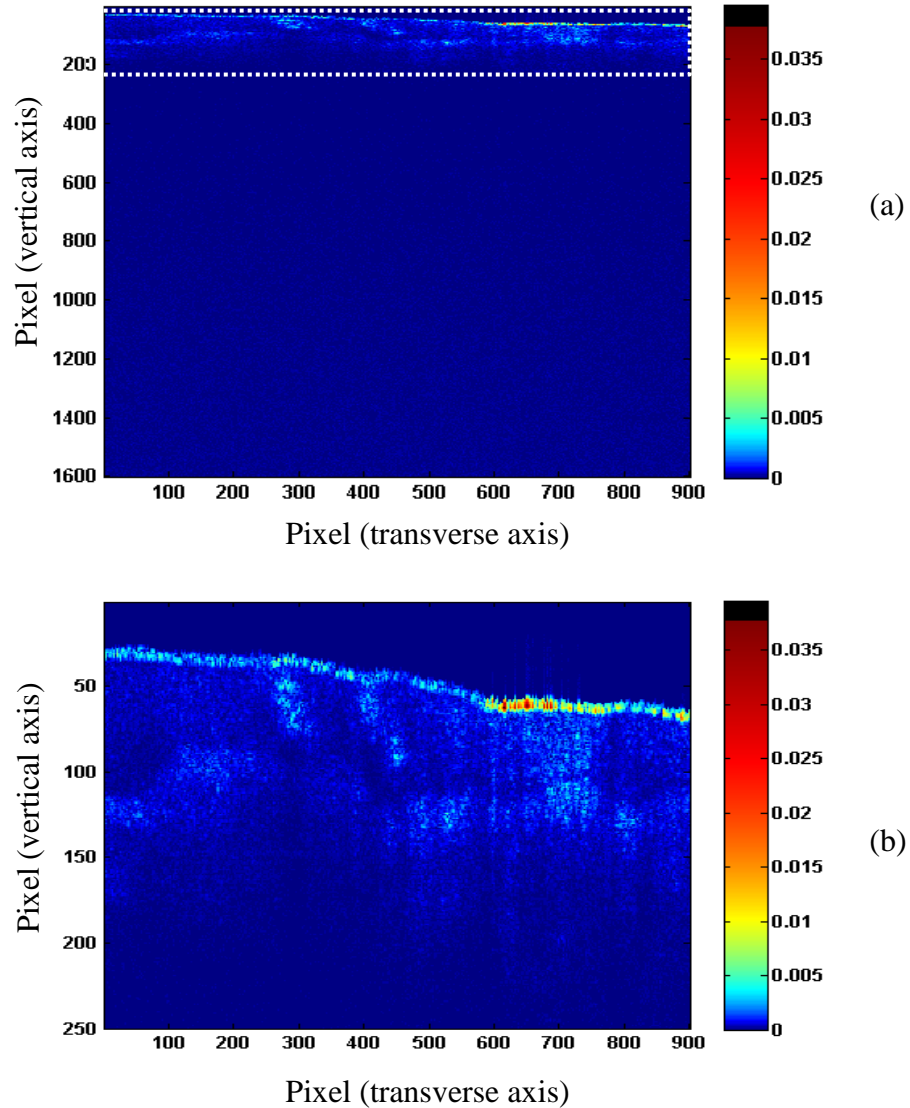


Figure 5-3 OCT images of a fingertip (a) full range image  
(b) ROI indicated by the white dashed box in (a)

Figure 5-4 (a) shows the real part of  $\left\{\frac{\partial^2 P_1(z)}{\partial z^2}\right\}$  of a fingertip.

Figure 5-4 (b) shows the imaginary part of  $\left\{\frac{\partial^2 P_1(z)}{\partial z^2}\right\}$  of a fingertip.

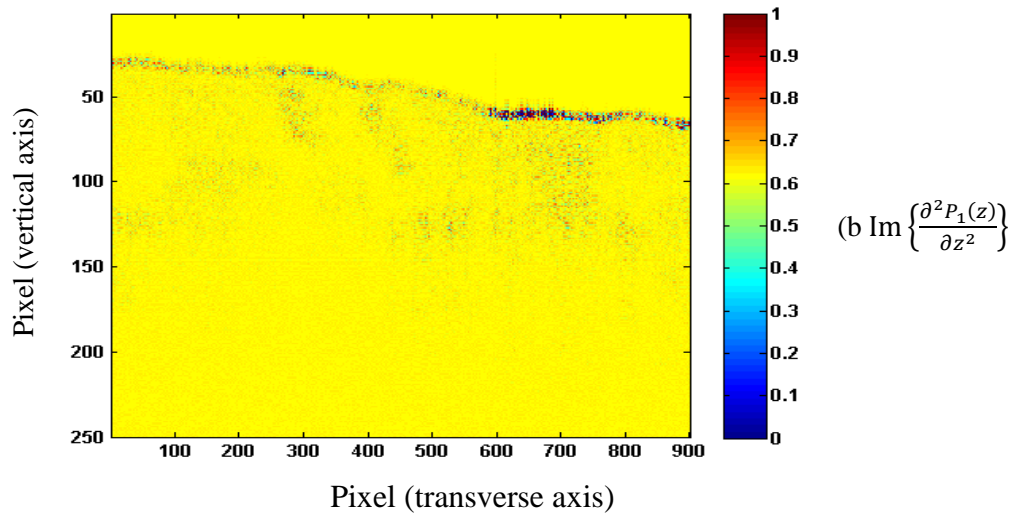
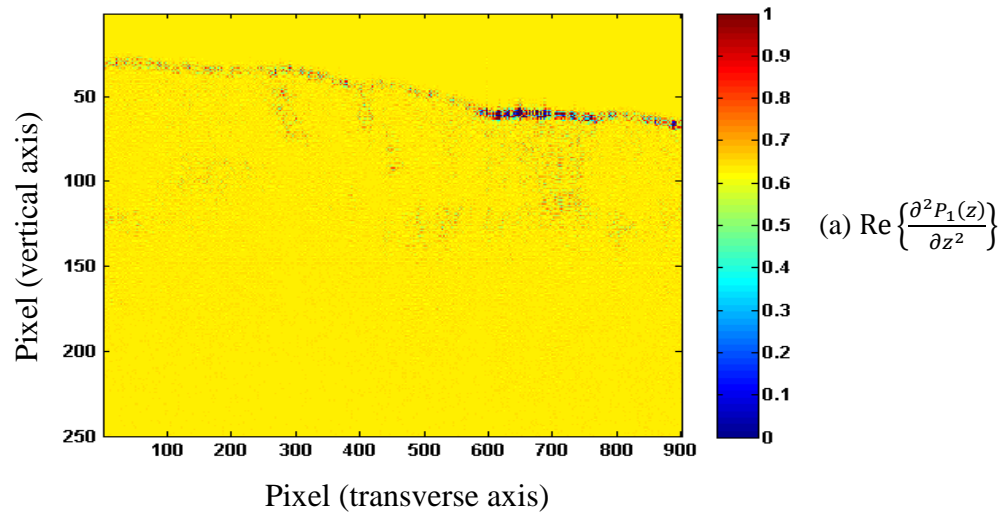


Figure 5-4 Images representing the 2<sup>nd</sup> derivative of the scattering potential profile of a fingertip (a) real part and (b) imaginary part

### 5.5.2.2. Sample 2: A fingertip with gloves

Figure 5-5 (a) shows the full range OCT image of a fingertip with gloves. Figure 5-5 (b) shows the Region-Of-Interest (ROI)

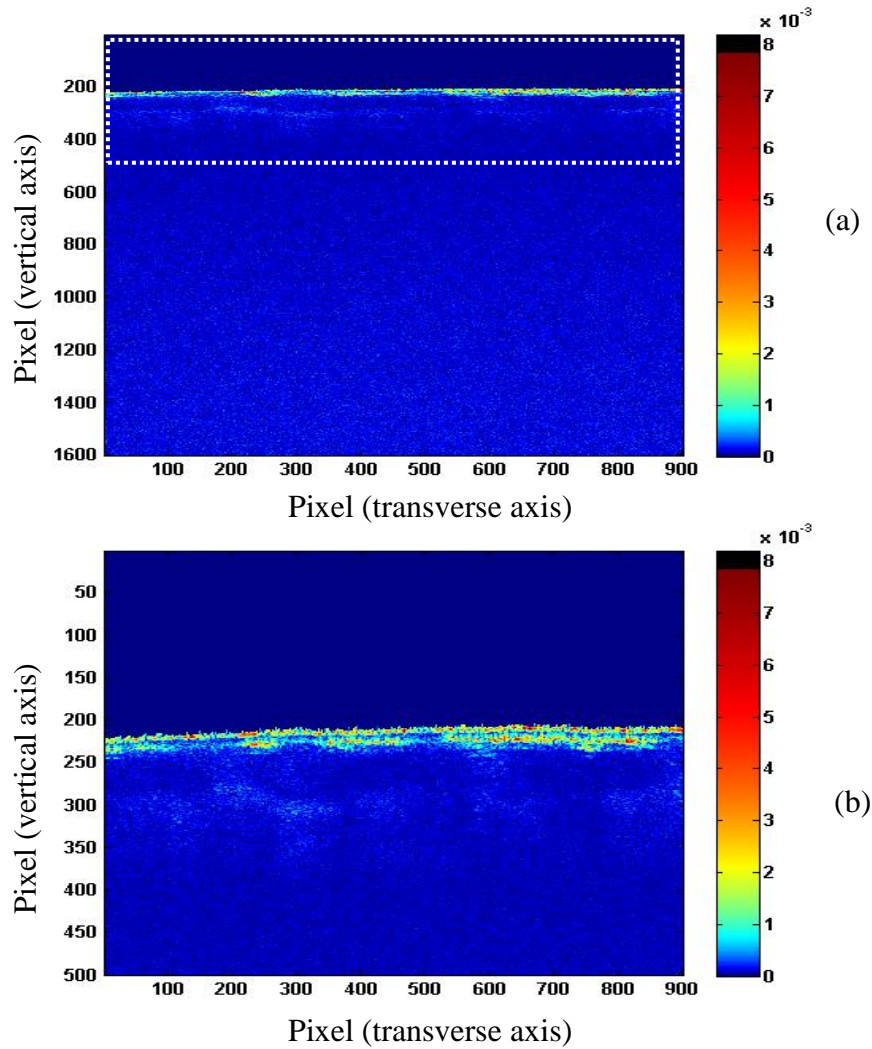
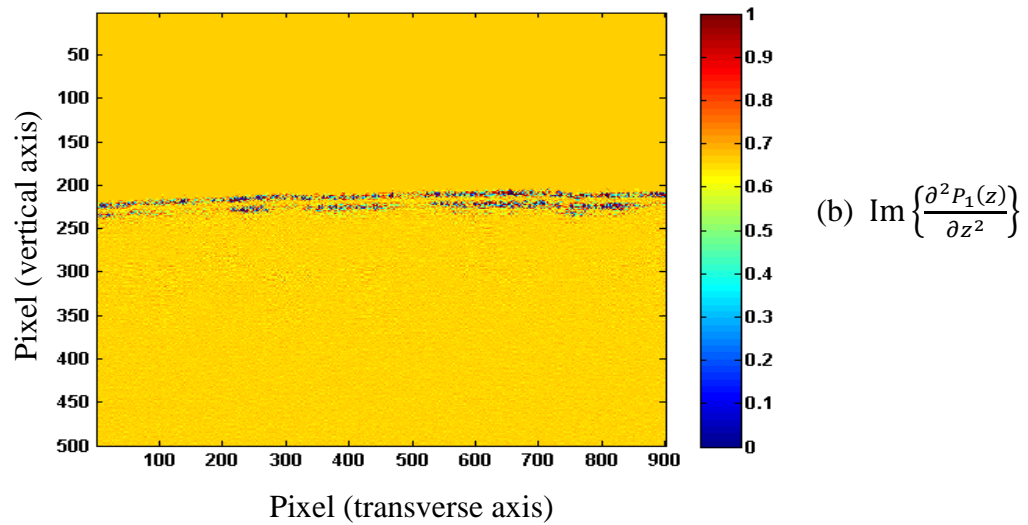
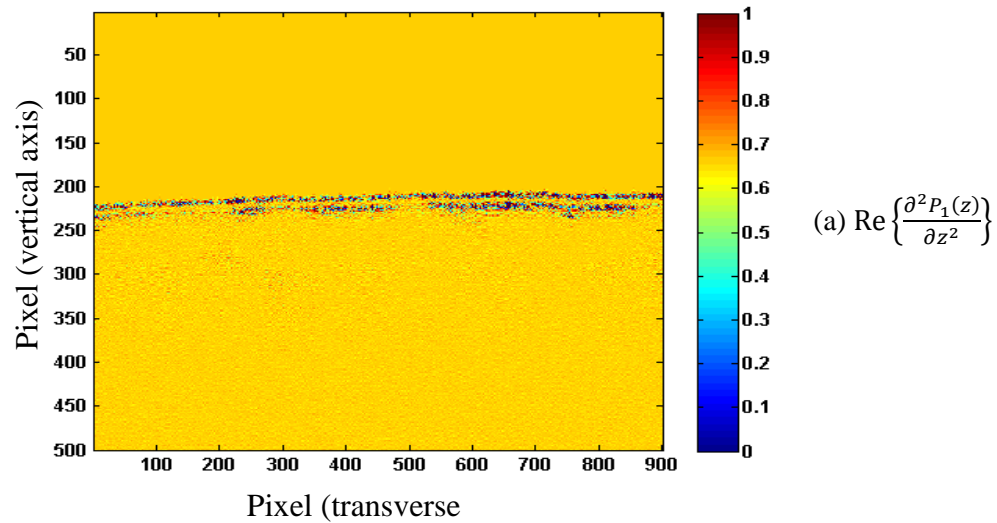


Figure 5-5 OCT images of a fingertip with gloves. (a) full range image and (b) ROI indicated by the white dashed box in (a)

Figure 5-6 (a) shows the imaginary part of  $\left\{\frac{\partial^2 P_1(z)}{\partial z^2}\right\}$  of a fingertip with gloves.

Figure 5-6 (b) shows the imaginary part of  $\left\{\frac{\partial^2 P_1(z)}{\partial z^2}\right\}$  of a fingertip with gloves.



**Figure 5-6 Images representing the 2<sup>nd</sup> derivative of the scattering potential profile of a fingertip with gloves(a) real part and (b) imaginary part**

### 5.5.2.3. Sample 3: An axolotl embryo

Figure 5-7 (a) shows the full range OCT image (no integration) of an axolotl embryo

Figure 5-7 (b) shows the Region-Of-Interest (ROI)

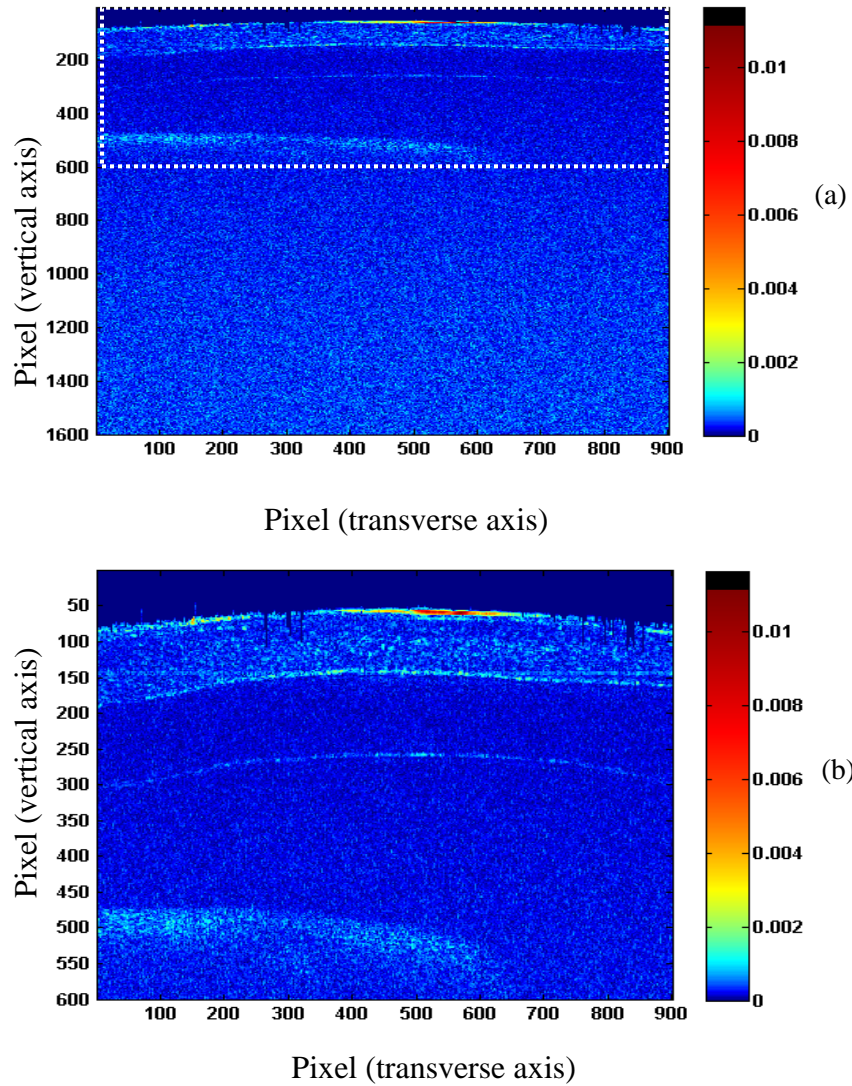
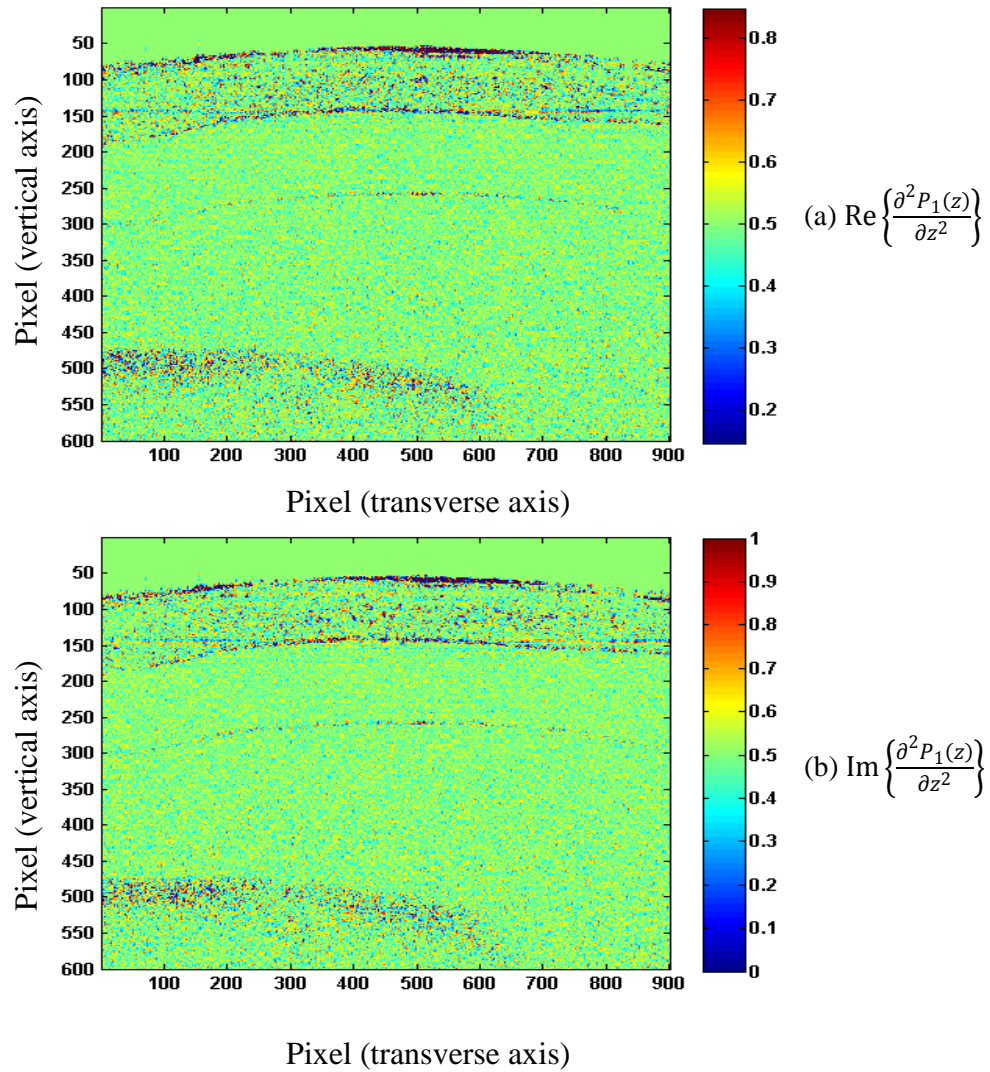


Figure 5-7 OCT images of an axolotl embryo. (a) full range image and (b) ROI indicated by the white dashed box in (a)

Figure 5-8 (a) shows the real part of  $\left\{\frac{\partial^2 P_1(z)}{\partial z^2}\right\}$  of an axolotl embryo.

Figure 5-8 (b) shows the imaginary part of  $\left\{\frac{\partial^2 P_1(z)}{\partial z^2}\right\}$  of an axolotl embryo.



**Figure 5-8 Images representing the 2<sup>nd</sup> derivative of the scattering potential profile of an axolotl embryo (a) real part and (b) imaginary part**

#### 5.5.2.4. Sample 4: Clear adhesive tape

Figure 5-9 (a) shows the full range OCT image (no integration) of a clear adhesive tape

Figure 5-9 (b) shows the region-of-interest (ROI)

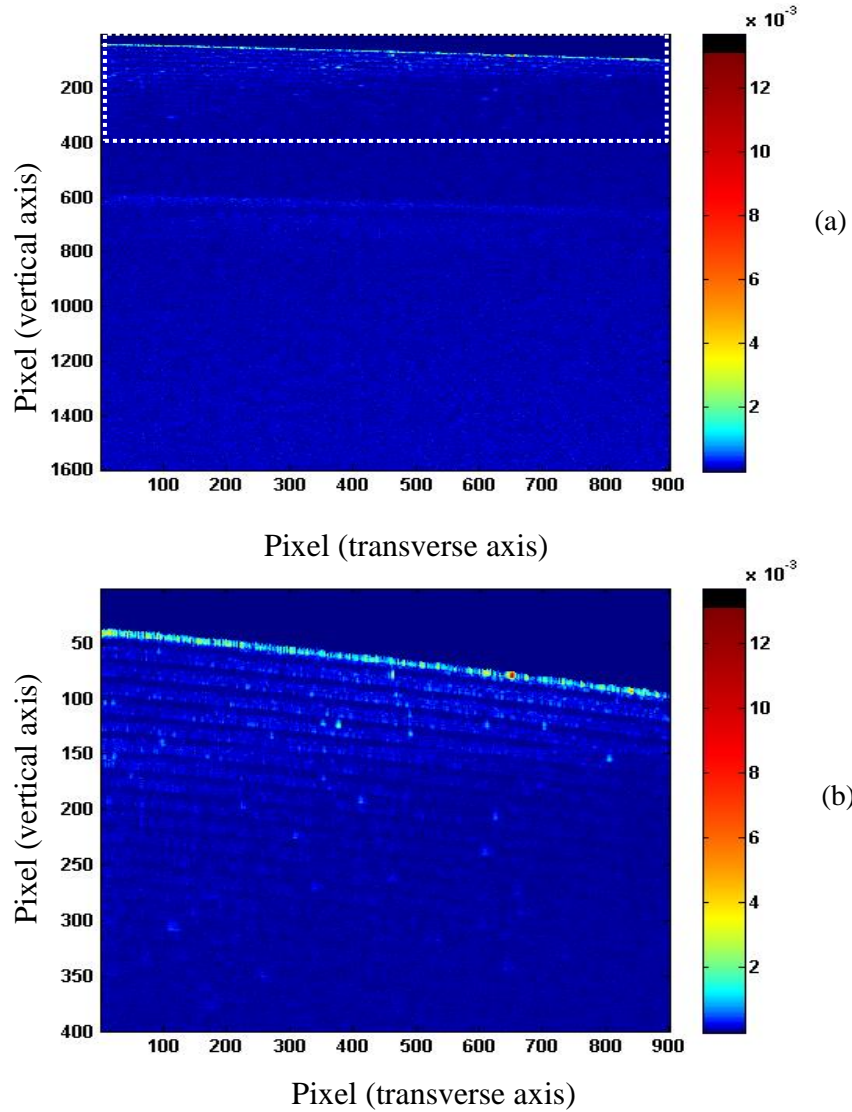
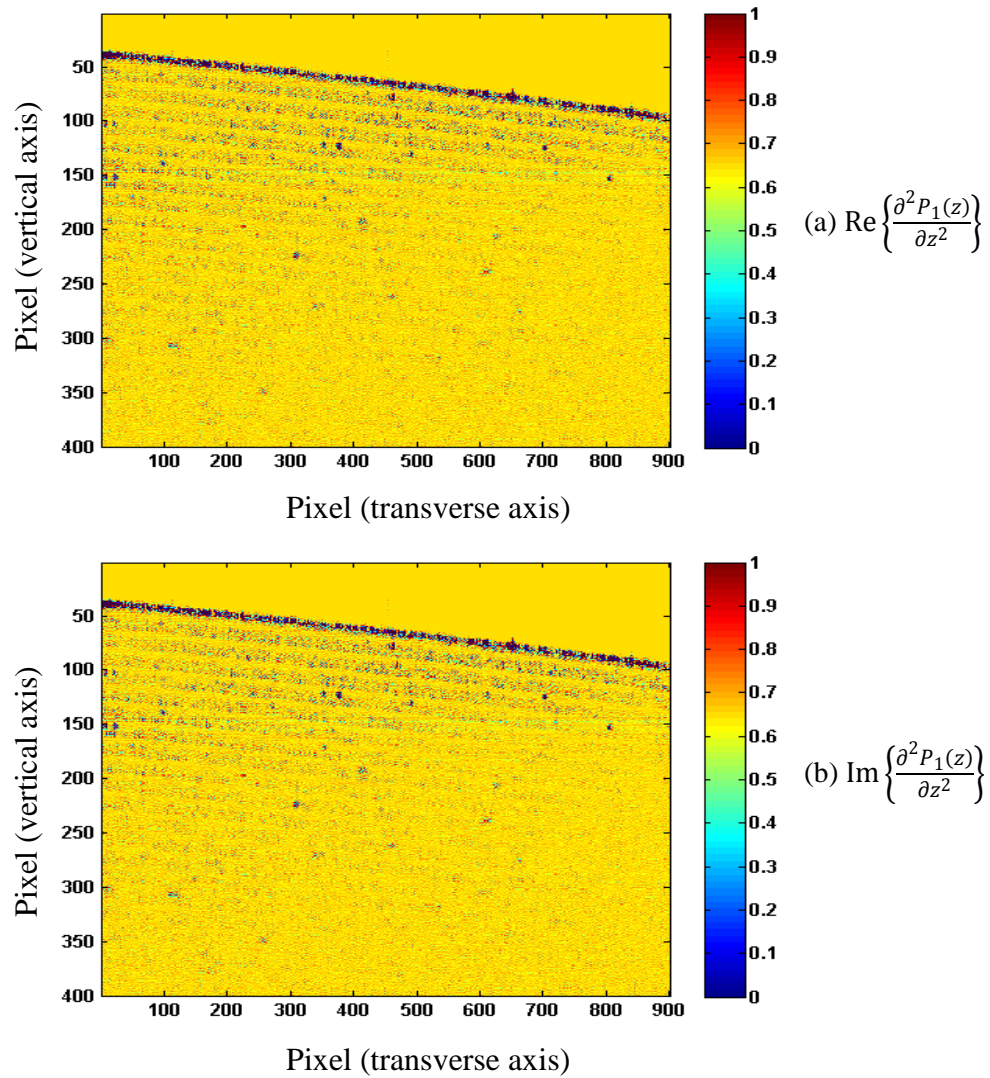


Figure 5-9 OCT images of clear adhesive tape. (a) full range image and (b) ROI indicated by the white dashed box in (a)

Figure 5-10 (a) shows the real part of  $\left\{\frac{\partial^2 P_1(z)}{\partial z^2}\right\}$  of a clear adhesive tape.

Figure 5-10 (b) shows the imaginary part of  $\left\{\frac{\partial^2 P_1(z)}{\partial z^2}\right\}$  of a clear adhesive tape.



**Figure 5-10 Images representing the 2<sup>nd</sup> derivative of the scattering potential profile of clear adhesive tape(a) real part and (b)imaginary part**

## Chapter 6

### Obtaining scattering and absorption profiles from the complex scattering potential

#### 6.1. Method to obtain scattering and absorption profiles from the complex scattering potential

Our new method to obtain scattering and absorption profiles is summarized as follows.

- 1) The measured spectral-domain data is integrated in the spectral domain to obtain  $P_1(z)$
- 2) Profiles of  $n_s$  and  $n_a$  are separated
- 3) 2<sup>nd</sup> derivative is obtained to display resulting images

##### 6.1.1. Integrating the 2<sup>nd</sup> derivative of the scattering potential

Indefinite integration can be carried out in the measured space-domain (by Riemann sum or rectangle method [44]) or in spectral domain [42, 45, 46]. We decided to use spectral methods because the data obtained from the swept source OCT is already represented in spectral domain. Also spectral domain integration allows two consecutive integrations in one step.

From Eq. (5.14) and Eq. (5.15) in Chapter 5, the photocurrent signal obtained from the swept source OCT is described as

$$\begin{aligned}
 I(2k) &= 2|A^i|^2 \frac{W}{4\pi(z_{ref} + \Delta z)} \left( -k^2 \widetilde{P}_1(2k) \right) \\
 &= C \left( -k^2 \widetilde{P}_1(2k) \right),
 \end{aligned}$$

(6.1)

where

$$C = 2|A^i|^2 \frac{W}{4\pi(z_{ref} + \Delta z)}. \quad (6.2)$$

From Eq. (6.1), the integration is performed by dividing  $I(2k)$  by the frequency variable  $k$ , where  $-\frac{N}{2} < k < \frac{N}{2}$ , and  $N$  is the number of samples. The theoretical background will be explained in Chapter 7. Using the integration property by dividing by  $-k^2$ , we obtain

$$\hat{I}(2k) = \begin{cases} C(\widetilde{P}_1(2k)), & k \neq 0 \\ 0, & k = 0 \end{cases} \quad (6.3)$$

Applying an inverse Fourier transform to Eq.(6.3), the space domain signal  $P_1(z)$  without the Direct Current (DC) is obtained. The DC of the integrated function is removed during the integration process because the spectrum component at  $k = 0$  is forced to zero. Letting  $C'$  be the DC value of the function  $P_1(z)$ , then, the integrated function can be written as shown in Eq. (6.4).

$$\text{FT}^{-1}\{\hat{I}(2k)\} = C(P_1(z) - C') \quad (6.4)$$

### 6.1.2. Retrieval of the DC value of the complex scattering potential

The DC of the scattering potential can be regained by applying a known initial condition of  $P_1(z)$ . In OCT imaging, the first part of the A-scan signal is typically in air where  $n_s(0) = 1$  and  $n_a(0) = 0$ . Therefore, the scattering potential at  $z = 0$  becomes

$$\begin{aligned} P_1(0) &= n^2(0) - 1 = (n_s(0) - jn_a(0))^2 - 1 \\ &= 0 + j0 \end{aligned} \quad (6.5)$$

Hence, the difference between the first point of the integrated values and  $P_1(0)$  is equivalent to the required DC offset.

### 6.1.3. Approximate value of the scattering potential scale

To separate the profiles of the complex refractive index, it is necessary to know the value of the constant  $C$  as defined in Eq. (6.2),

$$C = 2|A^i|^2 \frac{W}{4\pi(z_{ref} + \Delta z)}.$$

The value of  $C$  is a dependent variable that relies on three factors;  $A^i$ ,  $z_{ref} + \Delta z$ , and  $W$ . The first two factors are possibly obtained from calibration process.  $W$  is dependent on the sample property which is difficult to measure. Instead of an exact value for  $C$ , its value can be approximated by the following method which is suitable for imaging tissue.

When imaging tissue, we can assume that the refractive index inside the sample is very close to that of water [47] where  $n_s = 1.32$  and  $n_a = 8.04 \times 10^{-5}$  at wavelength of 1310 nm [48]. Let  $z_o$  be an arbitrary position inside a tissue sample, then from Eq.(6.1), and Eq. (6.2) we can write

$$\hat{C}_{real} = \frac{\text{Re}\{CP_1(z_o)\}}{n_s^2(z_o) - 1} \tag{6.6}$$

and

$$\hat{C}_{img} = \frac{\text{Im}\{CP_1(z_o)\}}{2n_s(z_o)n_a(z_o)}, \tag{6.7}$$

where

$$C \times (n^2(z) - 1) = C_{real}(n_s^2(z) - 1) + C_{img}(2jn_s(z)n_a(z)). \tag{6.8}$$

#### 6.1.4. Obtaining scattering and absorption profiles from the complex scattering potential

From Eq. (6.8) and the approximated value of  $C_{real}$  and  $C_{img}$ , we have

$$C \times (n^2(z) - 1) \approx \hat{C}_{real}(n_s^2(z) - 1) + \hat{C}_{img}(2jn_s(z)n_a(z)) \quad (6.9)$$

Hence, the scattering and absorption profile of the sample can be computed as shown in Eq. (6.10) and (6.11).

$$\widehat{n}_s(z) \approx \sqrt{\text{Re}\{P_1(z)\} + 1}, \quad (6.10)$$

$$\widehat{n}_a(z) \approx \frac{\text{Im}\{P_1(z)\}}{2n_s(z)}. \quad (6.11)$$

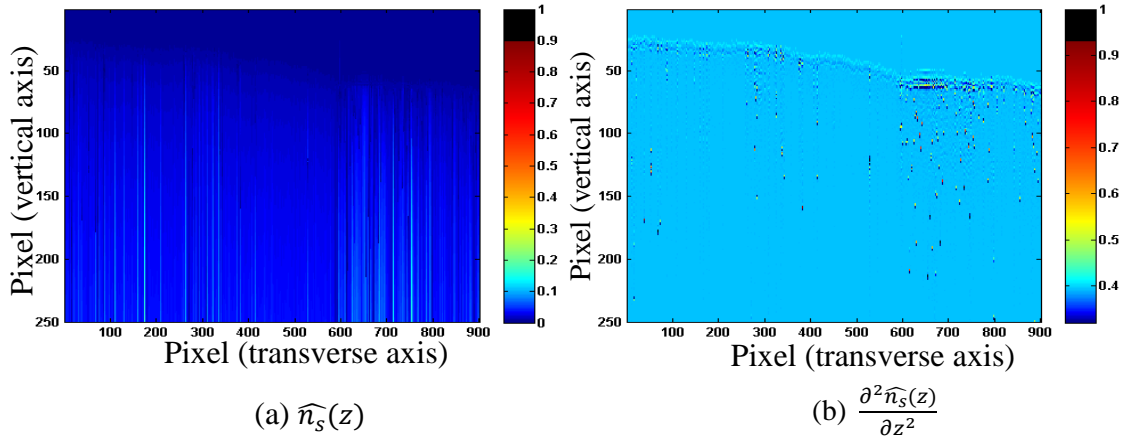
Therefore, we have successfully separated the scattering and absorption profiles of the sample.

## 6.2. Results of the OCT data

This section shows the results of separating scattering and absorption profiles explained in the last section. The lists of samples are the same with ones shown in Chapter 5. To visually compare the results from this chapter with the ones from the last chapter, we apply the 2<sup>nd</sup> derivative operator to obtain the 2<sup>nd</sup> derivative of the scattering and absorption profiles.

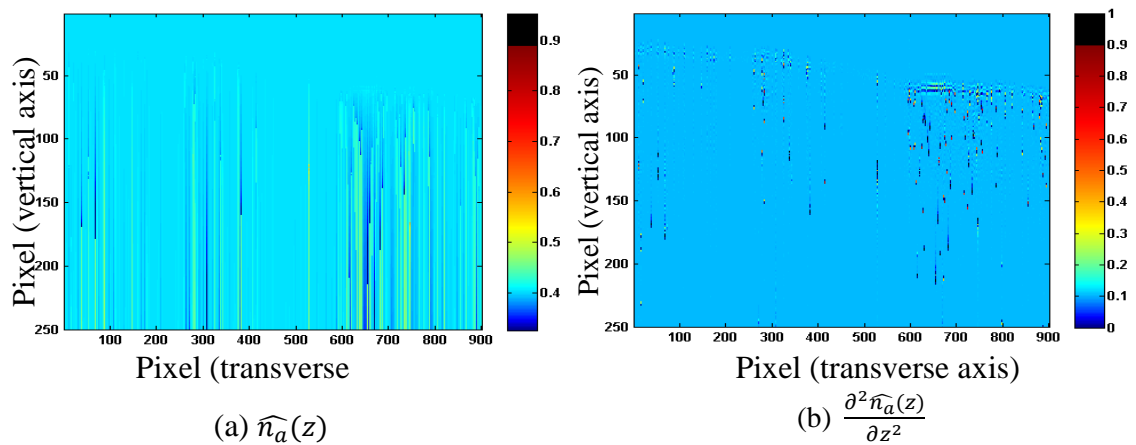
### 6.2.1.1. Sample 1: A fingertip without gloves

Figure 6-1 (a) shows the scattering profile of a fingertip. Figure 6-1 (b) shows the 2<sup>nd</sup> derivative of the scattering profile of the scattering profile



**Figure 6-1 Scattering profile of a fingertip**  
 (a) scattering profile (b) 2<sup>nd</sup> derivative of the scattering profile

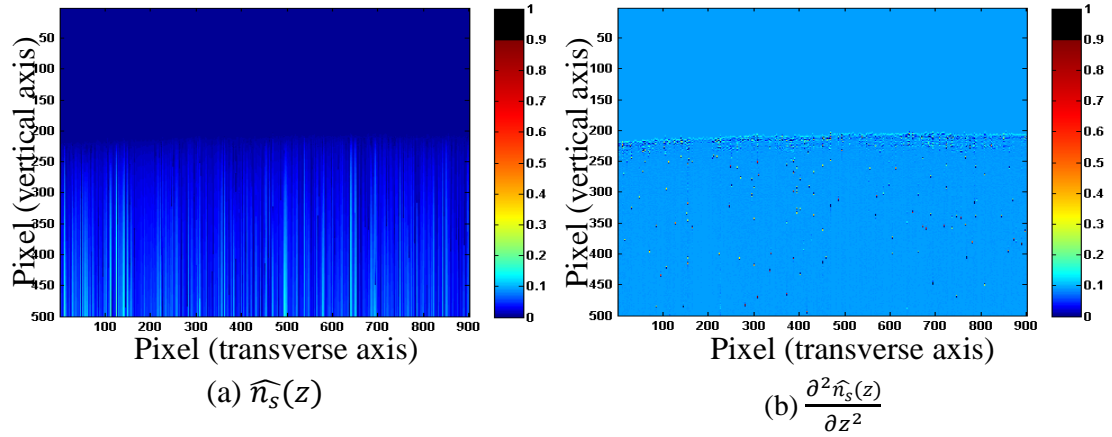
Figure 6-2 (a) shows the absorption profile of a fingertip. Figure 6-2 (b) shows the 2<sup>nd</sup> derivative of the absorption profile of the absorption profile



**Figure 6-2 Absorption profile of a fingertip**  
 (a) absorption profile (b) 2<sup>nd</sup> derivative of the absorption profile

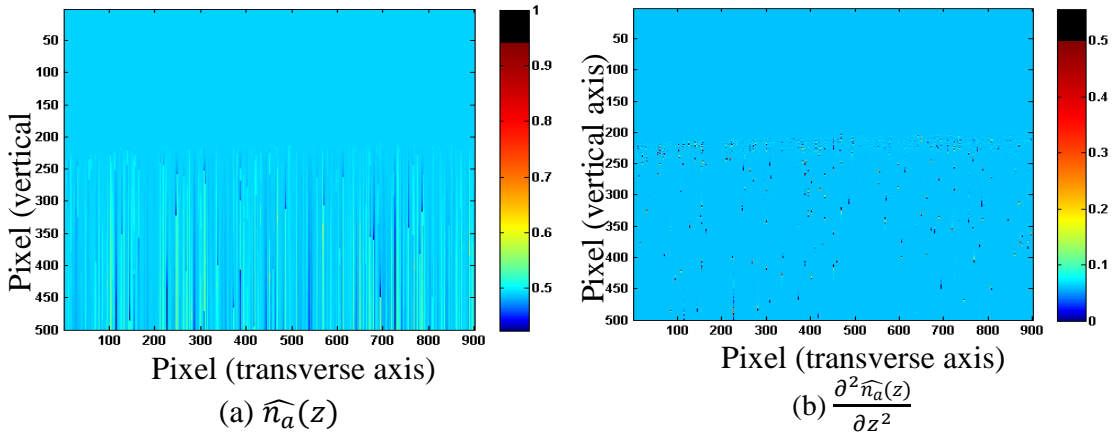
### 6.2.1.2. Sample 2: A fingertip with gloves

Figure 6-3 (a) shows the scattering profile of a fingertip with gloves. Figure 6-3 (b) shows the 2<sup>nd</sup> derivative of the scattering profile



**Figure 6-3 Scattering profile of a fingertip with gloves**  
 (a) scattering profile (b) 2<sup>nd</sup> derivative of the scattering profile

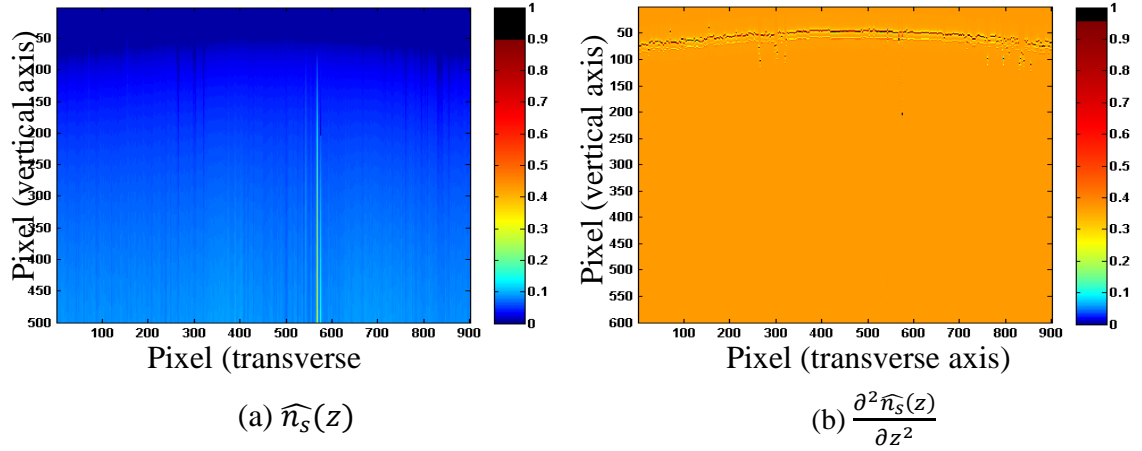
Figure 6-4 (a) shows the absorption profile of a fingertip with gloves. Figure 6-4 (b) shows the 2<sup>nd</sup> derivative of the absorption profile.



**Figure 6-4 Absorption profile of a fingertip with gloves**  
 (a) absorption profile (b) 2<sup>nd</sup> derivative of the absorption profile

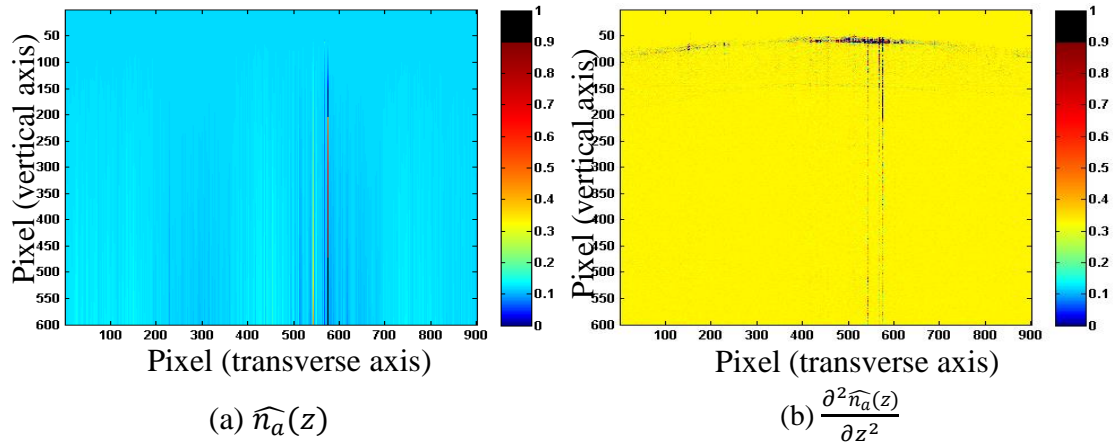
### 6.2.1.3. Sample 3: An axolotl embryo

Figure 6-5 (a) shows the scattering profile of an axolotl embryo. Figure 6-5 (b) shows the 2<sup>nd</sup> derivative of the scattering profile



**Figure 6-5 Scattering profile of an axolotl embryo**  
 (a) scattering profile (b) 2<sup>nd</sup> derivative of the scattering profile

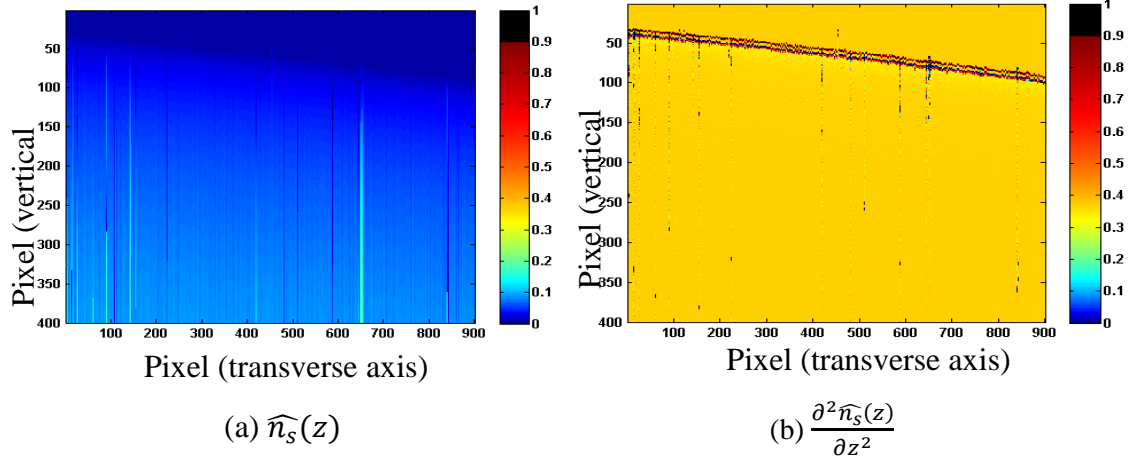
Figure 6-6 (a) shows the absorption profile of an axolotl embryo. Figure 6-6 (b) shows the 2<sup>nd</sup> derivative of the absorption profile



**Figure 6-6 Absorption profile of an axolotl embryo**  
 (a) absorption profile (b) 2<sup>nd</sup> derivative of the absorption profile

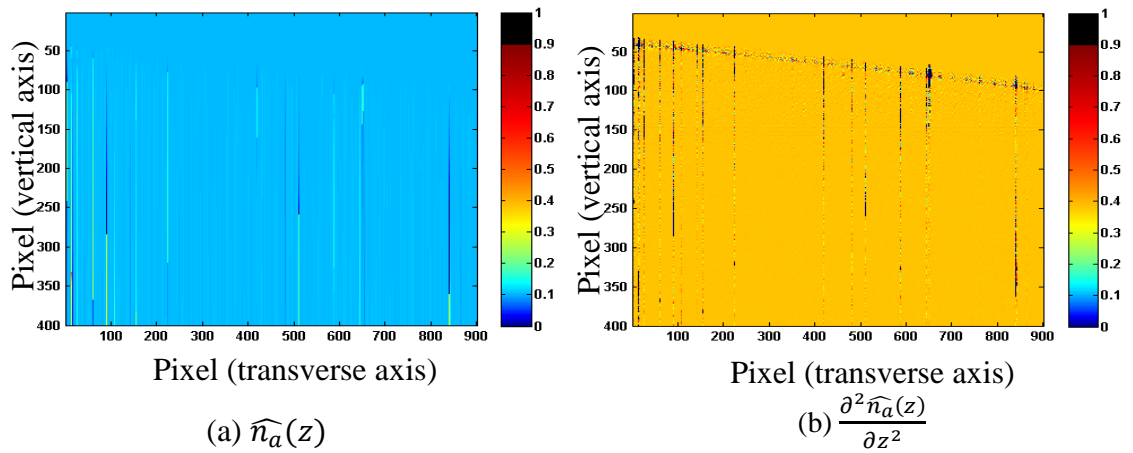
### 6.2.1.4. Sample 4: Clear adhesive tape

Figure 6-7 (a) shows the scattering profile of clear adhesive tape. Figure 6-7 (b) shows the 2<sup>nd</sup> derivative of the scattering profile



**Figure 6-7 Scattering profile of clear adhesive tape**  
 (a) scattering profile (b) 2<sup>nd</sup> derivative of the scattering profile

Figure 6-8 (a) shows the image of the absorption profile of clear adhesive tape. Figure 6-8 (b) shows the 2<sup>nd</sup> derivative of the absorption profile



**Figure 6-8 Absorption profile of clear adhesive tape**  
 (a) absorption profile (b) 2<sup>nd</sup> derivative of the absorption profile

## Chapter 7

### Implementation of differentiation and integration in the spectral domain

The procedure to separate the scattering and absorption effects explained in the last chapter requires numerical differentiation and integration processes. Because SS-OCT data is acquired in the spectral domain, the main focus of this chapter is to explain the methods and the implemented algorithms of the differentiation and integration in spectral domain. The methods were demonstrated with test functions and the results are shown at the end of the chapter.

#### 7.1. Theoretical background

##### 7.1.1. Discrete Fourier Transform (DFT)

In digital signal processing, the signal from the detector of the OCT system is given in a finite set of values in a function of time (or space). Thus, the algorithms are described in the discrete notation and the Fourier transform is represented by the Discrete Fourier transform (DFT). We begin the discussion on the derivative property of the Fourier transform by writing the Fourier transform of a function  $f(z)$  and its inverse Fourier transform as shown in Eq. (7.1) and Eq. (7.2).

$$F(k) = \int_{-\infty}^{\infty} f(z) e^{-j2\pi kz} dz, \tag{7.1}$$

$$f(z) = \int_{-\infty}^{\infty} F(k) e^{j2\pi kz} dk. \tag{7.2}$$

The Discrete Fourier transform (DFT) of the set of a discrete  $N$ -dimensional vector  $\{f_n\}$  can be represented by  $\{F_k\}$  as shown in Eq. (7.3) [42]:

$$F(k) = \frac{1}{N} \sum_{n=0}^{N-1} f(n) e^{-j2\pi n \left(\frac{k}{N}\right)}.$$

(7.3)

The inverse DFT can be described as shown in Eq. (7.4):

$$f(n) = \sum_{k=0}^{N-1} F(k) e^{j2\pi \frac{nk}{N}}.$$

(7.4)

The integer representation  $k$  is related to frequency which is defined for mathematical convenience, but it is not the same frequency as in the Fourier transform. For example, a set of  $f(n)$  consists of  $N$  samples separated by 1 second. The fundamental period of the data is  $N$  seconds which corresponds to the fundamental frequency of  $1/N$  hertz. Since the highest frequency (the Nyquist frequency) needed to represent the samples is 0.5 hertz,  $k/N$  where  $k$  is greater than  $N/2$  is greater than 0.5 hertz which is not equivalent to the frequency. In fact, the frequency  $k/N$  for  $k > N/2$  corresponds to the negative frequency [42]. For simplicity,  $F(k)$  and  $f(n)$  can be written as shown in Eq. (7.5) and Eq. (7.6). In practice, the DFT is computed using the Fast Fourier Transform (FFT) algorithm of Cooley-Tukey [49]:

$$F(k) = \frac{1}{N} \sum_{n=-N/2}^{N/2-1} f(n) e^{-j2\pi \left(\frac{k}{N}\right)n},$$

(7.5)

$$f(n) = \sum_{k=-\frac{N}{2}}^{\frac{N}{2}-1} F(k) e^{j2\pi \left(\frac{k}{N}\right)n}.$$

(7.6)

### 7.1.2. Differentiation in the spectral domain

Let  $f'(z)$  be the 1<sup>st</sup> derivative of  $f(z)$ , its Fourier transform can be written as

$$\text{FT}\{f'(z)\} = \int_{-\infty}^{\infty} f'(z) e^{-j2\pi kz} dz.$$

(7.7)

Eq. (7.7) can be expanded by integration by parts as

$$\text{FT}\{f'(z)\} = [f(z)e^{-j2\pi kz}]_{-\infty}^{\infty} - \int_{-\infty}^{\infty} f'(z) (-j2\pi k) e^{-j2\pi kz} dz.$$

(7.8)

From Cauchy principal value [50], the first term in the bracket vanishes; hence, we obtain

$$\begin{aligned} \text{FT}\{f'(z)\} &= (j2\pi k) \int_{-\infty}^{\infty} f(z) e^{-j2\pi kz} dz \\ &= (j2\pi k)F(k). \end{aligned}$$

(7.9)

A higher order derivative can be obtained by repeating the same procedure. Eq. (7.10) shows a generalized form for a higher order derivative:

$$\text{FT}\{f^q(z)\} = (j2\pi k)^q F(k).$$

(7.10)

In the discrete notation, we can write the  $q^{\text{th}}$  order derivative (when  $q$  is an interger) of the sequence  $f(n)$  as,

$$f^q(n) = \sum_{k=-\frac{N}{2}}^{\frac{N}{2}-1} \rho^q(k) F(k) e^{j2\pi \left(\frac{k}{N}\right)n},$$

(7.11)

where the frequency response  $\rho(k)$  is given by,

$$\rho(k) = j2\pi \frac{k}{N}.$$

(7.12)

### 7.1.3. Integration in the spectral domain

Integration can also be performed in the spectral domain [42, 45, 46]. The proof of the property can be explained by showing an integration of  $f(z')$  from  $-\infty$  to  $z$ . The integrated function can be written in the form of its Fourier transform as,

$$\int_{-\infty}^z f(z') dz' = \int_{-\infty}^z \left[ \int_{-\infty}^{\infty} F(k) e^{j2\pi k z'} dk \right] dz'.$$

(7.13)

Rearranging the order of integration, we obtain,

$$\int_{-\infty}^z f(z') dz' = \int_{-\infty}^{\infty} F(k) \left[ \int_{-\infty}^z e^{j2\pi k z'} dz' \right] dk.$$

(7.14)

Integrating the exponential term in the bracket from  $-\infty$  to  $z$ , we get

$$\begin{aligned} \int_{-\infty}^z f(z') dz' &= \int_{-\infty}^{\infty} \frac{1}{j2\pi k} F(k) [e^{j2\pi k z} - 0] dk \\ &= \int_{-\infty}^{\infty} \left[ \frac{1}{j2\pi k} F(k) \right] e^{j2\pi k z} dk. \end{aligned}$$

(7.15)

Eq. (7.15) implies that the Fourier transform of  $\int_{-\infty}^z f(z') dz'$  can be expressed as,

$$FT \left\{ \int_{-\infty}^z f(z') dz' \right\} = \begin{cases} \frac{1}{j2\pi k} F(k), & k \neq 0 \\ F(0)\delta(k), & k = 0. \end{cases}$$

(7.16)

If  $f(z')$  has zero mean, e.g.  $F(0) = 0$ , Eq. (7.16) can be written as

$$FT \left\{ \int_{-\infty}^z f(z') dz' \right\} = \frac{1}{j2\pi k} F(k).$$

(7.17)

In summary, the integration in the spectral domain process can be obtained by dividing  $F(k)$  with the frequency response  $j2\pi k$ , and the time domain function can be achieved by applying an inverse Fourier transform. The integrated function will have zero average because the value of  $F(0)$  is forced to zero.

The integration property of the Fourier transform can be described in discrete notation given in Eq. (7.18):

$$f(n) = \sum_{k=-\frac{N}{2}}^{\frac{N}{2}-1} F(k) e^{j2\pi\left(\frac{k}{N}\right)n}.$$

(7.18)

The integration in the spectral domain is done by multiplying Eq. (7.18) with a frequency response  $\eta^q(k)$ , where

$$\eta(k) = \begin{cases} 1 / \left( j2\pi \frac{k}{N} \right), & -\frac{N}{2} < k < \frac{N}{2} \text{ and } k \neq 0 \\ 0, & k = 0 \end{cases}$$

(7.19)

and  $q$  is the order of integration. Eq. (7.19) becomes

$$F(k) = \begin{cases} \left( \frac{1}{(j2\pi \frac{k}{N})} \right)^q F(k), & k \neq 0 \\ 0 \times F(0), & k = 0 \end{cases}.$$

(7.20)

In Eq. (7.20), the frequency response  $\eta(0)$  is forced to zero. This process eliminates the spectral value of  $F(k)$  at  $k = 0$ , i.e. the DC value of  $f(n)$ . This leads to  $f_{integrated}(n)$  that has zero mean when applying an inverse Fourier transform to Eq. (7.20). The DC offset of  $f_{integrated}(n)$  can be compensated with the prior knowledge of the initial boundary condition of the original  $f(n)$ , for example, the difference between the first position of the original  $f(n)$  and the  $f_{integrated}(n)$  given by

$$DC_{offset} = f(0) - f_{integrated}(0).$$

(7.21)

Then, the offset is added to  $f_{integrated}(n)$  as,

$$f_{integrated}(n) = f_{integrated}(n) + DC_{offset}.$$

(7.22)

## 7.2. Implementation of differentiation in the spectral domain

### 7.2.1. Buffered spectral differentiation

Spectral derivative using a standard FFT is an effective method for a function with a periodic boundary condition. On the other hand, representing the derivative of a non-periodic function using the method does not give a correct solution due to the Gibb's phenomenon [51]. The discontinuity in a non-periodic function causes the Gibb's phenomenon which creates a large oscillation near the endpoints which will be shown in the following example. Figure 7-1 shows a plot of a polynomial function. The 1<sup>st</sup> and the 2<sup>nd</sup> derivatives of the function are obtained by

solving the function analytically. The plots of the 1<sup>st</sup> and the 2<sup>nd</sup> derivatives are shown in Figure 7-2 (a) and (b), respectively.

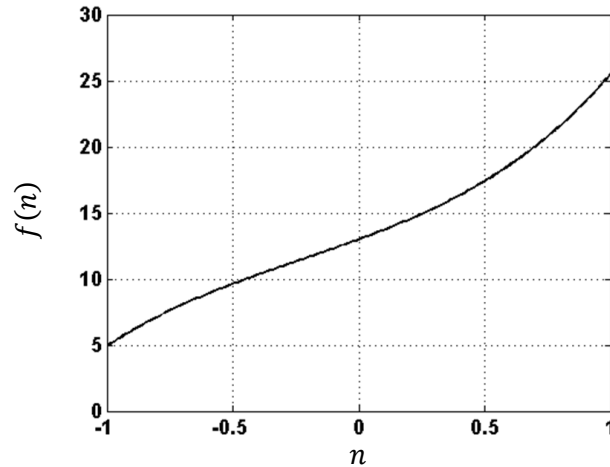


Figure 7-1 An arbitrary polynomial function

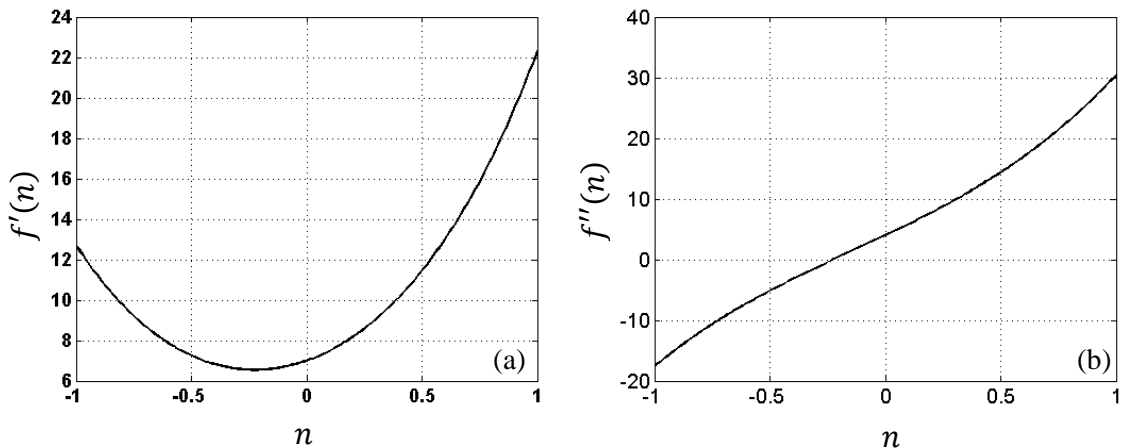
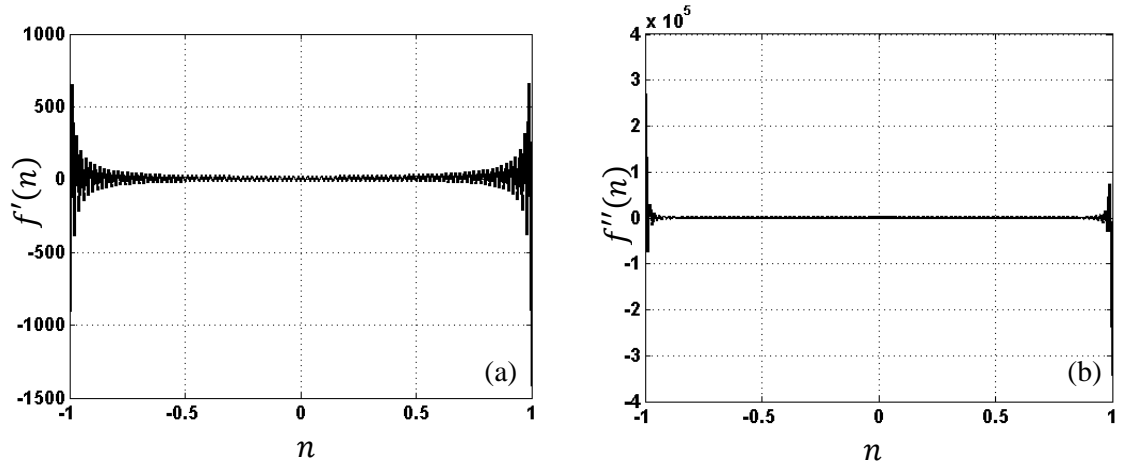


Figure 7-2 Analytical derivatives (a) 1<sup>st</sup> derivative and (b) 2<sup>nd</sup> derivative

We apply the differentiation in the spectral domain to the function shown in Figure 7-1 using Eq. (7.11) and Eq. (7.12). The 1<sup>st</sup> and the 2<sup>nd</sup> derivatives are computed by setting  $q = 1$  and  $q = 2$ , respectively. Figure 7-3 shows the results of using the differentiation technique. Gibb's phenomenon appears at the endpoints on both plots. The high oscillation at the end point distorts the shape of the derivative functions and results in unsatisfactory results.



**Figure 7-3 Derivatives using spectral derivative technique**  
**(a) 1<sup>st</sup> derivative and (b) 2<sup>nd</sup> derivative**

In 2012, Fu and Liu proposed a buffered Fourier spectral method to solve a non-periodic partial differential equation [51]. In their method, the Gibb's phenomenon which occurs from the discontinuity of a non-periodic function is reduced by duplicating the function to create periodicity. All duplicates of the function are joint together by buffer zones that are introduced to create the smoothness. From the experimental results, the method keeps high resolution and high order accuracy for non-periodic partial differential equations (PDEs). We used this technique in our numerical spectral differentiation method. The implementation of the technique will be described in the next paragraph.

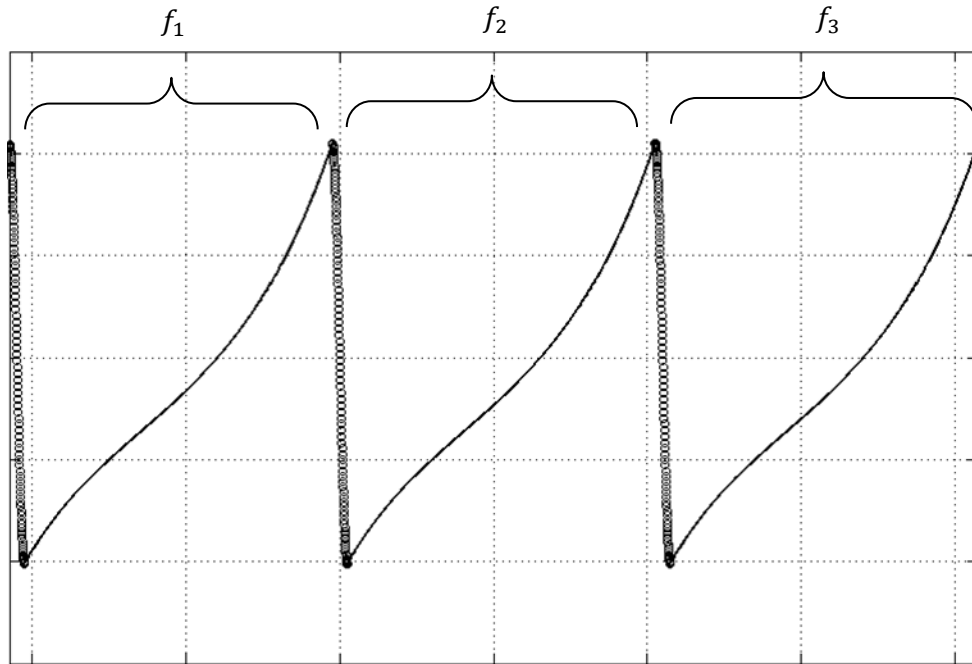


**Figure 7-4 A periodic function where the original function and its duplicates are shown in solid line and the buffered zones are represented by circle markers**

Let  $f(n)$  be the function shown in Figure 7-1. In Figure 7-4,  $f(n)$  is expanded into three periods, defined as  $f_1, f_2$ , and  $f_3$ , and the “buffer zones” (circle marker) are put between each period. This process is called a periodic continuation and the new function is defined as  $f_p(n)$ , where subscription  $p$  indicates the periodicity . Elements in the buffer zone which is a smooth joint between  $f_1, f_2$ , and  $f_3$  are interpolated by the Lagrange interpolation  $p(n)$  [52]. The mathematical function of the Lagrange interpolation is explained in APPENDIX B. Finally, the standard spectral derivative technique is applied to the new data set.

Since the derivatives contain the duplicated functions resulting from the periodic continuation, we choose only one period and discard the rest. Figure 7-5 shows the results of the 1<sup>st</sup> and the 2<sup>nd</sup> derivatives where the Gibb’s phenomenon at the endpoints is suppressed and show more accurate results.

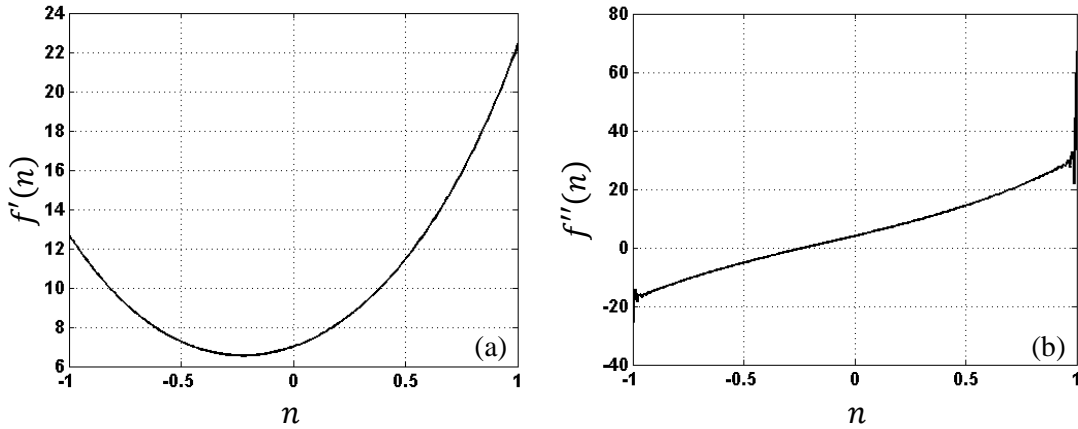


Figure 7-5 Plots of the 1<sup>st</sup> and 2<sup>nd</sup> derivatives using buffered spectral Fourier derivative technique

The summary of the algorithm is shown below.

---

Algorithm 1:  $q^{th}$  order derivative of a vector using Buffered spectral derivative

---

1. Given  $f(n)$  for  $-\frac{N}{2} \leq n \leq \frac{N}{2}$ , use periodic continuation method with Lagrange interpolation to compute  $f_p(m)$  for  $-\frac{M}{2} \leq m \leq \frac{M}{2}$  where  $M > N$
  2. Use an FFT to compute  $F_p(k)$
  3. Compute  $F_p^q(k)$  using spectral derivative technique
  4. Apply inverse FFT to  $F_p^q(k)$  to compute  $f_p^q(m)$
  5. Extract one period of the function, e.g.  $f^q(n)$ , from  $f_p^q(m)$  by discarding the two duplicating functions and the buffered zones
- 

### 7.2.2. Application to test functions

This section illustrates experimental results consisting of three examples. In each example, the 1<sup>st</sup> and the 2<sup>nd</sup> derivative of test functions are computed by the buffered spectral derivative technique.

The results are compared with the real 1<sup>st</sup> and the 2<sup>nd</sup> derivative functions.

- **Example 1**

Figure 7-6 shows the plot of the function  $f(n) = n^2$  where  $-1 \leq n \leq 1$ .

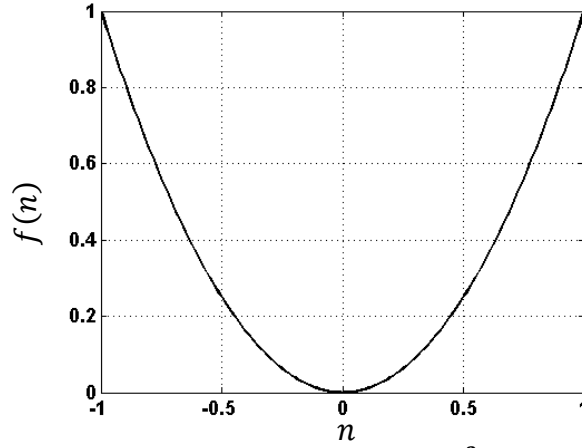


**Figure 7-6 Plot of  $f(n) = n^2$**

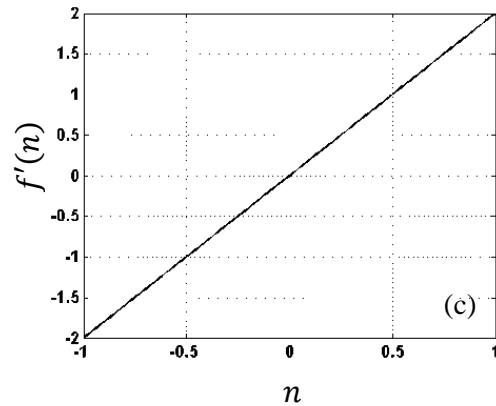
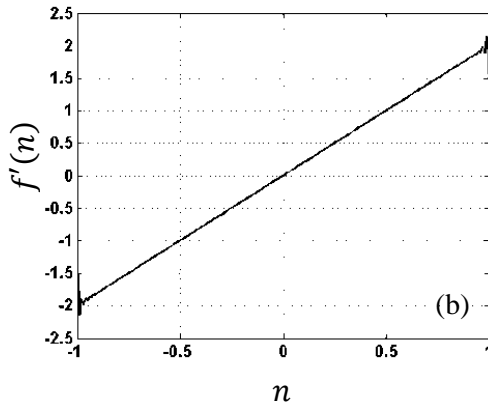
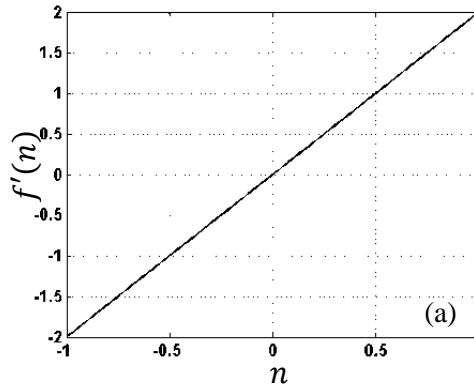


**Figure 7- 7 Plots of  $f'(n) = 2n$  (a) analytical (b)derivative using standard FFT, and (c) derivative using buffered spectral derivative**

Figure 7- 7(a) shows the plot of  $f'(n) = 2n$  from  $-1 \leq n \leq 1$  which is the real 1<sup>st</sup> derivative of  $f(n) = n^2$ . Then, we compare the real derivative function with the results from using the spectral derivative directly and using the buffered spectral derivative technique. Figure 7- 7 (b) is the derivative result from using the standard spectral derivative technique; it shows high oscillation at the end points. Figure 7- 7 (c) shows the result from the buffered spectral derivative technique which looks identical to the analytical derivative function.

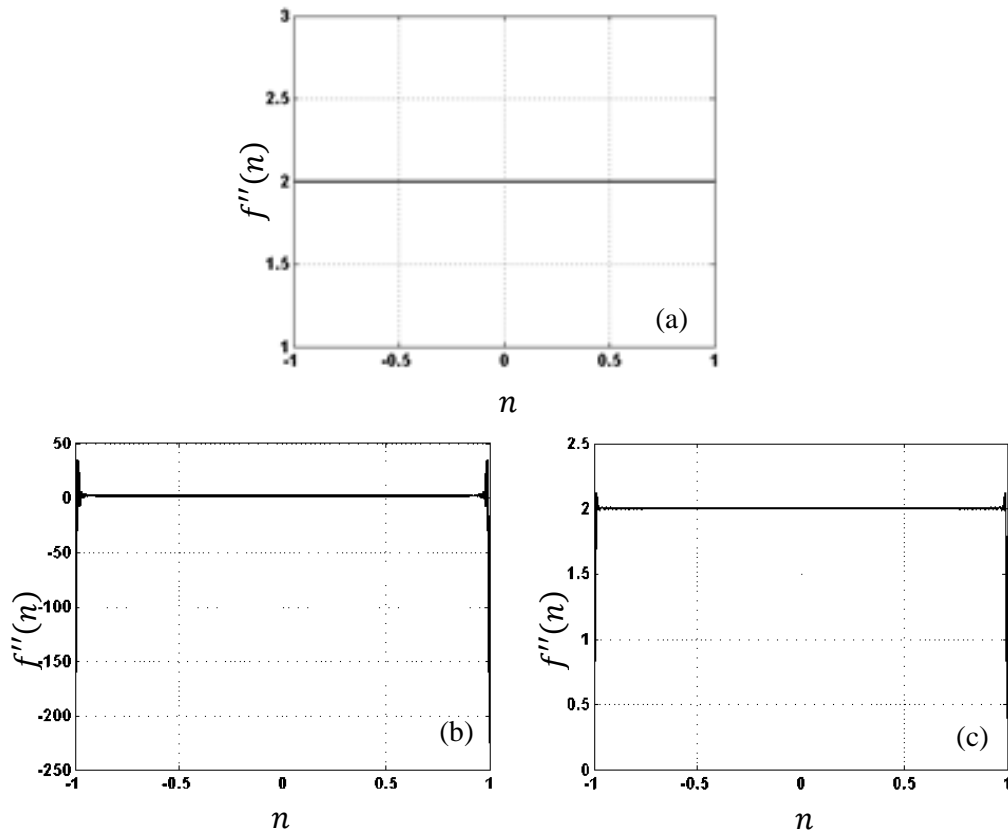


**Figure 7-7 Plots of  $f''(n) = 2$  (a) analytical (b) derivative using standard FFT, and (c) derivative using buffered spectral derivative**

The 2<sup>nd</sup> derivative of  $f(n)$  is  $f''(n) = 2$  and the plot in the range of  $-1 \leq n \leq 1$  is shown in Figure 7-7(a). Figure 7-7 (b) and (c) compare the results of using the standard spectral derivative and the buffered spectral derivative technique, respectively.

- **Example 2**

Figure 7-8 shows the plot of a polynomial function  $f(n) = -n^3 + 0.2n^2 + 0.7n + 1$  for  $-1 \leq n \leq 1$ .

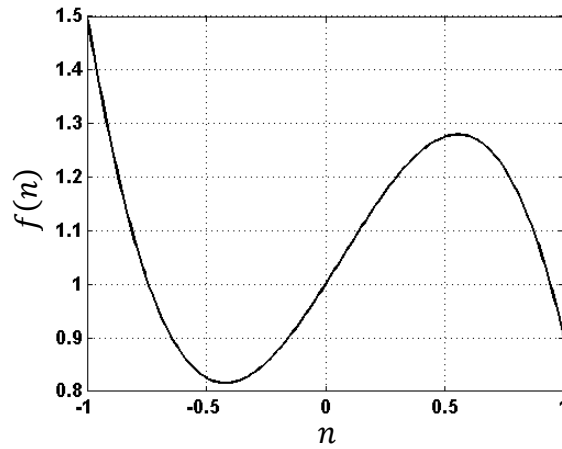


Figure 7-8 Plot of  $f(n) = -n^3 + 0.2n^2 + 0.7n + 1$

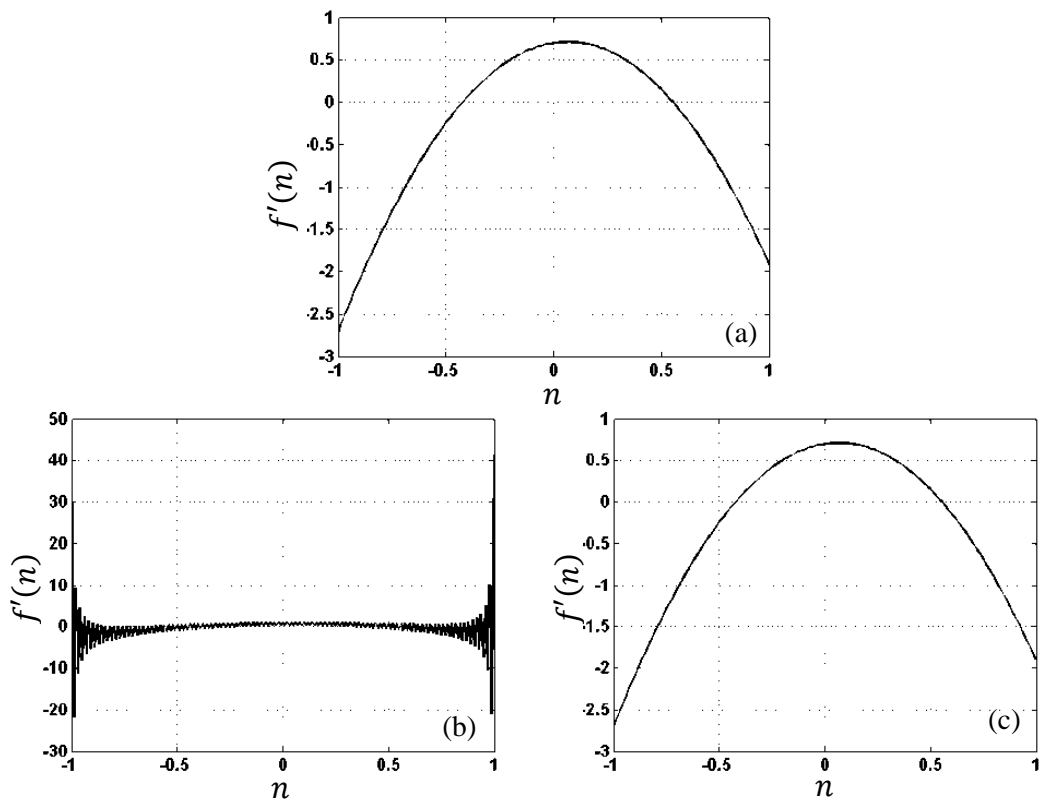
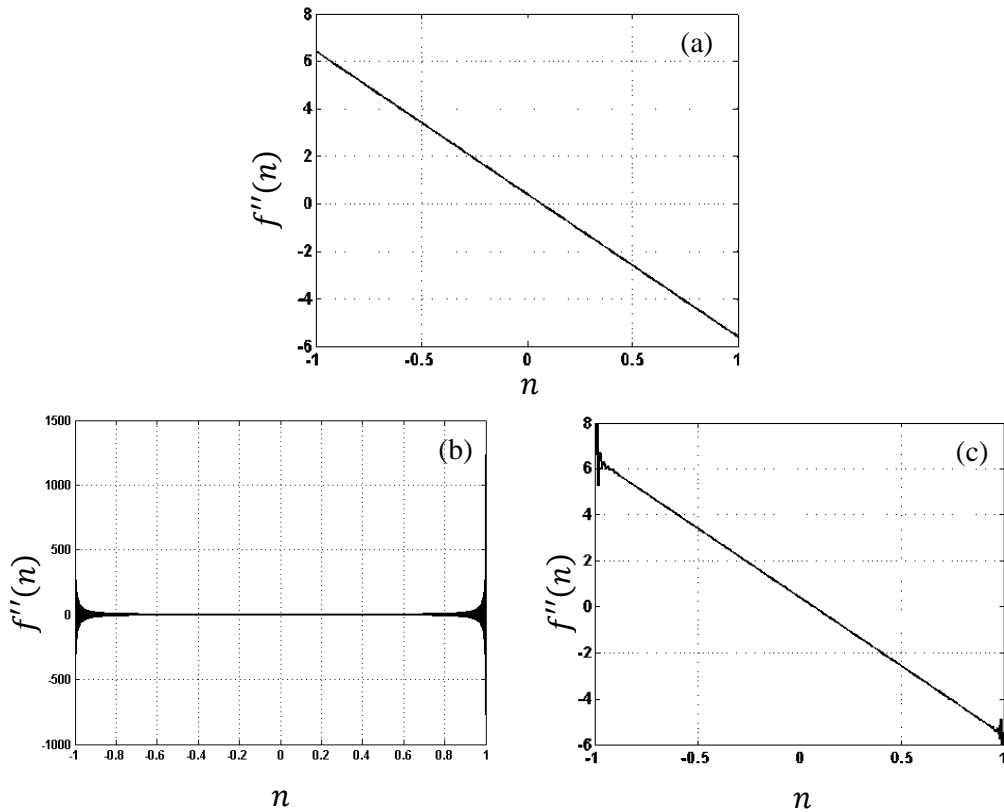


Figure 7-9 Plots of  $f'(n) = -3n^2 + 0.4n + 0.7$  (a) analytical (b) derivative using standard FFT, and (c) derivative using buffered spectral derivative

The 1<sup>st</sup> derivative of the function is  $f'(n) = -3n^2 + 0.4n + 0.7$  and the plot of the function in the range of  $-1 \leq n \leq 1$  is shown in Figure 7-9 (a). Figure 7-9 (b) and (c) show the 1<sup>st</sup> derivative of the function from the standard technique and the buffered spectral derivative technique, respectively.



**Figure 7-10 Plots of  $f''(n) = -6n + 0.4$  (a) analytical (b) derivative using standard FFT, and (c) derivative using buffered spectral derivative**

The 2<sup>nd</sup> derivative of the function is  $f''(n) = -6n + 0.4$  and the plot of the function ranging from  $-1 \leq n \leq 1$  is shown in Figure 7-10 (a). Figure 7-10 (b) is the result of using the standard technique. It shows high oscillation at the endpoints which highly affects the shape of the derivative. Figure 7-10 (c) is the result of using the buffered spectral derivative technique where the Gibb's phenomenon is suppressed and it reveals the correct shape.

- **Example 3**

The plot of a polynomial function  $f(n) = -\frac{1}{4}n^5 - \frac{7}{8}n^4 + \frac{3}{2}n^3 + 2n^2 - 2n + 2$  for  $-1 \leq n \leq 1$  is shown in Figure 7-11.

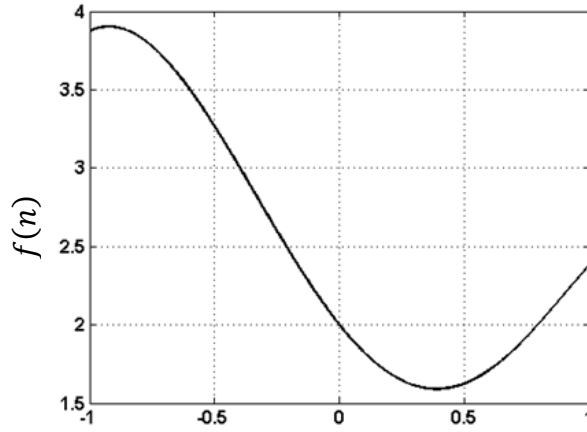


**Figure 7-11** Plot of  $f(n) = -\frac{1}{4}n^5 - \frac{7}{8}n^4 + \frac{3}{2}n^3 + 2n^2 - 2n + 2$

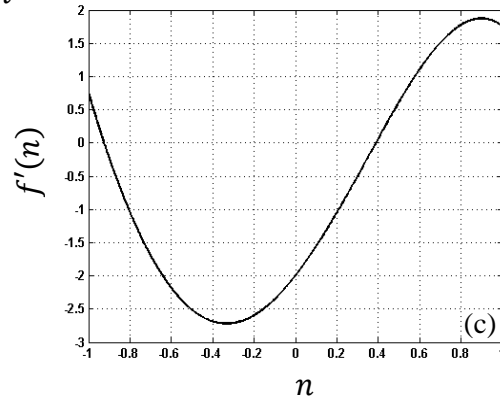
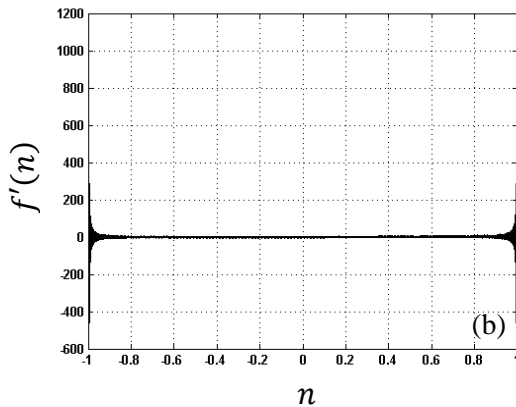
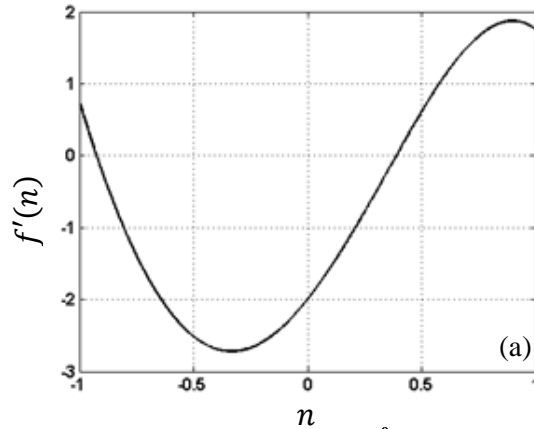


**Figure 7-12** Plots of  $f'(n) = -\frac{5}{4}n^4 - \frac{7}{2}n^3 + \frac{9}{2}n^2 + 4n - 2$

(a) analytical (b) derivative using standard FFT, and (c) derivative using buffered spectral derivative

Figure 7-12(a) illustrates the plot of  $f'(n) = -\frac{5}{4}n^4 - \frac{7}{2}n^3 + \frac{9}{2}n^2 + 4n - 2$  when  $-1 \leq n \leq 1$ .

Figure 7-12 (b) and (c) show the 1<sup>st</sup> derivative of the function from direct FFT derivative technique and the buffered spectral derivative technique, respectively.

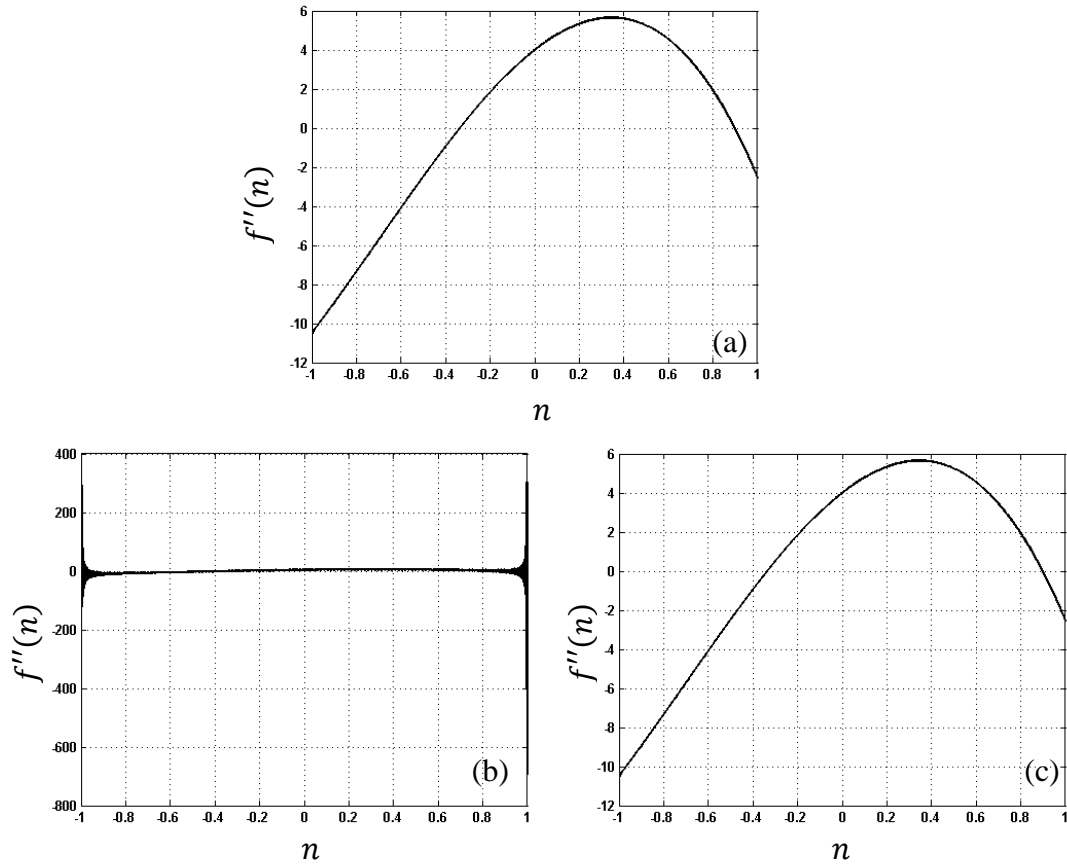


**Figure 7-13 Plots of  $f''(n) = -5n^3 - \frac{21}{2}n^2 + 9n + 4$ (a) analytical (b) derivative using standard FFT, and (c) derivative using buffered spectral**

The 2<sup>nd</sup> derivative of the function is  $f''(n) = -5n^3 - \frac{21}{2}n^2 + 9n + 4$  and the plot ranging from  $-1 \leq n \leq 1$  is shown in Figure 7-13(a). Figure 7-13 (b) shows the result of using the standard technique. Figure 7-13 (c) show a satisfactory result of using the buffered spectral derivative technique.

### 7.3. Implementation of integration in the spectral domain

#### 7.3.1. Buffered spectral integration

Similar to the differentiation, periodicity and discontinuity of the to-be-integrated function affects the final outcome. The frequency response  $\eta(k) = 1/(j2\pi \frac{k}{N})$  behaves like a low-pass filter or a smoothing operator. The signal at high frequency (high  $k$ ) is suppressed and the signal at the low frequency (low  $k$ ) is amplified. For a function that is smooth, the integrating process will give an inadequate result; an over-smoothing  $f(n)$ . For example, Figure 7-14 (a) shows the plot of  $f'(n)$ . Figure 7-14 (b) compares plots between the original  $f(n)$  in dashed line and the result (with DC offset) from the integrating in the spectral domain in solid line. Figure 7-14 (c) shows the incorrect result (in solid line) after the DC offset is compensated.

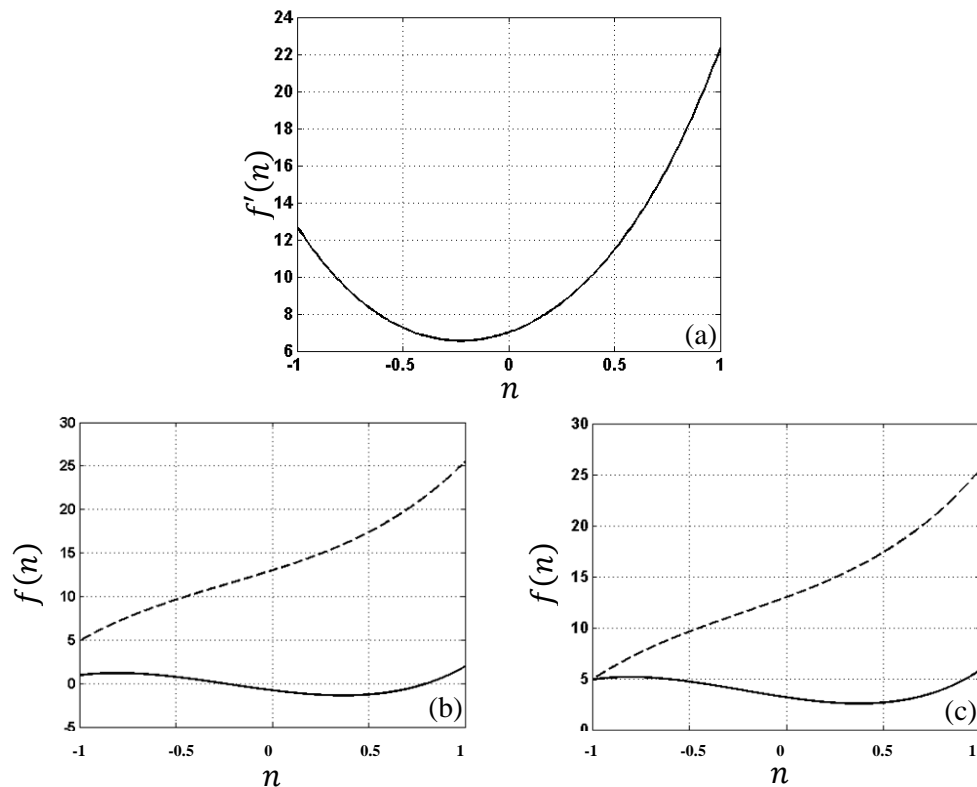
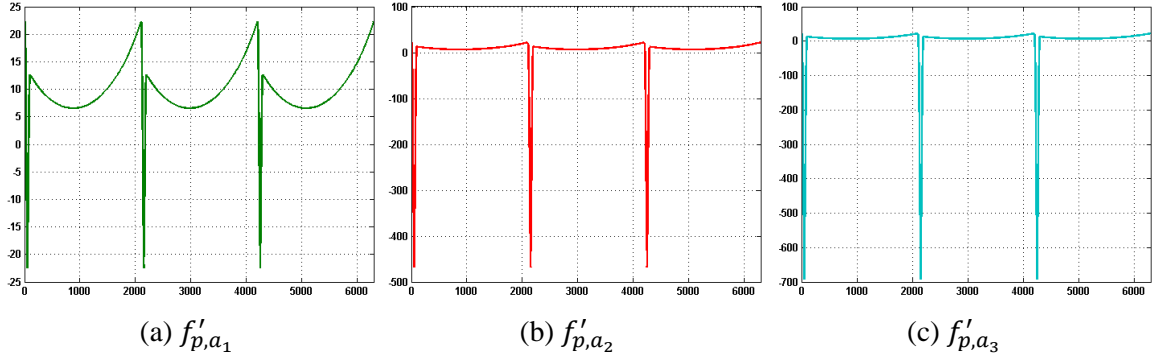


Figure 7-14 Integration in The spectral domain (a) given a smooth non-periodic  $f'(n)$  (b) comparison plots between  $f(n)$  (dashed line) and the incorrect result  $f(n)$ , and (c) incorrect  $f(n)$  after DC offset compensation

In this thesis, we proposed a method to solve the problem using the periodic continuation process together with an optimization. First, the same periodic continuation process is applied to  $f'(n)$  which gives three periods of  $f'(n)$  and the buffer zones. The new periodic function is defined as  $f'_p$ . In the differentiation process, the linkage between each period is smoothed using Lagrange interpolation which is different from the integration. In the integration, a spike function is used to disrupt the continuity between each period, and the amplitude of the spike is varied with a constant  $a$ , where  $a \in \mathcal{R}$ . Figure 7-15 shows plots of periodic functions  $f'_{p,a_1}$ ,  $f'_{p,a_2}$ , and  $f'_{p,a_3}$  where  $|a_3| > |a_2| > |a_1|$ .



**Figure 7-15** Plots of  $f'_{p,a}$  where (a)  $a = a_1$ , (b)  $a = a_2$ , and  
(c)  $a = a_3$  and  $|a_3| > |a_2| > |a_1|$

The integrated functions of  $f'_{p,a_1}$ ,  $f'_{p,a_2}$ , and  $f'_{p,a_3}$  are called  $f_{p,a_1}$ ,  $f_{p,a_2}$ , and  $f_{p,a_3}$ . Then, one period, excluding the buffer zone, is chosen from the periodic function and defined as  $f_{p,a_1}(n)$ ,  $f_{p,a_2}(n)$ , and  $f_{p,a_3}(n)$ . Figure 7-16 compares the results, when the constant  $a$  or the amplitude of the spike functions are varied, with the real  $f(n)$ . The results show that at  $a_2$ , the integrated result is almost identical to the original function. This shows that there is an optimal point of the spikiness that gives the correct solution.

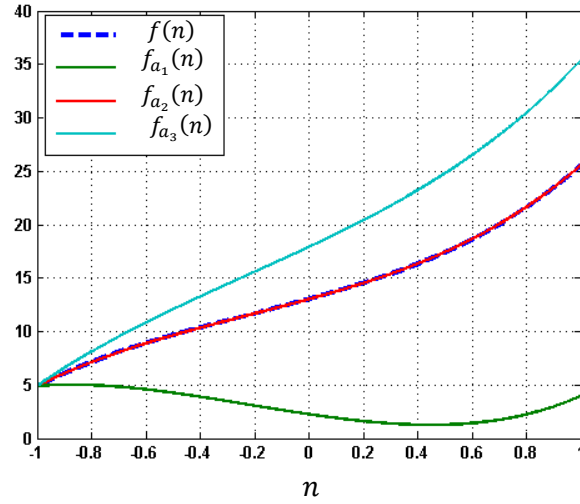


**Figure 7-16 Comparison plots of the results from the integration method and the original  $f(n)$**

In our method, an iterative process is used to find an optimal value of  $a$ . This can be done by taking the derivative of the integrated function  $f_a(n)$ , e.g.  $f'_a(n)$  and find the root-mean-square (RMS) error between  $f'(n)$  and  $f'_a(n, a)$ . The RMS error is computed from Eq. (7.23) [53].

$$\text{RMS}_{\text{error}} = \left( \frac{\sum_{n=1}^N (f'(n) - f'_a(n))}{N} \right)^{1/2} \quad (7.23)$$

The iteration process continues by varying input  $a$  until the RMS error is less than a certain value  $\epsilon$  as shown in Eq. (7.24).

$$\text{RMS}_{\text{error}} \leq \epsilon \quad (7.24)$$

Figure 7-17 illustrates the plots of  $f_a(n)$  converging to  $f(n)$  as the level of the spike function increases.

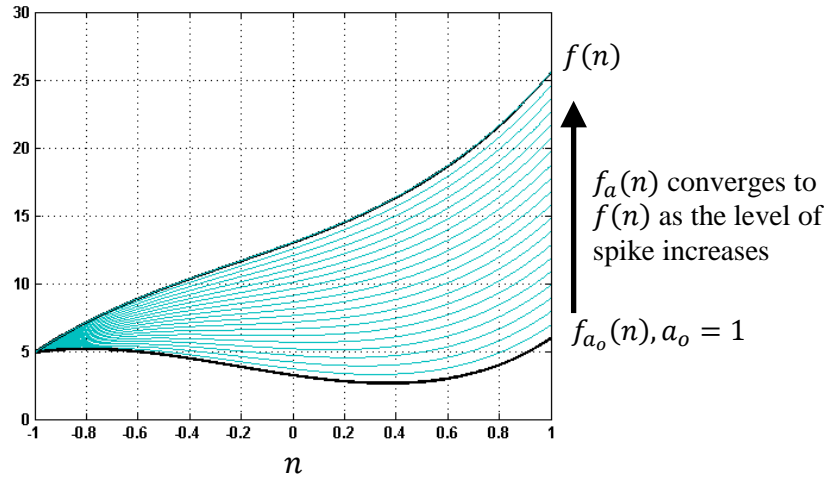


**Figure 7-17**  $f_a(n)$  converges to  $f(n)$  during the iterative process

The algorithm of the proposed integration technique is shown below.

---

Algorithm 2: Integration in spectral domain of the  $q^{th}$  order derivative of a vector

---

1. Given  $f^q(n)$  for  $-\frac{N}{2} \leq n \leq \frac{N}{2}$ . Use periodic continuation method to compute  $f_{p,a}^q$  where  $a$  is the initial value (default is 1)
  2. Use an FFT to compute  $F_{p,a}^q(k)$
  3. Use spectral integration method to obtain  $F_{p,a}(k)$
  4. Compute  $f_{p,a}$  from  $F_{p,a}(k)$  via an inverse FFT
  5. Use spectral derivative to compute  $f'_{p,a}$
  6. Extract  $f'_a(n)$  from  $f'_{p,a}$
  7. Compute the RMS error according to Eq. (7.23), if  $\text{RMS}_{\text{error}} > \epsilon$  repeat step 1 to step 7 by varying  $a$
  8. Stop the iteration when  $\text{RMS}_{\text{error}} \leq \epsilon$
- 

### 7.3.2. Experimental results of test functions

This section shows the experimental result which includes three examples (same as in section 7.2.2) where we apply the technique to restore  $f(n)$  from its 2<sup>nd</sup> derivative. The results are benchmarked with the true  $f(n)$  and results of using the numerical integration based on the rectangle method to find the approximated definite integral.

- **Example 1**

The 2<sup>nd</sup> derivative function  $f''(n) = 2$  is shown in Figure 7-18.

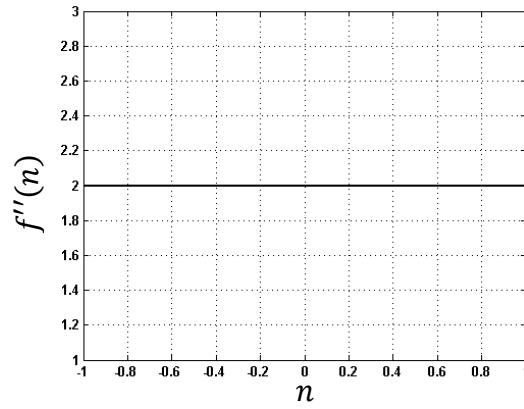


**Figure 7-18** Plot of the second derivative  $f''(n) = 2$

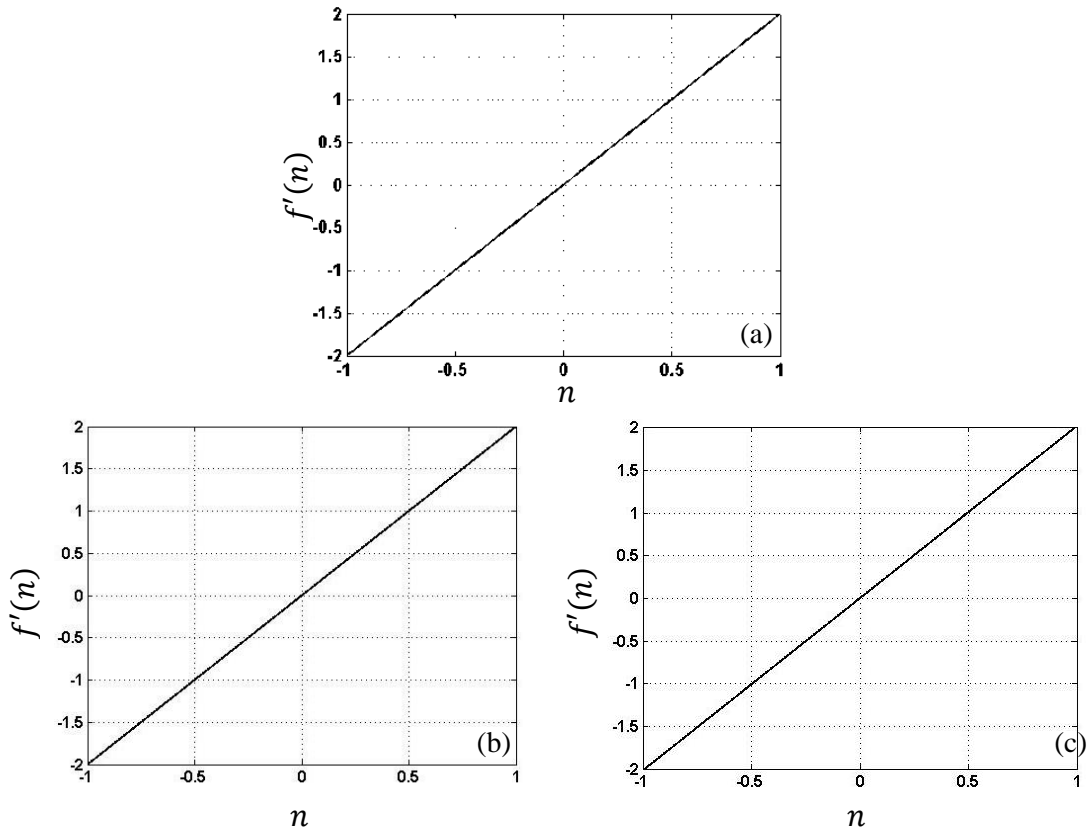


**Figure 7-19**  $f'(n) = 2 \times n$  (a) analytical  
(b) cumulative sum method, and (c) integration in the spectral domain

The function is integrated using the proposed integration method to find  $f'(n) = 2 \times n$  and compared with the result from the numerical integration from cumulative sum. Figure 7-19 (a) shows the plot of  $f'(n) = 2 \times n$  for  $-1 \leq n \leq 1$ . Figure 7-19 (b) and (c) compare the integrated results using cumulative sum and the proposed integration method.

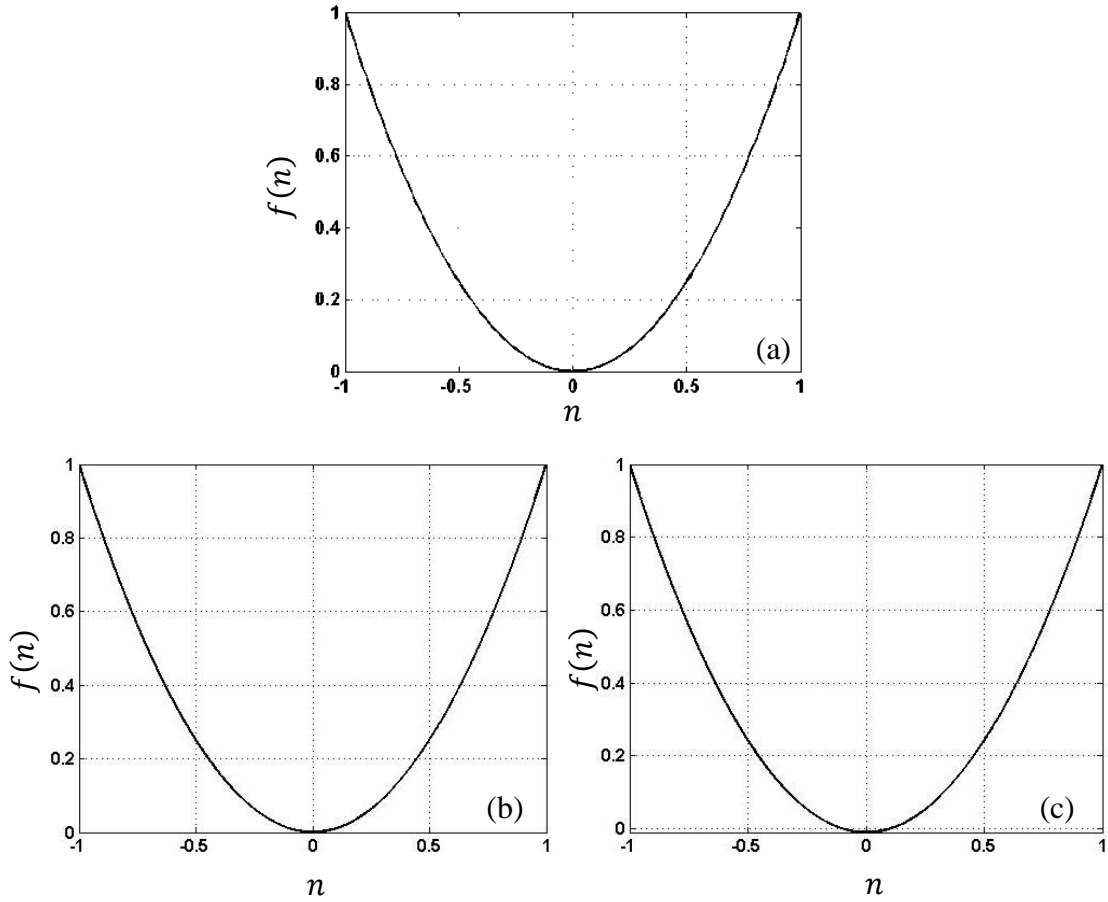


**Figure 7-20**  $f(n) = n^2$ (a) analytical  
(b) cumulative sum method, and (c) integration in the spectral domain

The algorithm is further tested by integrating the 1<sup>st</sup> derivative function to restore  $f(n) = n^2$ . The plot of the function  $f(n) = n^2$  from  $-1 \leq n \leq 1$  is shown in Figure 7-20 (a). Figure 7-20 (b) and (c) show the results from the integration using cumulative sum method and the proposed method.

- **Example 2**

Figure 7-21 shows the plot of the initial function  $f''(n) = -6n + 0.4$  for  $-1 \leq n \leq 1$ .

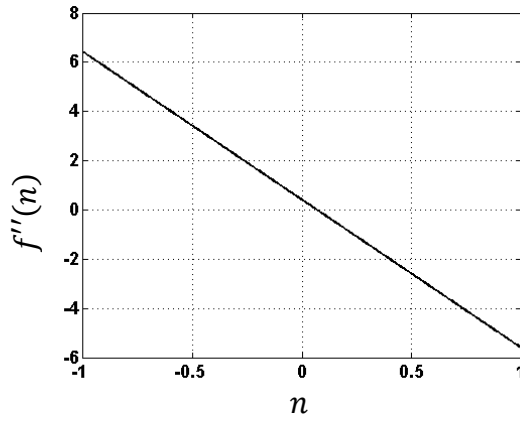


Figure 7-21 The plot of  $f''(n) = -6n + 0.4$

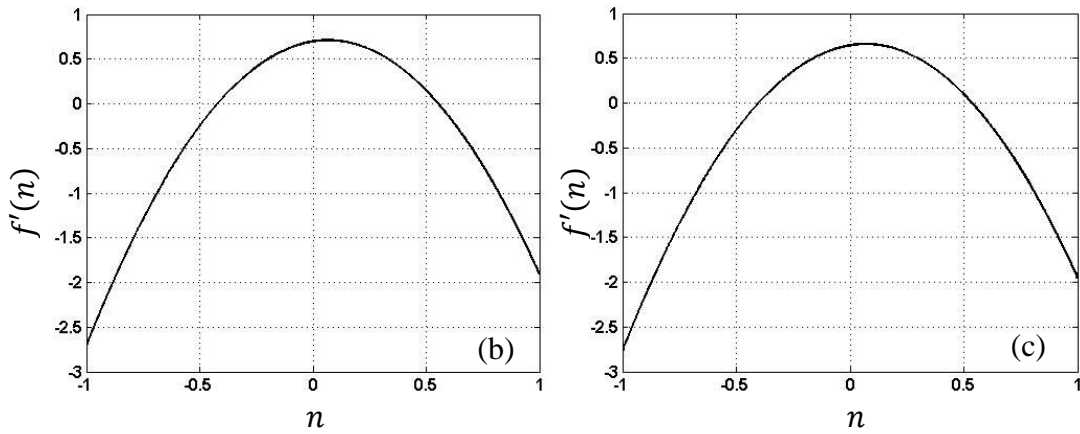
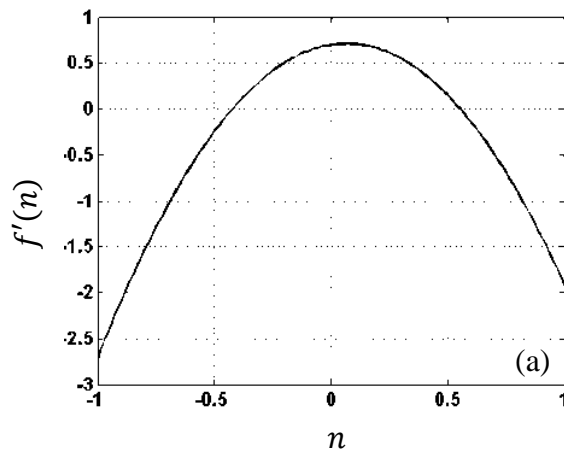
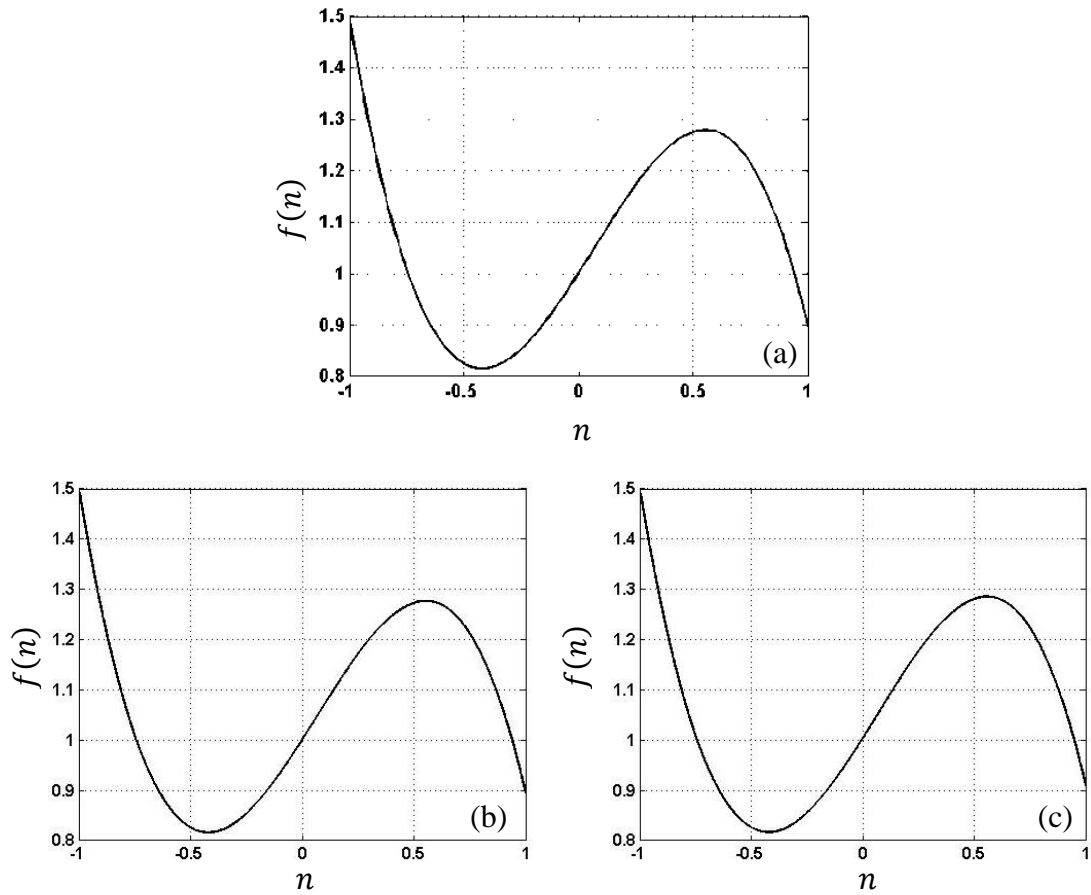


Figure 7-22  $f'(n) = -3n^2 + 0.4n + 0.7$  (a) analytical  
(b) cumulative sum method, and (c) integration in the spectral domain

Figure 7-22 (a) shows the plot  $f'(n) = -3n^2 + 0.4n + 0.7$  where  $-1 \leq n \leq 1$ . The results from integrating by cumulative sum is shown in Figure 7-22 (b) and the result from the proposed technique is shown in Figure 7-22 (c)



**Figure 7-23  $f(n) = -n^3 + 0.2n^2 + 0.7n + 1$ (a) analytical, (b) cumulative sum method, and (c) integration in the spectral domain**

Figure 7-23 (a) shows the plot  $f(n) = -n^3 + 0.2n^2 + 0.7n + 1$  from  $-1 \leq n \leq 1$ . The results from integration using cumulative sum and the proposed integrating method are shown in Figure 7-23 (b) and (c).

- **Example 3**

Figure 7-24 shows the plot of the initial function  $f''(n) = -5n^3 - \frac{21}{2}n^2 + 9n + 4$  from  $-1 \leq n \leq 1$ .

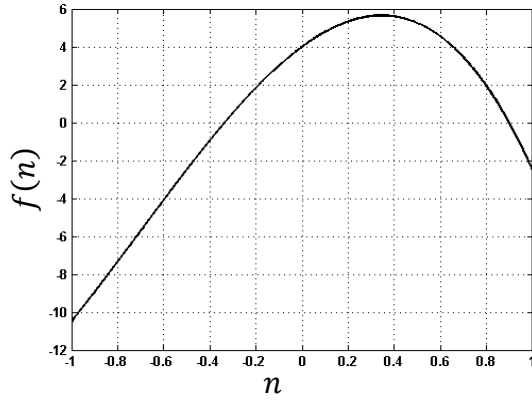


**Figure 7-24** Plot of  $f''(n) = -5n^3 - \frac{21}{2}n^2 + 9n + 4$

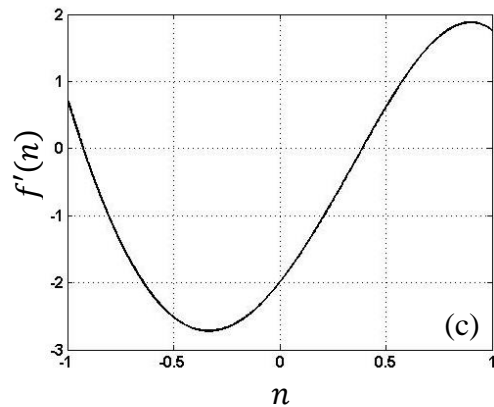
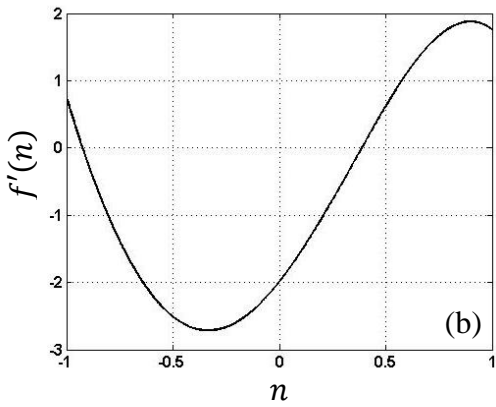
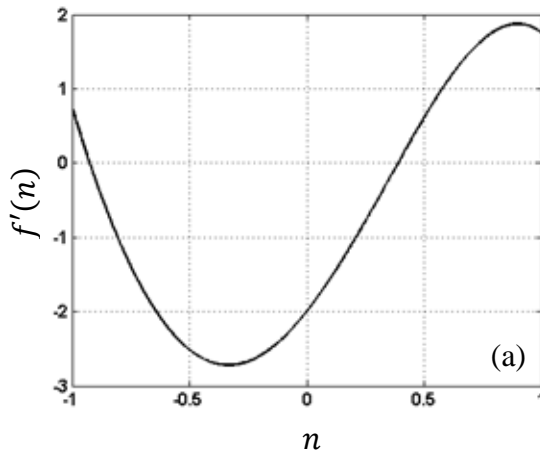


**Figure 7-25**  $f'(n) = -\frac{5}{4}n^4 - \frac{7}{2}n^3 + \frac{9}{2}n^2 + 4n - 2$  (a) analytical (b) cumulative sum method, and (c) integration in the spectral domain

The integrated results using rectangle method (shown in Figure 7-25(b)) and the result from the proposed method (shown in Figure 7-25 (c)) are compared with the real  $f'(n) = -\frac{5}{4}n^4 - \frac{7}{2}n^3 + \frac{9}{2}n^2 + 4n - 2$  Figure 7-25 (a).

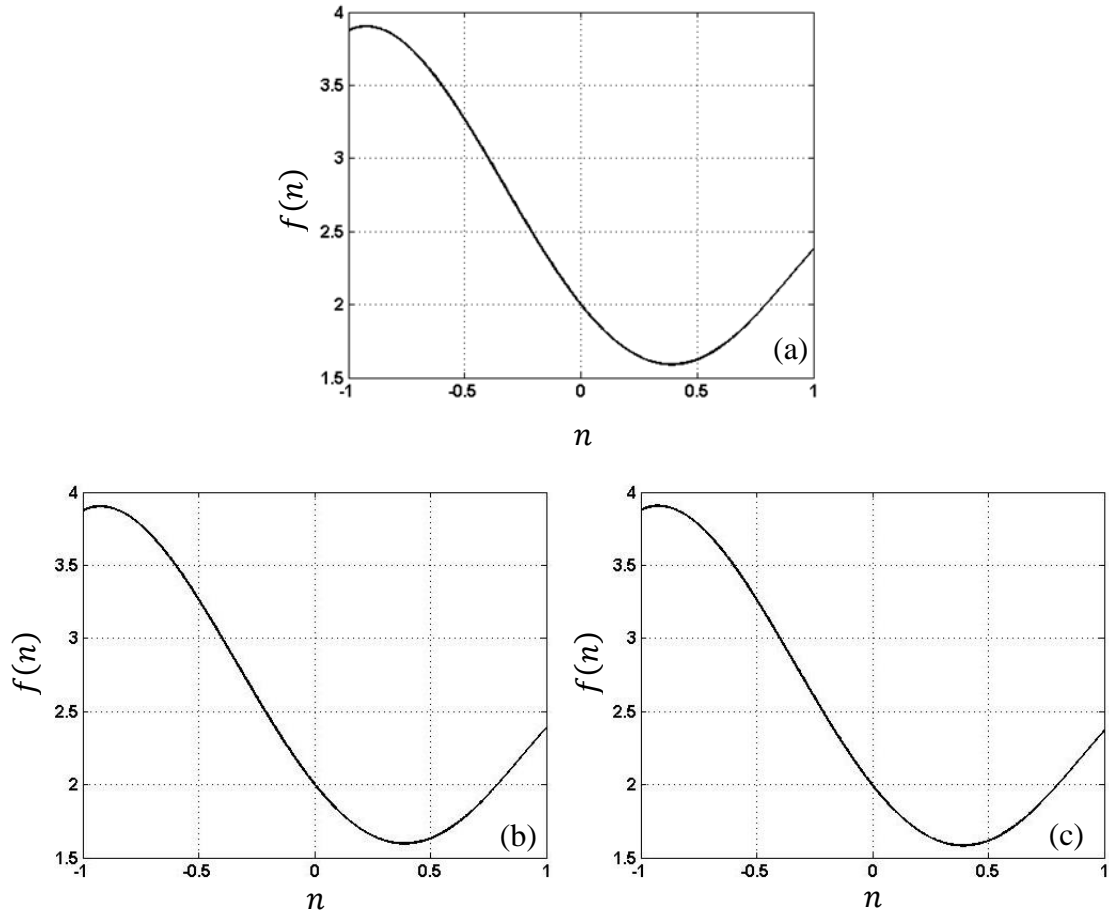


**Figure 7-26**  $f(n) = -\frac{1}{4}n^5 - \frac{7}{8}n^4 + \frac{3}{2}n^3 + 2n^2 - 2n + 2$  (a) analytical (b) cumulative sum method, and (c) integration in the spectral domain

The results of integrating the first derivative function using rectangle method and the proposed method are shown in Figure 7-26 (b) and (c). The integrated results are compared with the real  $f(n) = -\frac{1}{4}n^5 - \frac{7}{8}n^4 + \frac{3}{2}n^3 + 2n^2 - 2n + 2$  where the plot is shown in Figure 7-26 (a) where  $-1 \leq n \leq 1$ .

## Chapter 8

### Summary and future development

The work in this thesis could be divided into two parts: 1) the implementation of a time-domain OCT system in which I completely implemented the optical module, 2) development of a method to extract scattering and absorption profiles from the scattering potential using a quadrature SS-OCT.

Our time-domain OCT system consists of an Optical Module and a Data Acquisition Module where implementation details were described in Chapter 3. The design of the optical module was based on a Mach-Zehnder interferometer, which offers a better SNR compared to a Michelson interferometer. In addition to the Optical Module, a Data Acquisition Module was implemented by one of my colleagues. The Data Acquisition Module allows a user to control the optical system and to acquire and store OCT images. GUI OCT system was used to image many samples and an example of those images can be found in Chapter 4.

The second part of this work is development of a method to extract scattering and absorption profiles from the scattering potential using a quadrature SS-OCT. We demonstrated how the swept source quadrature OCT can be used in extracting the complex scattering potential of a sample. We introduced a new interpretation of the OCT images as the 2<sup>nd</sup> derivative of the scattering potential of an object. We demonstrated the validity of our method by applying to different quadrature SS-OCT images of different objects. Results for our method show that quadrature OCT is suitable to be used as a spectroscopic imaging technique.

Following is a list of suggested future work.

- Add capability of SS-OCT to our TD-OCT system.
- Add quadrature SS-OCT capability to extend the functionality

- Develop a faster integration and differentiation for extracting the scattering and absorption profiles.

## APPENDIX A.

### Time-Frequency Analysis

This appendix is a brief review of different techniques of the time-frequency analysis.

#### A.1. Linear time-frequency analysis

In this section, the short-term periodic behavior of a signal is observed locally. The most fundamental analysis tool in this family is short-time Fourier transform (STFT) and spectrogram. Then, a more flexible analysis tool, known as wavelet representations, is discussed.

##### A.1.1. Short-time Fourier Transform

An essential time-frequency analysis in this domain is a windowed Fourier transform or a short-time Fourier transform (STFT). The basic idea of this approach is to linearly decompose a signal into “atoms” by a “sliding window” in time. The Fourier transform is applied to the signal inside the window to obtain its local spectrum components; therefore, the STFT is a function of time and frequency. In practice, a window function, The STFT is defined in [54] as.

$$\text{STFT}_x^g(t, f) = \int_{-\infty}^{\infty} x(t')g^*(t' - t)e^{-j2\pi ft'} dt'.$$

(A.1)

where  $g(t)$  is a window function. The window  $g(t)$  is generally an even function window or Gaussian window, with positive real values concentrated around the origin. Apart from having a good choice of the window size, the shape of the window is also important for signal representation. False peak detections may occur when the shape of the chosen window does not fit the signal [54]. Examples of shapes of the analysis windows are rectangular window, truncated Gaussian window, and Hanning window.

### A.1.2. Wavelet-type representations

A more flexibility can be found in a multi-scale analysis known as wavelet-type representations. In continuous wavelet transform (CWT), a signal is projected on a family of functions, known as wavelets. The functions are deduced from an elementary function called mother wavelet by translation ( $t'$ ) and scaling ( $a$ ) factors as

$$\psi_{t',a}(t) = \frac{1}{\sqrt{a}} \psi\left(\frac{t-t'}{a}\right). \quad (\text{A.2})$$

An example of a wavelet is Morlet wavelet which is a modulated Gaussian:  $\psi(t) = e^{-t^2+j2\pi f_0 t}$  with  $f_0 = 1/\sqrt{\ln 2}$  [54]. The wavelet coefficients resulting from applying the wavelets to the signal is given by

$$\text{CWT}_x^\psi(t', a) = \int_{-\infty}^{\infty} x(t) \frac{1}{\sqrt{a}} \tilde{\psi}^*\left(\frac{t-t'}{a}\right) dt. \quad (\text{A.3})$$

The main difference between the STFT and CWT is the scaling factor  $a$  that is introduced in CWT. In contrast to STFT, the scaling factor  $a$  in CWT in which its effect will vary the time-frequency resolution based on the length of the analysis window. Short windows are used at high frequencies and long windows are used at low frequencies. This makes the analysis more suitable with the real world signal.

### A.2. Energy distributions of a signal

Before moving to the second class of time-frequency analysis, it is important to have a background about signal energy. The energy of the signal can be calculated from the squared modulus of the signal in temporal and its Fourier representations as

$$E_x = \int_{-\infty}^{\infty} |x(t)|^2 dt = \int_{-\infty}^{\infty} |\hat{x}(f)|^2 df.$$

(A.4)

Representing the signal in one dimensional,  $x(t)$  or  $\hat{x}(f)$ , does not provide enough information of the signal. For example, representing the signal by its instantaneous power does not provide information on how the frequency changes in time. Also, representing the signal by its spectral energy density only shows the global frequency contents of the signal. Because of that, a joint distribution of energy over time and frequency variable is introduced which can be expressed by  $\rho_x(t, f)$  given by

$$E_x = \int_{-\infty}^{\infty} \int_{-\infty}^{\infty} \rho_x(t, f) dt df.$$

(A.5)

The integration of time-frequency distribution along one variable, either time or frequency, we obtain the energy density that correspond to the other variable. These properties are known as marginal properties given in Eq. (A.6) and Eq. (A.7):

$$\int_{-\infty}^{\infty} \rho_x(t, f) dt = |\hat{x}(f)|^2$$

(A.6)

$$\int_{-\infty}^{\infty} \rho_x(t, f) df = |x(t)|^2$$

(A.7)

The advantage of STFT is the simplicity in implementation and interpretation from the result; however, the method has its limitation about the adequacy of its spectrogram. Spectrogram is the squared modulus of STFT of the signal,  $S_x^h(t, f) = |STFT_x^h(t, f)|^2$ , which represents the signal

energy distribution in the time-frequency plane. The energy of the signal is calculated by Eq. (A.8)

$$E_x = \int_{-\infty}^{\infty} \int_{-\infty}^{\infty} S_x^g(t, f) dt df \quad (\text{A.8})$$

where the analysis window is normalized to obtain unit energy  $\int_{-\infty}^{\infty} |g(t)|^2 dt = 1$ . The first limitation is the spectrogram's temporal and frequency resolutions. The size of the analysis window  $g(t)$  plays an important role on time-frequency resolution via the Heisenberg-Gabor uncertainty principle [54, 38]. A good time resolution require a short-time window  $g(t)$ ; whereas a good frequency resolution require large frequency bandwidth (or long-time window  $g(t)$ ). This makes the method not suitable for the high bandwidth signal. The uncertainty principle imposes a lower limit of the time-frequency building block as

$$\Delta t_g \Delta f_g \geq \frac{1}{4\pi}. \quad (\text{A.9})$$

The second limitation of STFT is the bias of the spectrogram which corresponds to smoothed version of the time-frequency representation which does not satisfy the marginal properties [54].

$$\int_{-\infty}^{\infty} S_x^g(t, f) dt = \int_{-\infty}^{\infty} |\hat{x}(f')|^2 |\hat{g}(f - f')|^2 df' \neq |\hat{x}(f)|^2 \quad (\text{A.10})$$

$$\int_{-\infty}^{\infty} S_x^g(t, f) df = \int_{-\infty}^{\infty} |x(t')|^2 |g(t' - t)|^2 dt' \neq |x(t)|^2 \quad (\text{A.11})$$

### A.3. Quadrature time-frequency analysis

The second class of time-frequency analysis is based on the distribution of signal energy over time and frequency where its marginal are unbiased. The general form of quadratic representation is

$$\text{TFR}_x(t, f) = \int_{-\infty}^{\infty} \int_{-\infty}^{\infty} \mathcal{K}(t, f; v, \tau) x\left(v + \frac{\tau}{2}\right) x^*\left(v - \frac{\tau}{2}\right) dv d\tau \quad (\text{A.12})$$

where  $\mathcal{K}(t, f; v, \tau) = K\left(v + \frac{\tau}{2}, v - \frac{\tau}{2}; t, f\right)$  is a kernel. Additional constraints obtained from imposing covariance are added to the kernel for the representation to meet the desired properties. For example, Cohen's class put constraints under time and frequency translation. The kernel of the covariance of the representation under time translation by  $t_0$  can be written as  $\mathcal{K}(t, f; v + t_0, \tau) = \mathcal{K}(t - t_0, f; v, \tau)$ . If we take  $v = 0$ s and  $t_0 = v$ , we can write

$$\text{TFR}_x(t, f) = \int_{-\infty}^{\infty} \int_{-\infty}^{\infty} k(t - v, f, \tau) x\left(v + \frac{\tau}{2}\right) x^*\left(v - \frac{\tau}{2}\right) dv d\tau \quad (\text{A.13})$$

where  $k(t - v, f, \tau) = \mathcal{K}(t, f; 0, \tau)$ . An additional constraint in frequency translation  $f_0$  is added to the kernel and it leads to  $k(t, f, \tau)e^{j2\pi f_0 \tau} = k(t, f - f_0, \tau)$ . By taking  $f = 0$ Hz and  $f_0 = -f$ , we obtain  $k(t, f, \tau) = k(t, 0, \tau)e^{j2\pi f_0 \tau}$ , we obtain a bilinear representation covariant under time and frequency translations as

$$\text{TFR}_x(t, f) = C_x(t, f) = \int_{-\infty}^{\infty} \int_{-\infty}^{\infty} \phi_{t-d}(t - v, \tau) x\left(v + \frac{\tau}{2}\right) x^*\left(v - \frac{\tau}{2}\right) e^{-j2\pi f \tau} dv d\tau \quad (\text{A.14})$$

with  $\phi_{t-d}(t, \tau) = k(t, 0, \tau) = \mathcal{K}(t, 0; 0, \tau)$ .

### A.3.1. Cohen's class

Cohen's class put constraints under time and frequency translation. The kernel of the covariance of the representation under time translation by  $t_0$  can be written as  $\mathcal{K}(t, f; v + t_0, \tau) = \mathcal{K}(t - t_0, f; v, \tau)$ . If we take  $v = 0$ s and  $t_0 = v$ , the representation can be written as

$$\text{TFR}_x(t, f) = \int_{-\infty}^{\infty} \int_{-\infty}^{\infty} k(t - v, f, \tau) x\left(v + \frac{\tau}{2}\right) x^*\left(v - \frac{\tau}{2}\right) dv d\tau \quad (\text{A.15})$$

where  $k(t - v, f, \tau) = \mathcal{K}(t, f; 0, \tau)$ . An additional constraint in frequency translation  $f_0$  is added to the kernel and it leads to  $k(t, f, \tau)e^{j2\pi f_0 \tau} = k(t, f - f_0, \tau)$ . By taking  $f = 0$ Hz and  $f_0 = -f$ , we obtain  $k(t, f, \tau) = k(t, 0, \tau)e^{j2\pi f_0 \tau}$ , we obtain a bilinear representation covariant under time and frequency translations as

$$\text{TFR}_x(t, f) = C_x(t, f) = \int_{-\infty}^{\infty} \int_{-\infty}^{\infty} \phi_{t-d}(t - v, \tau) x\left(v + \frac{\tau}{2}\right) x^*\left(v - \frac{\tau}{2}\right) e^{-j2\pi f \tau} dv d\tau \quad (\text{A.16})$$

with  $\phi_{t-d}(t, \tau) = k(t, 0, \tau) = \mathcal{K}(t, 0; 0, \tau)$ .

Wigner-Ville distribution is a member of Cohen's class. From Eq. (A.16), by moving from the delay variable  $\tau$  to a frequency convolution variable  $\nu$  using a Fourier transform, we obtain

$$C_x(t, f) = \int_{-\infty}^{\infty} \int_{-\infty}^{\infty} \phi_{t-f}(t - v, f - \nu) W_x(\nu, \nu) dv d\nu \quad (\text{A.17})$$

where  $W_x(\nu, \nu)$  is called the Wigner-Ville distribution (WVD)

$$W_x(\nu, \nu) = \int_{-\infty}^{\infty} x\left(v + \frac{\tau}{2}\right) x^*\left(v - \frac{\tau}{2}\right) e^{-j2\pi f \tau} d\tau \quad (\text{A.18})$$

and  $\phi_{t-f}(t, f)$  is a two-dimensional low-pass filter,

$$\phi_{t-f}(t, f) = \int_{-\infty}^{\infty} \phi_{t-d}(t, \tau) e^{-j2\pi f \tau} d\tau.$$

(A.19)

The time-frequency resolution of WVD is higher than that of the atomic decomposition; one of the main drawbacks is *interference terms* that are obtained when the signal has of more than one component. For example, the time-frequency representation of a signal  $y(t) = x_1(t) + x_2(t)$  can be described as

$$\text{TFR}_y(t, f) = \text{TFR}_{x_1}(t, f) + \text{TFR}_{x_2}(t, f) + \text{TFR}_{x_1 x_2}(t, f) + \text{TFR}_{x_2 x_1}(t, f)$$

(A.20)

where

$$\text{TFR}_{x_1 x_2}(t, f) = \int_{-\infty}^{\infty} \int_{-\infty}^{\infty} \phi_{t-d}(t - v, \tau) x_1\left(v + \frac{\tau}{2}\right) x_2^*\left(v - \frac{\tau}{2}\right) e^{-j2\pi f \tau} dv d\tau.$$

(A.21)

### A.3.2. Pseudo-Wigner-Ville distribution

The interference terms can be suppressed by a modified version of WVD, known as pseudo-Wigner-Ville distribution and smoothed-pseudo-Wigner-Ville distribution. In pseudo-Wigner-Ville distribution, a window  $h(\tau)$  is introduced in the original equation to decrease the number of the interference terms that are sufficiently separated in time. It also suppresses the amplitude of the interference terms by smoothing the signal in frequency direction. The pseudo-Wigner-Ville distribution can be described as

$$PW_x(v, v) = \int_{-\infty}^{\infty} h(\tau) x\left(v + \frac{\tau}{2}\right) x^*\left(v - \frac{\tau}{2}\right) e^{-j2\pi f \tau} d\tau.$$

(A.22)

Another extension on pseudo-Wigner-Ville distribution is smoothed pseudo-Wigner-Ville distribution where an additional window  $g(t)$  is used for signal smoothing in time independently from the frequency. The expression of the smoothed pseudo-Wigner-Ville distribution is given in Eq. (A.23).

$$SPW_x(v, \nu) = \int_{-\infty}^{\infty} g(t)h(\tau)x\left(v + \frac{\tau}{2}\right)x^*\left(v - \frac{\tau}{2}\right)e^{-j2\pi f\tau} d\tau$$

(A.23)

## APPENDIX B.

### Lagrange interpolation

Lagrange interpolation is a polynomial interpolation of degree less than  $n$  that passes through a discrete data set of  $n + 1$  samples. Let the interpolation vector  $P_n(z)$  of degree  $n$  that is constructed from a discrete data set  $(z_k, f_k)$ ,  $k = 0, \dots, n$ .  $z_k$  are the nodes and  $f_k = f(z_k)$  are the function values corresponding to the nodes. The Lagrange interpolation  $P_n(z)$  is described in Eq. (B.1), Eq. (B.2), and Eq. (B.3) [55].

$$P_n(z) = \sum_{k=0}^n l_k(z) f_k = \sum_{k=0}^n \frac{\omega_{n+1}(z)}{(z - z_k) \omega'_{n+1}(z_k)} f_k \quad (\text{B.1})$$

where

$$l_k(z) = \prod_{j=0, j \neq k}^n \frac{z - z_j}{z_k - z_j} \quad (\text{B.2})$$

and

$$l_k(z_j) = \delta_{k,j}. \quad (\text{B.3})$$

The nodal polynomial  $\omega_{n+1}$  can be described as shown in Eq. (B.4).

$$\omega_{n+1}(z) = \prod_{j=0}^n (z - z_k) \quad (\text{B.4})$$

## Bibliography

- [1] B. Saleh, "Localized Imaging," in *Introduction to Subsurface Imaging*, Cambridge, Cambridge University Press, 2011, p. 127.
- [2] E. Wolf, "Three-dimensional structure determination of semi-transparent objects from holographic data," *Optics Communications*, vol. 1, no. 4, pp. 153-156, 1969.
- [3] M. Kulkarni and J. Izatt, "Spectroscopic optical coherence tomography," in *CLEO '96*, 1996.
- [4] U. Morgner, W. Drexler, F. X. Kärtner, X. D. Li, C. Pitris, E. P. Ippen and J. G. Fujimoto, "Spectroscopic optical coherence tomography," *Optics letters*, vol. 25, no. 2, pp. 111-113, 2000.
- [5] R. Leitgeb, M. Wojtkowski, A. Kowalczyk, C. K. Hitzenberger, M. Sticker and A. F. Fercher, "Spectral measurement of absorption by spectroscopic frequency-domain optical coherence tomography," *Optics Letters*, vol. 25, no. 11, pp. 820-822, 2000.
- [6] G. J. Tearney, M. E. Brezinski, J. F. Southern, B. E. Bouma, M. R. Hee and J. G. Fujimoto, "Determination of the refractive index of highly scattering human tissue by optical coherence tomography," *Optics letters*, vol. 20, no. 21, pp. 2258-2260, 1995.
- [7] A. Fercher, C. Hitzenberger, G. Kamp and S. El-Zaiat, "Measurement of intraocular distances by backscattering spectral interferometry," *Optics Communications*, vol. 117, no. 1-2, pp. 43-48, 1995.
- [8] C. Xu, D. L. Marks, M. N. Do and S. A. Boppart, "Separation of absorption and scattering profiles in spectroscopic optical coherence tomography using a least-squares algorithm," *Optics express*, vol. 12, no. 20, pp. 4790-4803, 2004.
- [9] F. E. Robles and A. Wax, "Separating the scattering and absorption coefficients using the real and imaginary parts of the refractive index with low-coherence interferometry," *Optics Letters*, vol. 35, no. 17, pp. 28843-2845, 2010.
- [10] Y. Mao, S. Sherif, C. Flueraru and S. Chang, "3×3 Mach–Zehnder interferometer with unbalanced differential detection for full-range swept-source optical coherence tomography,"

*Applied Optics*, vol. 47, no. 12, pp. 2004-2010, 2008.

- [11] C. Flueraru, H. Kumazaki, S. Sherif, S. Chang and Y. Mao, "Quadrature Mach-Zehnder interferometer with application in optical coherence tomography," *Journal of Optics A: Pure and Applied Optics*, vol. 9, no. 4, 2007.
- [12] B. Saleh, "Overview," in *Introduction to Subsurface Imaging*, Cambridge, Cambridge University Press, 2011, p. 2.
- [13] W. Drexler, Ed., *Optical Coherence Tomography: Technology and Applications*, New York: Springer, 2008.
- [14] D. Huang, E. A. Swanson, C. P. Lin, J. S. Schuman, W. G. Stinson and W. Chang, "Optical coherence tomography," *Science*, vol. 254.5035, pp. 1178-1181, 1991.
- [15] J. G. Fujimoto, C. Pitris, S. A. Boppart and M. E. Brezinski, "Optical Coherence Tomography: An Emerging Technology for Biomedical Imaging and Optical Biopsy," *Neoplasia*, vol. 2, no. 1-2, pp. 9-25, 2000.
- [16] J. Welzel, E. Lankenau, G. Hüttmann and R. Birngruber, "OCT in Dermatology," in *Optical Coherence Tomography: Technology and Applications*, New York, Springer, 2008, pp. 1103-1121.
- [17] A. Terenteva, A. Shakhov, A. Maslennikova, N. Gladkova, V. Kamensky, F. Feldchtein and N. Shakhova, "OCT in Laryngology," in *Optical Coherence Tomography: Technology and Applications*, New York, Springer, 2008, pp. 1123-1148.
- [18] P. Wilder-Smith, L. Otis, J. Zhang and Z. Chen, "Dental OCT".
- [19] J. P. Dunkers, "Applications of Optical Coherence Tomography to the Study of Polymer Matrix Composites," in *Optical Coherence Tomography: Technology and Applications*, New York, Springer, 2008, pp. 1151-1176.
- [20] S. Chang, Y. Mao, G. Chang and C. Flueraru, "Jade detection and analysis based on optical coherence tomography images," *Optical Engineering*, vol. 49, no. 6, 2010.

- [21] Y. Cheng and K. V. Larin, "Artificial fingerprint recognition by using optical coherence tomography with autocorrelation analysis," *Applied Optics*, vol. 45, no. 36, pp. 9238-9245, 2006.
- [22] S. Chang, Y. Cheng, K. V. Larin, Y. Mao, S. Sherif and C. Flueraru, "Optical coherence tomography used for security and fingerprint-sensing applications," *Image Processing, IET*, vol. 2, no. 1, pp. 48-58, 2008.
- [23] P. Hariharan, *Basics of Interferometry*, Burlington, MA, USA : Academic Press , 2006.
- [24] M. Born and E. Wolf, *Principles of Optics*, seventh (expanded) ed., Cambridge: Cambridge University Press, 2003.
- [25] M. R. Hee, "Optical Coherence Tomography: Theory," in *Handbook of Optical Coherence Tomography*, B. E. Bouma and G. J. Tearney, Eds., New York, Marcel Dekker, Inc., 2002, pp. 41-49.
- [26] B. Saleh and E. Miller, "Tomographic Imaging," in *Subsurface Imaging*, Cambridge, Cambridge University Press, 2011, pp. 140-188.
- [27] M. A. Choma, M. V. Sarunic, C. Yang and J. A. Izatt, "Performance of fourier domain vs. time domain optical coherence tomography," *Optics Express*, vol. 11, no. 8, pp. 889-894, 2003.
- [28] A. C. Kak and M. Slaney, *Principles of Computerized Tomographic Imaging*, New York: IEEE Press, 1999.
- [29] J. Izatt and M. Choma, "Theory of Optical Coherence Tomography," in *Optical Coherence Tomography: Technology and Applications*, New York, Springer, pp. 47-72.
- [30] A. Rollins and J. Izatt, "Optimal interferometer designs for optical coherence tomography," *Optics Letters*, vol. 24, no. 21, pp. 1484-1486, 1999.
- [31] S. Jiao and M. Ruggeri, "Polarization effect on the depth resolution of optical coherence tomography," *Journal of Biomedical Optics*, vol. 13, no. 6, p. 060503, 2008.

- [32] G. Lamouche, M. Dufour, B. Gauthier, V. Bartulovic, M. Hewko and J.-P. Monchalín, "Optical delay line using rotating rhombic prisms," in *Proc. SPIE 6429, Coherence Domain Optical Methods and Optical Coherence Tomography in Biomedicine XI*, San Jose, CA, 2007.
- [33] "Thorlabs, Inc.," [Online]. Available: <http://www.thorlabs.com/>. [Accessed 15 April 2014].
- [34] "Newport," Newport Corporation, [Online]. Available: <http://www.newport.com/>. [Accessed 17 April 2014].
- [35] "OZ optics," 28 January 2014. [Online]. Available: [http://www.ozoptics.com/ALLNEW\\_PDF/DTS0079.pdf](http://www.ozoptics.com/ALLNEW_PDF/DTS0079.pdf). [Accessed 15 April 2014].
- [36] "Corning Incorporated," March 2010. [Online]. Available: <file:///C:/Users/thanusup/Downloads/SMF28eplusSpecialtyFiber.pdf>. [Accessed 4 April 2014].
- [37] P. Thanusutiyabhorn and F. Saccon, "Time-domain OCT system manual - Integrated Computational Imaging Lab internal report," Winnipeg, 2013.
- [38] D. Faber, M. Aalders, B. Hermann and W. Drexler, "Using Low Coherent Light for Spectroscopic Information from Tissue," in *Optical Coherence Tomography: Technology and Applications*, W. Drexler and J. G. Fujimotor, Eds., New York, Springer, 2008, pp. 697-712.
- [39] D. J. Faber, E. G. Mik, M. C. G. Aalders and T. G. v. Leeuwen, "Toward assessment of blood oxygen saturation by spectroscopic optical coherence tomography," *Optics Letters*, vol. 30, no. 9, pp. 1015-1017, 2005.
- [40] V. Jaedicke, S. Agcaer, F. E. Robles, M. Steinert, D. Jones, S. Goebel, N. C. Gerhardt, H. Welp and M. R. Hofmann, "Comparison of different metrics for analysis and visualization in spectroscopic optical coherence tomography," *Biomedical Optics Express*, vol. 4, no. 12, pp. 2945-2961, 2013.
- [41] F. Robles, R. N. Graf and A. Wax, "Dual window method for processing spectroscopic optical coherence tomography signals with simultaneously high spectral and temporal

- resolution," *Optics Express*, vol. 17, no. 8, pp. 6799-6812, 2009.
- [42] R. N. Bracewell, *The Fourier Transform and its Applications*, Singapore: The McGraw-Hill Companies, 2000.
- [43] J. Arthur R. Weeks, "Image Segmentation and Representation," in *Fundamentals of Electronic Image Processing*, Washington, SPIE-The International Society for Optical Engineering, p. 430.
- [44] E. Weisstein, "Wolfram MathWorld," Wolfram Research, Inc., 18 07 2014. [Online]. Available: <http://mathworld.wolfram.com/RiemannSum.html>. [Accessed 21 07 2014].
- [45] P. Drinkwater, "The Fourier Transform.com," 2010. [Online]. Available: <http://www.thefouriertransform.com/transform/integration.php>. [Accessed 13 06 2014].
- [46] J. Campos, L. P. Yaroslavsky, A. Moreno and M. J. Yzuel, "Integration in the Fourier domain for restoration of a function from its slope: comparison of four methods," *Optics letters*, vol. 27, no. 22, pp. 1986-1988, 2002.
- [47] F. P. Bolin, L. E. Preuss, R. C. Taylor and R. J. Ference, "Refractive index of some mammalian tissues using a fiber optic cladding method," *Applied Optics*, vol. 28, no. 12, pp. 2297-2303, 1989.
- [48] M. N. Polyanskiy, "Refractive index database," [Online]. Available: <http://refractiveindex.info/?shelf=main&book=H2O&page=Hale>. [Accessed 08 04 2014].
- [49] J. W. Cooley, P. A. W. Lewis and P. D. Welch, "The Fast Fourier Transform and Its Applications," *IEEE Transactions on Education*, vol. 12, no. 1, pp. 27-34, 1969.
- [50] R. P. Kanwal, *Linear Integral Equations: Theory & Technique*, Boston: Birkhäuser, 1997.
- [51] H. Fu and C. Liu, "A buffered Fourier spectral method for non-periodic PDE," *International Journal of Numerical Analysis and Modeling*, vol. 9, no. 2, pp. 460-478, 2012.
- [52] H. Jeffreys and B. S. Jeffreys, *Methods of Mathematical Physics*, 2nd edition ed., Cambridge: The Cambridge University Press, 1950.

- [53] M. S. Zhdanov, Geophysical Electromagnetic Theory and Methods, Amsterdam : Elsevier, 2009, p. 305.
- [54] F. Hlawatsch and F. Auger, Time-Frequency Analysis, Wiley, 2010.
- [55] NIST, "NIST Digital Library of Mathematical Functions," 25 04 2014. [Online]. Available: <http://dlmf.nist.gov/>. [Accessed 13 06 2014].